



Centre for Sensors, Instruments and  
Systems Development  
UNIVERSITAT POLITÈCNICA DE CATALUNYA  
Shaping light to your needs

# DOCTORAL THESIS

FOR OBTAINING THE DOCTORAL DEGREE  
IN THE FIELD OF OPTICAL ENGINEERING FROM THE  
**TECHNICAL UNIVERSITY OF CATALONIA**  
**UPC-BARCELONATECH**  
DEPARTMENT OF OPTICS AND OPTOMETRY  
FACULTY OF OPTICS AND OPTOMETRY

---

## DEVELOPMENT OF A NEW SPECTRAL IMAGING SYSTEM FOR THE DIAGNOSIS OF SKIN CANCER

---

*Author:*

**XANA DELPUEYO ESPAÑOL**

*Thesis Directors:*

**DR. MERITXELL VILASECA RICART**

**DR. SANTIAGO ROYO ROYO**

Terrassa, 2017





Academic year:

## Assessment results for the doctoral thesis

Full name

Doctoral programme

Structural unit in charge of the programme

## Decision of the committee

In a meeting with the examination committee convened for this purpose, the doctoral candidate presented the topic of his/her doctoral thesis entitled \_\_\_\_\_

Once the candidate had defended the thesis and answered the questions put to him/her, the examiners decided to award a mark of:

FAIL

PASS

GOOD

EXCELLENT

(Full name and signature)		(Full name and signature)	
Chairperson		Secretary	
(Full name and signature)	(Full name and signature)	(Full name and signature)	(Full name and signature)
Member	Member	Member	Member

The votes of the members of the examination committee were counted by the Standing Committee of the Doctoral School, and the result is to award the CUM LAUDE DISTINCTION:

YES

NO

(Full name and signature)	(Full name and signature)
---------------------------	---------------------------

Barcelona, \_\_\_\_\_

## International doctorate mention

- As the secretary of the examination committee, I hereby state that the thesis was partly (at least the summary and conclusions) written and presented in a one of the languages commonly used in scientific communication in the relevant field of knowledge, which must not be an official language of Spain. This rule does not apply to stays, reports and experts from a Spanish-speaking country.

(Full name and signature)
---------------------------



---

# Agraïments

---

Després de quatre anys de doctorat, la llista de persones que han participat de manera directa, més a nivell científic, com indirecta, amb suport emocional, és molt llarga. Però voldria mencionar-ne alguns.

En primer lloc vull dedicar els meus sincers agraïments als meus directors de tesi, sense els quals la consecució d'aquest treball no hauria estat possible, la Dra. Meritxell Vilaseca, el Dr. Santiago Royo i el Dr. Jaume Pujol, tot i que només hi va poder participar en els inicis.

A tots els/les companys/es del CD6: Cristina M., Cristina C., Miguel, Xavi, Rosa, Julia., Anna, Ciscu, Ajit, Reza, Noe, Carlos E...; en especial els que hem conviscut més temps en la Sala 31: Carlos, Paula, Laura, Sara, Eli... els quals la seva companyia ha estat imprescindible durant aquest temps; Jorge, el veterà en color que em va ensenyar gran part del que se ara, ajudant-me sempre que ho he necessitat, inclús després de tornar a Colòmbia; i a Chenxue i Bernat per tota la seva ajuda en l'anàlisi de dades.

Al consorci de Diagnostocs, que sempre m'han tractat tant hospitalàriament en totes les reunions, i que tant m'han ajudat quan ho he necessitat, en especial a la Bea per tota la paciència en aquests anys tot i els maldecaps que han donat els sistemes.

Al Research Group of Optoelectronics for Embedded Systems, LAAS-CNRS liderat per Thierry Bosch, per la seva acollida durant la meva estància: Thierry, Adam i Julien; a la colla d'estudiants Antonio, Bastien, Fernando, Mengkoung, Mohanad, i en especial a Laura i Alejandro.

A la gent del MeetUp "Españoles en Toulouse", que sense ells no hauria gaudit tant de la meva estança a Toulouse, en especial a Eliseo i Irene per sentir-me dins del grup des del primer moment, i a Izarra per la paciència escoltant les meves batalletes amb la tesi.

A la gent del MeetUp "Jocs de Taula" de Terrassa, que m'han permès desconnectar del doctorat aquestes últimes setmanes.

Els meus/meves amics/amigues Uri, Vero, David, Mariona, Jose, Joan, Helena, Marc, Guillem... pel seu recolzament moral dia a dia.

A la meua parella, Dani, per tenir tanta paciència, comprensió i estar sempre el meu costat sense importar el moment o la distància, i encara més tenint en compte tot el que implica haver-nos conegut en l'últim any de doctorat

Al meus pares, Jordi i Yolanda, per recolzar-me sempre en totes les decisions preses i ajudar-me sempre que ho he necessitat.

---

Finalment, voldria mostrar el meu agraïment al CD6 per la seva acollida i l'ajuda rebuda per a realitzar aquesta tesi i al COST per la beca que em va permetre realitzar l'estança a Toulouse.

A tots, moltes gràcies.

---

## Supervisors' Certificate

Meritxell Vilaseca Ricart and Santiago Royo Royo, professors at the Universitat Politècnica de Catalunya (UPC),

### **CERTIFY**

that the work reported in the thesis entitled

### **Development of a New Spectral Imaging System for the Diagnosis of Skin Cancer**

which is submitted by Xana Delpueyo Español in fulfilment of the requirements for the degree of Doctor with the international Doctorate mention by the Universitat Politècnica de Catalunya (UPC) has been carried out under our supervision within the framework of the PhD program in Optical Engineering of the same university.

---

Meritxell Vilaseca Ricart

---

Santiago Royo Royo

---



---

# Contents

---

Contents .....	V
List of figures.....	IX
List of tables.....	XVII
<b>1. Introduction and Goals.....</b>	<b>1</b>
<b>2. State of the art .....</b>	<b>5</b>
2.1. Spectral imaging systems.....	5
2.2. Spectral sampling techniques.....	9
2.2.1. Passive variant .....	9
2.2.2. Active variant.....	11
2.3. Image sensors.....	11
2.3.1. Noise sources .....	12
2.4. Obtaining spectral and colour information from spectral imaging systems .....	13
2.5. Metrics used for the evaluation of spectral and colour differences.....	15
2.5.1. Spectral differences.....	15
2.5.2. Colour differences.....	16
2.6. Textural analysis .....	17
2.7. Applications of spectral imaging systems .....	18
2.7.1. Spectral imaging systems for the skin cancer detection.....	20
<b>3. Experimental system .....</b>	<b>27</b>
3.1. Multiphotonic platform.....	27
3.1.1. Confocal microscopy.....	28
3.1.2. 3D technology.....	29
3.1.3. Laser self-mixing technology (Optical Feedback Interferometry, OFI) .....	31

3.1.4.	Barcelona and Modena platforms: operation, computers and metal rings for the spatial correlation.....	32
3.2.	Multispectral system.....	35
3.2.1.	Design and components.....	35
3.2.2.	Acquisition software.....	41
3.2.2.1.	Extended software.....	41
3.2.2.2.	User interface.....	45
3.2.3.	Validation of the system's performance.....	47
3.2.3.1.	Temporal behaviour of the LEDs emission.....	47
3.2.3.2.	Linearity, uniformity and repeatability of the system.....	48
3.2.4.	Safety issues.....	51
<b>4.</b>	<b>Image processing and analysis.....</b>	<b>57</b>
4.1.	From spectral to reflectance and colour images.....	57
4.2.	Parameters analysed: spectral, colour and textural information.....	65
<b>5.</b>	<b>Results.....</b>	<b>69</b>
5.1.	Inclusion criteria and measurement protocol.....	69
5.2.	Clinical measurements and samples.....	71
5.3.	Classification algorithm and outcomes.....	78
5.4.	Discussion.....	86
<b>6.</b>	<b>Combination of the systems.....</b>	<b>91</b>
6.1.	3D system results.....	91
6.2.	Combined results.....	94
<b>7.</b>	<b>Conclusions.....</b>	<b>97</b>
<b>8.</b>	<b>Future work.....</b>	<b>101</b>
<b>9.</b>	<b>Dissemination.....</b>	<b>103</b>
9.1.	Journal publications.....	103
9.2.	Congress proceedings.....	103
9.3.	Patent.....	104

**10. Bibliography .....105**

**Appendix A. Datasheets of components used in the developed system .....116**

    A.1 Big metal ring..... 116

    A.2 DMK 23U455 camera ..... 116

    A.3 Sony ICX445ALA sensor ..... 118

    A.4 Schenider-Kreuznack Cinegon 1.8/16 ..... 120

    A.5 LEDs board ..... 122

    A.6 Electronic board to control the LEDs..... 123

    A.7 Visible linear polarizing laminated film from Edmund Optics..... 124

    A.8 X Rite ColorChecker® Classic CCCR ..... 125

**Appendix B. Intrumentation used in the thesis.....126**

    B.1 Spectrometer Instrument Systems Spectro 320..... 126

        B.1.1 Optical probe EOP 146..... 127

        B.1.2 Telescopic optical probe TOP 100 ..... 128

        B.1.3 Telescopic optical probe TOP 100 ..... 129

    B.2 International Light Radiometer (IL 1700) ..... 130

**Appendix C. User manual of the multispectral system.....132**



---

# List of figures

---

Figure 1.1 Commercial dermoscope [3] (top left), nevi observed through naked-eyed (top centre), nevi observed through dermoscopy (top right), melanoma observed through naked-eyed (bottom left), and melanoma observed through dermoscopy (bottom right) [4].	2
Figure 2.1 Spectral cube of the Earth’s surface. The spectral signatures or fingerprints from several areas are shown on the right [19].	6
Figure 2.2 Methods for acquiring the spectral datacube: point scanning (left), line scanning (centre), and area scanning (right) systems. The spectral datacube contains two spatial (x, y) and one spectral ( $\lambda$ ) dimension. Blue areas represent data acquired simultaneously. Red arrows represent temporal scanning required to complete the datacube [18].	7
Figure 2.3 Whiskbroom system layout [20].	7
Figure 2.4 Pushbroom system layout [20].	8
Figure 2.5 Staring imager system layout [20].	8
Figure 2.6 Commercially available liquid crystal tuneable filter [25] (left), acousto-optic tuneable filter [26] (centre), and filter wheel [27] (right).	10
Figure 2.7 : Liquid crystal tuneable filter: spectral transmittances [28] (left) and main components [29] (right).	10
Figure 2.8 Main components of an acousto-optic tuneable filter (RF: radio frequency) [32].	10
Figure 2.9 Scheme of transference process for CCD and CMOS sensors. Adapted from: [40].	12
Figure 2.10 Interpolation used to mask a hot-pixel.	13
Figure 2.11 space: 3D representation [58] (left), and spatial projection for a constant lightness value [59] (right).	15
Figure 2.12 ITA examples for different skin types with the corresponding histologies (left), and scale used for classification (right) [67].	16

Figure 2.13 Examples of spectral information obtained from different spectral imaging systems: images over Cuprite (Nevada, USA) obtained from the AVIRIS imaging spectrometer with a spectral range from 400 nm to 2500 nm and used to measure and monitor the components of the Earth’s surface [74] (left). The monochrome image corresponds to a specific spectral image and the pseudo-coloured image to the mineral distribution of alunite or kaolinite obtained from several bands. Spectral monochromatic images corresponding to 640 nm and 1000 nm, respectively, of a Byzantine painting (right). In the 1000 nm image some corrections of the hand’s virgin can be observed [23].  
 .....18

Figure 2.14 Spectral images of a mandarin acquired at 550, 660 and 1000 nm with a VIS and a NIR LCTF [79] (left), images and intensity profiles of two apples at 680 nm where the irregularities in the plot of the right apple indicates a fungal contamination [85] (right).....19

Figure 2.15 Simulation of a crime scene, in which fresh and older blood stains were automatically detected based on their reflectance and coloured in the image in blue and red, respectively [18]......19

Figure 2.16 Images of the retina at several wavelengths from a spectral imaging system based on LEDs [90].....20

Figure 2.17 2-layer skin model from Ohtsuki and Healy [99] .....21

Figure 2.18 Absorption of oxy- and deoxyhaemoglobin, melanin and water [102]. .....21

Figure 2.19 Mean spectral optical density of 17 melanomas, 65 common nevi and 82 healthy skin samples [103]. .....22

Figure 2.20 Distribution maps measured with the SIAscope V<sup>TM</sup> [104]) (top), system and MoleMate<sup>TM</sup> program [112] (bottom left), and scoring algorithm based on a diagnostic tree [98] (bottom right). .....23

Figure 2.21 Melafind® system [113] (left) and software screenshot [108] (right). .....24

Figure 2.22 Spectral images at 450, 545, 660 and 940 nm (top), and maps of a melanoma (E: erythema, B: bilirubin) (bottom) [110]......24

Figure 2.23 Scatter plot with the averaged parameter  $p$  for nevi and melanomas subtracted by the same parameter of the surrounding healthy skin of the patient ( $p0$ ) [103]......25

Figure 2.24 Spectral images and distribution maps of a malignant lesion (basal cell carcinoma) [111]. .....26

Figure 3.1 Medical cart with the confocal microscope, the OFI, the 3D and the multispectral systems. ....28

Figure 3.2 Confocal microscopic system (MAVIG VivaScope®) included in the multiphotonic platform: layout (left), picture of the head and image provided (right) [121]. .....29

Figure 3.3 Projected fringes, colour image and epipolar triangulation used (top), lesion and 3D prototype (middle) and topographic images of the skin and the lesion (bottom) obtained with the 3D system. ....30

Figure 3.4 OFI system. ....31

Figure 3.5 Scheme of the laser beam, where the red dot lines indicate the laser path when X and Y are at 0° and the black dot lines indicate the path in the extremes of the angular range of the mirror [127] (left). 2D OFI signal image proportional to the blood perfusion level (right). ....32

Figure 3.6 Multiphotonic platforms installed in Barcelona and Modena, respectively. ....33

Figure 3.7 Connection scheme and computers to operate with the different devices included in the platform. ....34

Figure 3.8 Big metal ring for the acquisition of the 3D, OFI and multispectral system (top left), small metal ring for the confocal microscopy acquisition (top right), and the big metal ring being used at the clinical setting (bottom). ....34

Figure 3.9 Several views of the multispectral system with the base. ....35

Figure 3.10 Overview of the multispectral head including the cylinder and the conus. ....36

Figure 3.11 Normalised spectral emission of the purchased VIS and NIR LEDs. ....37

Figure 3.12 PCB with the LED ring and view of the LED ring mounted inside the cylinder (top) and view of the inside of the front conus (bottom). ....38

Figure 3.13 Distribution of the multispectral head components (top): (1) camera, (2) objective lens, (3) LED ring, (4) polarizers; Polarizer attached to the conus (bottom left) and top view of the multispectral head with the lever allowing the degree of polarization to be changed (bottom right). ....39

LIST OF FIGURES

---

Figure 3.14 Spectral images taken at different wavelengths (414 nm, 524 nm, 735 nm and 995 nm) with the polarizers parallel (left) and crossed (right). The removal of the specular reflection can be clearly seen, mainly at shorter wavelengths. The longer wavelengths do not show this effect so clearly as they penetrate deeper into the tissue..40

Figure 3.15 standard calibrated sample in the “IN” and “OUT” positions (left); and design of the interior of the base where the power supply, electronic boards, standard calibrated sample and other parts of the system are located (right).....40

Figure 3.16 Reflectance of the “Neutral 6.5” from the X Rite ColorChecker® Classic CCCR chart measured with the spectrometer SPECTRO 320 attached to the integrating sphere ISP80 from Instrument Systems, GmbH (Appx. B.1 and B.1.2, respectively) [131]. .....41

Figure 3.17 Screenshot of the extended software. The turquoise box used for testing is shown on the left while the grey box available for physicians is on the right side. ....45

Figure 3.18 Pop-up message that appeared if the calibration was not already done.....46

Figure 3.19 “PATIENT SELECTION” screen (top), confirmation screen (centre) and pop-up warning message (bottom). .....46

Figure 3.20 Radiance ( $W/sr.m^2$ ) of the 414 nm LEDs at different forward currents measured every second over 10 seconds.....47

Figure 3.21 Digital levels vs. exposure time at different wavelengths to test for the linearity of the camera response. ....48

Figure 3.22 Spectral images of the uniform sample “Neutral 6.5” from the X Rite ColorChecker® Classic CCCR chart and their corresponding SNUP values.....49

Figure 3.23 Mean digital levels of the 9 spectral images obtained along 9 different days for each wavelength.....50

Figure 3.24 Mean digital levels of the 9 spectral images acquired consecutively for each wavelength.....50

Figure 4.1 Graphical User Interface (GUI) to compute spectral and colorimetric images. ....57

Figure 4.2 Reflectance images at different wavelengths (414 nm, 447 nm, 731 nm, 477 nm, 890 nm, 524 nm, 995 nm and 671 nm) and degrees of polarization ( $0^\circ$ ,  $45^\circ$ ,  $90^\circ$ ) for a common nevus.....58



Figure 4.3 Pseudo-coloured image (left) and averaged reflectance curves from the ROIs selected (right). In the reflectance plot the solid line corresponds to the crossed polarizers ( $90^\circ$ ), the empty circles to  $45^\circ$  and the filled circles to  $0^\circ$  (parallel polarizers). .....59

Figure 4.4 Images in terms of pseudo-CIELAB colour coordinates:  $L^*$ ,  $a^*$ ,  $b^*$ ,  $C^*_{ab}$  and  $h_{ab}$  for a common nevus. ....60

Figure 4.5 Reflectance (top) and absorbance curves (bottom) obtained for two skins from different people with the multispectral system with crossed polarizers and the spectrometer SPECTRO 320. ....61

Figure 4.6 Reflectance images at 414 nm, 477 nm and 671 nm for two different lesions; the lesion on the top is a clear example of a highly pigmented lesion. Higher melanin absorbance at shorter wavelengths make the lesion to appear smaller at 671 nm; in this case, the image at 414 nm was used for the segmentation. In the one in the bottom, the contrast of the lesion and the surrounding skin at 414 nm is not enough as it is not as pigmented as the first one, so the next spectral image at 477 nm was used for the segmentation. ....62

Figure 4.7 Top: From left to right, a non-homogenous lesion segmented with only one threshold and the same lesion segmented with 4 different thresholds, respectively. Bottom: steps of the segmentation algorithm. The upper images correspond to the implementation of the Otsu method for each subimage. The images at the bottom are (from left to right): transposition, removal of pixel groups of the lesion with less than 15.000 pixels, fill in the black areas to obtain the final mask, and finally, the segmented lesion. ....63

Figure 4.8 Flow chart of the segmentation process. ....64

Figure 4.9 Images in terms of pseudo-CIELAB colour differences ( $E$ ), goodness-of-fit coefficient (GFC) and Individual Typology Angle (ITA) between the lesion and the averaged surrounding skin for a common nevus (refer to figure 4.4. for the images in terms of pseudo-CIELAB colour coordinates of the same lesion). ....64

Figure 4.10 Physical parameters calculated after the segmentation of the lesion. ....64

Figure 4.11 Graphical User Interface (GUI) using Matlab® software to operate with reflectance images. ....65

Figure 5.1 Patient lying in the bed while the practitioner prepares the big metal ring in order to measure a lesion with the multiphotonic platform .....70

## LIST OF FIGURES

---

Figure 5.2 Summary of the lesions included in the study and measured with the multispectral imaging system. The lesions in green and red correspond to benign and malignant lesions, respectively. ....	72
Figure 5.3 Reflectance images (top), conventional colour photography (bottom left), dermoscopic image (bottom centre), and segmented image of a non-pigmented basal cell carcinoma. ....	72
Figure 5.4 Reflectance images (top), conventional colour photography (bottom left), dermoscopic image (bottom centre), and segmented image of a pigmented lesion with irregular and blurred borders. The lesion has two differentiated areas in terms of colour (light and brown). ....	73
Figure 5.5 Reflectance images (top), conventional colour photography (bottom left), dermoscopic image (bottom centre), and segmented image of a pigmented lesion bigger than the field of view of the multispectral system.....	73
Figure 5.6 Reflectance images (top), conventional colour photography (bottom left), dermoscopic image (bottom centre), and segmented image of a lesion with misalignments of the lesion along wavelengths due to the breath movement of the patient. ....	74
Figure 5.7 Reflectance images (top), conventional colour photography (bottom left), dermoscopic image (bottom centre), and segmented image of a lesion with hairy zones. ....	74
Figure 5.8 Reflectance images (top), conventional colour photography (bottom left), dermoscopic image (bottom centre), and segmented image of a lesion with many different colours. ....	75
Figure 5.9 Reflectance images (top), conventional colour photography (bottom left), dermoscopic image (bottom centre), and segmented image of a nevus. ....	75
Figure 5.10 Reflectance images (top), conventional colour photography (bottom left), dermoscopic image (bottom centre), and segmented image of a melanoma. ....	76
Figure 5.11 Reflectance images (top), conventional colour photography (bottom left), dermoscopic image (bottom centre), and segmented image of a pigmented basal cell carcinoma. ....	76
Figure 5.12 Reflectance images (top), conventional colour photography (bottom left), dermoscopic image (bottom centre), and segmented image of a non-pigmented basal cell carcinoma. ....	77

Figure 5.13 Reflectance images (top), conventional colour photography (bottom left),  
dermoscopic image (bottom centre), and segmented image of a seborrheic keratosis..... 77

Figure 5.14 Averaged reflectance ( $\pm\sigma$ , standard deviation) of nevi, melanomas and basal  
cell carcinomas. .... 78

Figure 5.15 Histograms of a nevus, a melanoma and a pigmented basal cell carcinoma in  
terms of spectral reflectance at 414 nm (top), and at 671 nm (bottom) with their  
respective values of mean ( $\bar{x}$ ), standard deviation ( $\sigma$ ), maximum, minimum, entropy  
( $E_p$ ), energy ( $E_n$ ), and third central moment ( $\mu_3$ ). .... 79

Figure 5.16 Flow chart of the classification algorithm. .... 81

Figure 5.17 Scatter plots of the 15 selected parameters. .... 83

Figure 6.1 Horizontal width and perimeter of a lesion (top), and the 4 methods used to  
calculate the area and volume of any lesion (bottom)..... 92

Figure 6.2 3D topography of a nevus (left) and a melanoma (right)..... 92

Figure 6.3 Scatterplots of the 3 selected parameters for the 3D system..... 93



---

# List of tables

---

Table 3.1 Peak wavelength ( $\lambda_p$ ), spatial emission (angle in degrees), and dimension of the LEDs given by the manufacturer, and the reason of selection of the wavelength. ....	37
Table 3.2 Measured peak wavelength ( $\lambda_p$ ) and FWHM of the purchased VIS and NIR LEDs. ....	38
Table 3.3 Exposure times (in milliseconds) needed to obtain the averaged digital levels (DL) from 900 to 3600 ( $\pm 200$ ) in steps of 300 for the 3 degrees of polarization and the uniform calibrated sample “Neutral 6.5”. ....	44
Table 3.4 Forward current used for each wavelength (expressed in mA). ....	48
Table 3.5 Percentage of variation in terms of digital levels of the 9 images acquired in 9 different days for each wavelength. ....	50
Table 3.6 Percentage of variation in terms of digital levels of the 9 images acquired consecutively for each wavelength. ....	51
Table 3.7 Equations, irradiance limits and irradiance measured according to UNE-EN 62471. ....	52
Table 3.8 Equations, radiance limits and radiance measured according to UNE-EN 62471. ....	54
Table 5.1 Thresholds for the 15 selected parameters. ....	84
Table 5.2 Mean, standard deviation ( $\sigma$ ), maximum and minimum for the nevi included in the validation set, for the 15 selected parameters. ....	84
Table 5.3 Mean, standard deviation ( $\sigma$ ), maximum and minimum for the melanomas included in the validation set, for the 15 selected parameters. ....	85
Table 5.4 Mean, standard deviation ( $\sigma$ ), maximum and minimum for the melanomas included in the validation set, for the 15 selected parameters. ....	85
Table 5.5 Confusion matrix of the validation set when including melanomas, basall cell carcinomas and nevi in the analysis. ....	86
Table 5.6 Confusion matrix of the validation set when including melanomas and nevi in the analysis. ....	86

LIST OF TABLES

---

Table 6.1 Confusion matrix of the 3D system.....93

Table 6.2 Sensitivity and specificity of each system individually (Multispectral and 3D)  
and when they are combined.....94

---

# 1. Introduction and Goals

---

The incidence of skin cancer in Europe, US, and Australia is rising rapidly. One in five people will develop some form of skin cancer in the course of a lifetime. Skin cancer accounts for one in three cancers worldwide. A person has a 1:25 chance to develop melanoma, the most aggressive skin cancer which causes the greatest number of deaths [1]. In fact, it is the second most common cancer in young adults (aged 15-34 years) and twice as common in women in this age group. About 90% of skin cancers are caused by exposure under ultraviolet (UV) light in sunlight. Moreover, the use of sunbeds doubles the risk of developing melanoma. The World Health Organization estimates that 60,000 people die every year from too much sun: 48,000 from melanoma and 12,000 from other skin cancers.

The 5-year survival rate for people with skin cancers significantly improves if detected and treated early. Accordingly, significant improvement of the current diagnostic tools of dermatologists is required in order to identify dermal disorders at a very early stage as well as to monitor directly the effects of treatment.

Visual inspection followed by histological examination is, still today, the gold standard for clinicians. This visual inspection is carried out by dermoscopy. A dermoscope is a handheld device with a magnifying lens and a white and uniform illumination field. The light is often polarized to remove specular reflection from the skin surface to obtain information from deeper layers. Dermoscopy allows the specialists to identify different structures, patterns and colours of the skin lesions suggesting if they are benign (seborrheic keratosis, haemangiomas, lipomas, warts) or malignant (melanoma, basal cell carcinoma) (Figure 1.1).

The dermoscopic technique requires considerable training in the interpretation of what is seen and is highly dependent on subjective impressions [2]. One of the most used rules to inspect skin lesions is the ABCD, which outlines warning signs of the most common type of melanoma: A is for asymmetry (one half of the lesion does not match the other half), B is for border irregularity (the edges are ragged, notched, or blurred), C is for colour (the pigmentation is not uniform, with variable degrees of tan, brown, or black) and D is for a diameter greater than 6 millimetres. However, while most melanomas tend to exhibit these features, amelanotic melanomas usually do not, and hence their diagnosis is often delayed. In addition, melanomas arising *de novo* (not within pre-existing nevi) will be smaller than 6 mm at an early stage. The acronym is also not very specific, as seborrheic keratosis which are very common in older patients often will exhibit “ABCD” features.

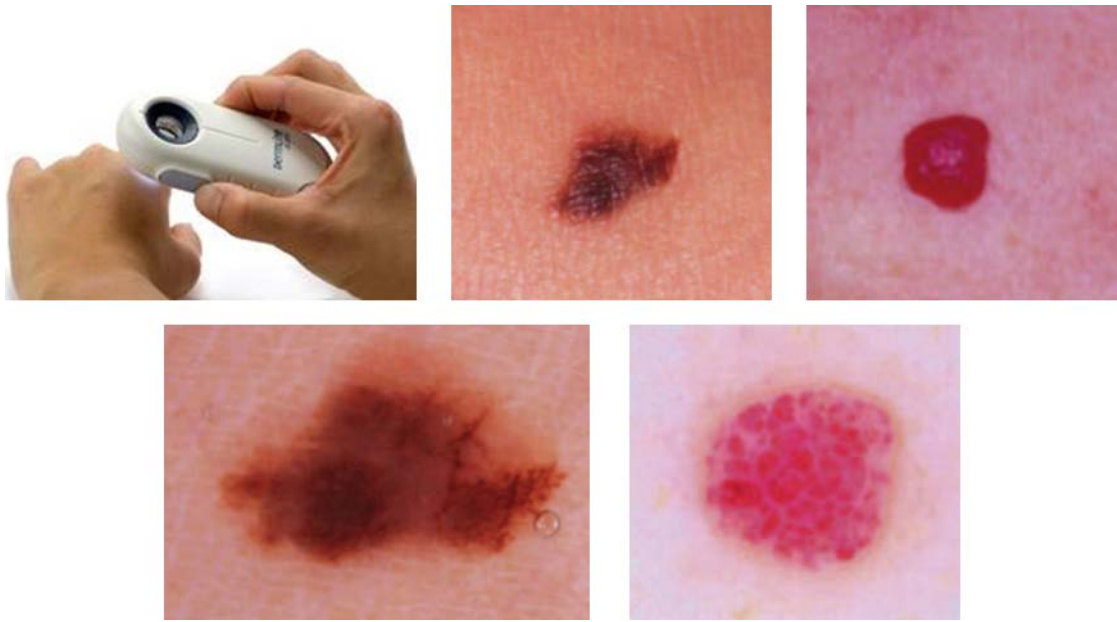


Figure 1.1 Commercial dermoscope [3] (top left), nevi observed through naked-eyed (top centre), nevi observed through dermoscopy (top right), melanoma observed through naked-eyed (bottom left), and melanoma observed through dermoscopy (bottom right) [4].

On the other hand, short-term monitoring studies have revealed that most growing melanomas exhibit observable changes over a period of 3-6 months and longer-term observational studies similarly found that melanomas tend to exhibit non-uniform growth patterns. Given these considerations, the addition of ‘E’ of evolution to the ABCD acronym is recommended, to increase its sensitivity and specificity [5], [6].

Even so, a large number of unnecessary surgical procedures are still performed. Around 10,000 biopsies are investigated annually in a typical sized hospital. The direct annual costs of diagnosis and treatment of skin cancer are several billion dollars in United States. Therefore, a significant improvement of the current diagnostic tools of dermatologists is demanded in order to identify dermal disorders at a very early stage as well as to monitor directly the effects of treatment [4], [7].

As a means of overcoming the limitations of dermoscopy, confocal microscopy has started to be used. Even this technique provides in-vivo characterisation of skin data at cellular-level resolution and can notably improve diagnosis of skin cancer, there is still a long way to go.

For this reason, the European Project DIAGNOPTICS “Diagnosis of skin cancer using optics” (ICT PSP seventh call for proposals 2013) aimed to launch a hospital service based on a multiphotonic platform to improve skin cancer diagnosis with the combination of four non-invasive novel techniques: 3D imaging which based on fringe projection to obtain information of the lesions’ topography, a multispectral system which provided precise colorimetric and spectral information of the skin lesions, optical feedback interferometry



(OFI) to analyse their blood flow by means of a laser imaging technique, and the confocal microscopy, offering improved diagnostic accuracy for skin tumours. These technologies and their associated procedures were envisaged to improve the detection ratio and the evaluation of the prognosis of skin cancer at earlier stages, compared with the conventional approach based on simple naked-eye inspection of lesions or digital dermoscopy.

The abovementioned technologies were demonstrated in a pilot project, in accordance with standard clinical workflows, protocols and procedures, involving professional healthcare end-users and covering a sufficient range of skin cancer profiles in two healthcare specific institutions: Hospital Clinic i Provincial de Barcelona (and its associated research centre, IDIBAPS) (Spain) and the Università degli Studi di Modena e Reggio Emilia (Italy) clinical facilities. Both clinical teams are world-class experts in in-vivo and ex-vivo skin cancer diagnosis and prognosis. The consortium involved the rest of actors required. The Centre for Sensors, Instruments and Systems Development from Universitat Politècnica de Catalunya (CD6-UPC), (Spain) is an experienced centre in photonics engineering, and the Institut National Polytechnique de Toulouse (INPT) (France) is expert in blood flow analysis using laser imaging. Finally, two Small and Medium-Sized Enterprises (SME) pursue the commercialization of the results of the project. Carril is a medical device company interested in the exploitation of the in-vivo imaging platform, while MAVIG is a manufacturer of confocal microscopes with products already in the market for the analysis of skin cancer lesions.

In this context, this thesis is focused on a multispectral system developed in the DIAGNOPTICS project, which allowed precise colour and spectral information of the lesions to be obtained. Multispectral systems capture image data through several specific wavelengths or spectral bands along the electromagnetic spectrum. Therefore, colour and spectral information from the lesion is available pixel by pixel. Chromophores such as melanin, haemoglobin, water etc. as well as other structures might differ among lesions of different etiologies, so, diagnosis of skin cancer can be improved through the use of spectroscopic and colour data given by multispectral technology.

In order to reach the goal of this thesis, i. e., the development of a multispectral system for the analysis of skin lesions, the following stages have been completed:

1. Review of multispectral system devices, focusing on those used for skin cancer.
2. Design, implementation and calibration of the multispectral system.
3. Generation of the software acquisition for physicians.
4. Implementation of the system in the hospitals to measure real skin lesions.
5. Analysis of the images obtained and classification for diagnosis.

This thesis is structured in eight chapters including this one. Chapter 2 provides a description of the different topics covered by this work. The concept of spectral imaging systems, image sensors and the analysis of spectral, colorimetric and textural features is

also included. The last part comprises a summary about the applications of spectral imaging systems, focusing on cancer detection.

Chapter 3 describes the experimental system developed. First, the four techniques used in the multiphotonic platform built in the DIAGNOPTICS project are briefly explained, i. e., confocal microscopy, 3D and Optical Feedback Interferometry (OFI) systems; the second section is entirely focused on the multispectral imaging system developed in this thesis.

Chapter 4 is centred in the image processing and analysis of the spectral images obtained from real skin lesions in order to extract valuable information. That is, computing reflectance and colour images from the images taken, the segmentation algorithm used, and the spectral, colour and textural parameters analysed from the lesions.

In chapter 5 the main results of this thesis are shown. The measurement protocol, inclusion criteria and classification algorithm used to account for malignancy of lesions are presented as well as the outcomes and discussion.

Chapter 6 describes some preliminary results obtained with the combination of multispectral technology and 3D, also available in the multiphotonic platform.

Chapter 7 and 8 contain the most relevant conclusions of this work and lines of future research.

Finally, the bibliography used in this thesis and the appendices containing the data sheets of components, the instrumentation used and the user manual of the multispectral system, are presented.

---

## 2. State of the art

---

In this chapter, a detailed view of the spectral imaging technology is presented first as well as the different approaches to spectral sampling and sensors included in such systems. Then, the spectral data management and metrics used to evaluate their performance in terms of spectral and colour quality are explained. Finally, several applications of spectral imaging systems are shown, paying special attention to those used for skin cancer detection and diagnosis.

### 2.1. Spectral imaging systems

In general, a spectral imaging system is defined as that having an image sensor attached to a spectrometric device, which allows the reflected or transmitted light from a sample to be measured through several spectral bands of the electromagnetic spectrum range with high spatial resolution [8], [9].

Although a standard classification has not been established yet, spectral imaging systems are often classified taking into account the amount of spectral bands or acquisition channels they include. In this way, a monochromatic system contains only one spectral band, a trichromatic system three (R, G, B), a multispectral system between 4 and 9, and a hyperspectral one from 10 to hundreds of bands. Other authors refer to hyperspectral systems as those having a large number of bands very close one to each other and, therefore, a really good spectral resolution [10], [11].

Accordingly, a spectral image is a collection of images taken through several spectral bands which are spatially aligned [12]. The bands correspond to the total number of wavelengths available in the system. For instance, in a camera with sensitivity in the visible range (VIS) (380 nm - 780 nm) and a sampling step of 5 nm, a total of 81 bands will be available [13].

When using a spectral imaging system, the spectral resolution of an image refers to the number and width of the electromagnetic bands measured by the spectral camera, and the spatial resolution is defined as the level of spatial detail represented in this image [14].

The sum of a data set resulting from a spectral imaging system is the spectral datacube that is defined by two spatial ( $x, y$ ) and an additional wavelength dimension ( $\lambda$ ). In fact, this cube can be considered a stack of images, one for each band centred at a specific wavelength ( $\lambda_i$ ). And from it, it is possible to obtain spectral features of the scene under analysis and for each pixel individually, which can then be used as a “spectral signature or fingerprint” of materials or chemical compounds, as is depicted in Figure 2.1 [12], [15]–[18].

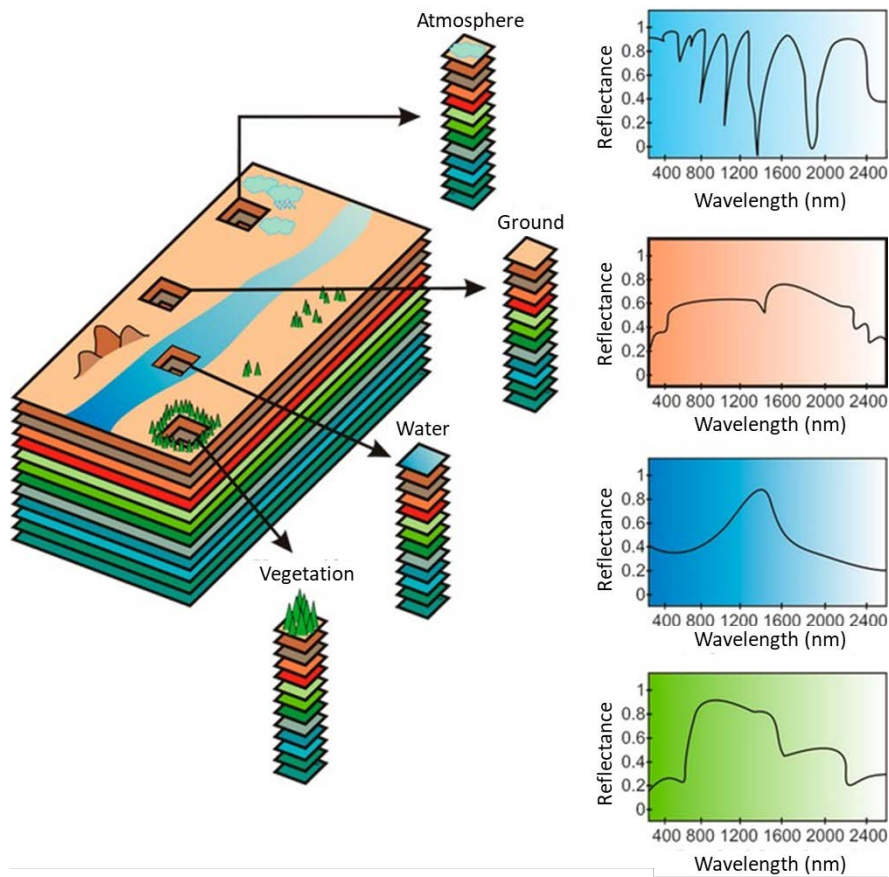


Figure 2.1 Spectral cube of the Earth's surface. The spectral signatures or fingerprints from several areas are shown on the right [19].

In general, spectral imaging systems can only obtain simultaneously two of the three dimensions of the spectral datacube at a time leading to the need of including a displacement system allowing for a temporal scanning. Thus, it is possible to distinguish three main types of systems for the collection of the whole spectral datacube; the point scanning systems (or whiskbroom) perform the spectral measurement of a single point at a time and then scan the whole area of the scene point by point; the line scanning systems (or pushbroom) carry out a simultaneous spectral measurement of an entire line of the scene and then perform a linear spatial scanning in only one direction; and the area scanning systems (or staring imagers) capture the entire image of the scene in a specific spectral band and then perform a spectral scanning process along all wavelengths [18], [20] (Figure 2.2).

The point scanning or whiskbroom system configuration shown in Figure 2.3 acquires the whole spectral data of one single point. Light originating from this point is separated into different wavelengths by a spectrometer and detected by a linear array sensor. Once spectral acquisition is completed, the spectrum of another point can be recorded. Scanning has to be performed in both spatial directions to build the spectral cube. Consequently, this method is very time-consuming and requires a complex configuration for the spatial scanning over the sample. [18], [20].

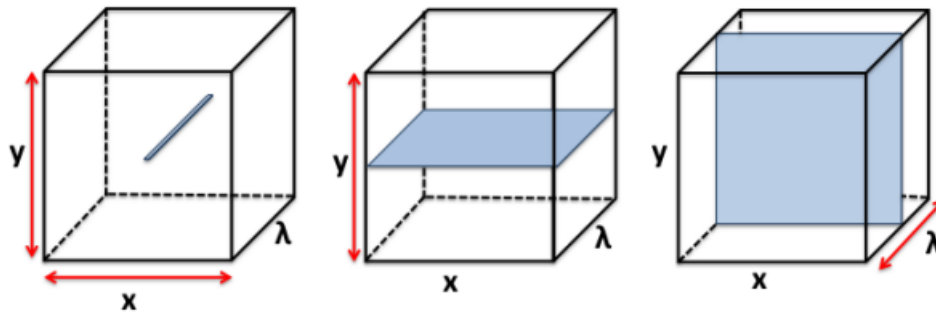


Figure 2.2 Methods for acquiring the spectral datacube: point scanning (left), line scanning (centre), and area scanning (right) systems. The spectral datacube contains two spatial ( $x$ ,  $y$ ) and one spectral ( $\lambda$ ) dimension. Blue areas represent data acquired simultaneously. Red arrows represent temporal scanning required to complete the datacube [18].

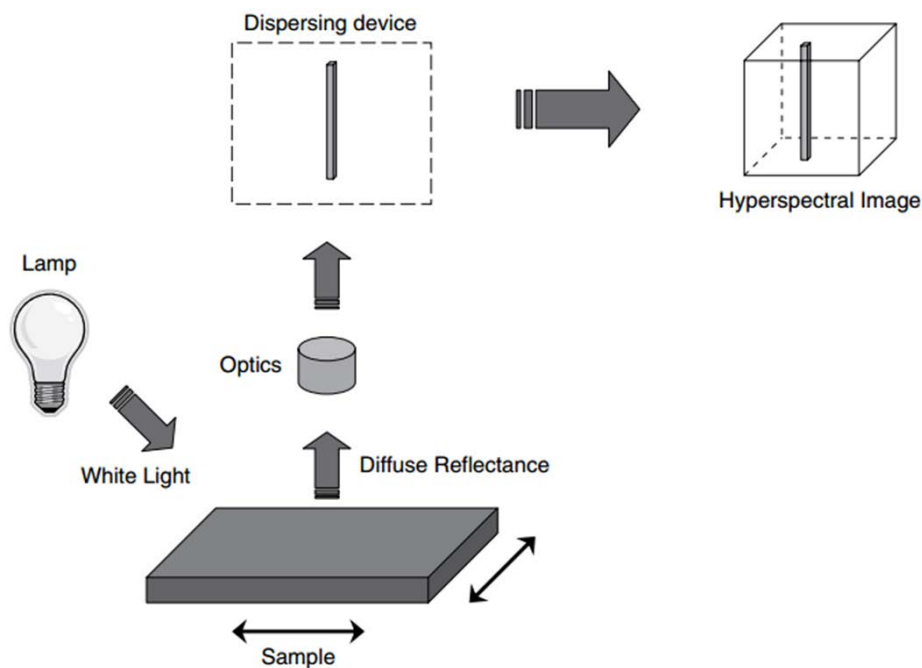


Figure 2.3 Whiskbroom system layout [20].

The line scanning or pushbroom system obtains simultaneously spectral information from one line instead of a single point. In this case, the light is dispersed onto a two-dimensional array sensor by means of a diffraction grating or a prism. In this way, a two-dimensional data matrix with the whole spectral dimension and one spatial dimension is acquired. The rest of the spatial information of the spectral cube is achieved by scanning across the specimen surface in a direction perpendicular to the imaging line. Therefore, pushbroom systems are generally faster than whiskbroom but the scanning process is still necessary (Figure 2.4)[20].

The area scanning systems or staring imagers capture a two-dimensional data matrix (full resolution image) of a scene at one spectral channel at a time (Figure 2.5). A complete spectral cube is obtained by collecting a sequence of these images. The spectral band of

## 2. STATE OF THE ART

---

incoming light in this configuration is typically modulated using a tuneable filter or a filter wheel. [20]. This configuration is the most widespread spectral imaging system while the use of line scanning or pushbroom approach is increasing in the last few years.

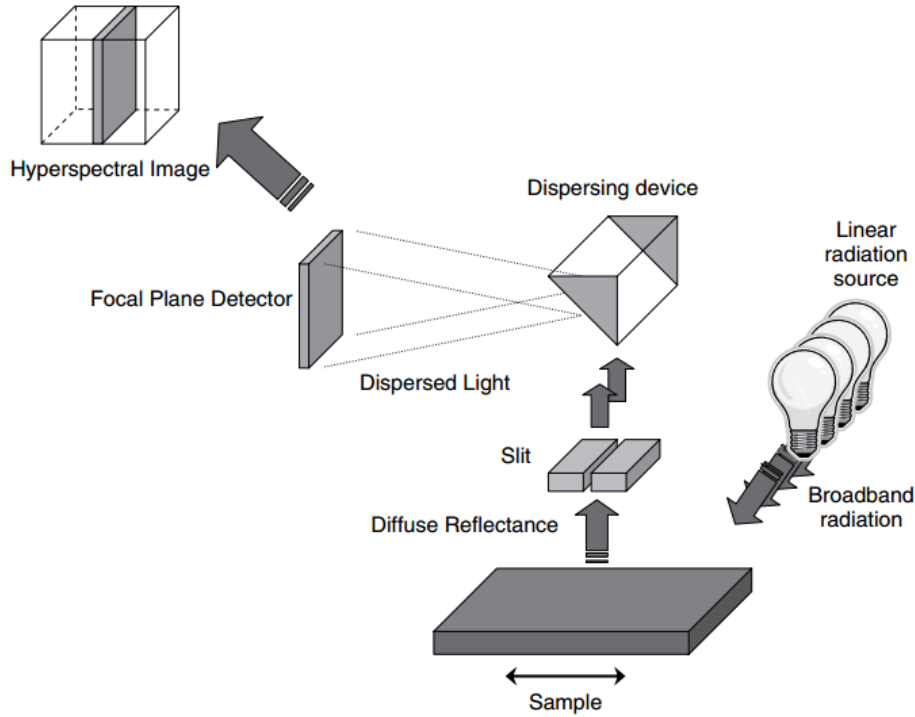


Figure 2.4 Pushbroom system layout [20].

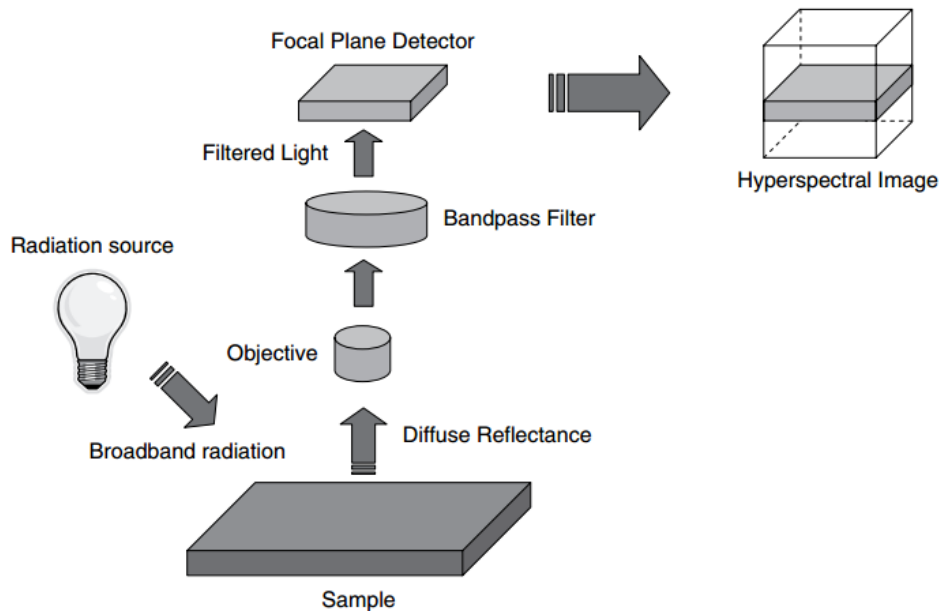


Figure 2.5 Staring imager system layout [20].

Finally, snapshot systems allow spectral information to be obtained in a single exposure (shot) on the camera sensor. These systems first capture a low-dimensional projection of

the original high-dimensional spectral data. The projection process can be represented as a sensing matrix that projects the spectral and spatial information into a low-dimensional measurement, which is then computationally decoded. To multiplex the spectral and spatial information in a solvable manner, the coded aperture-based undersampling schemes usually manipulate the original data matrix in two ways: shearing and spatial modulation. These two transforms effectively reorganize the entries of the data matrix and are operable in practice (shearing by a prism or diffraction grating, and spatial modulation by an occlusion mask, spatial light modulator, or digital micromirror device). Depending on their optical configurations and exploiting statistical properties of the spectrum data, each method employs different sampling strategies. These systems are thought to be used in fast biological processes which cannot be observed with scanning devices and the simultaneously recording of spectral and spatial information is needed [21], [22].

## **2.2. Spectral sampling techniques**

As mentioned in the previous section, staring imagers are nowadays the most widely used spectral imaging systems. They generally include a 2D monochrome imaging sensor as a CCD (Charge Coupled Device) or CMOS (Metal Oxide Semiconductor) camera attached to a dispersing element such as a tuneable filter or a filter wheel [20].

A temporal spectral scan is required in such systems to complete the spectral datacube. Generally, the collection of this information can be performed by using two different approaches: the passive variant, in which the light source has a wide spectral range and the dispersive elements or filters to configure the different spectral bands are placed in the optical path in front of the image sensor; and the active variant, in which the illumination itself is composed by different narrow spectral emission sources that provide several spectral bands.

### **2.2.1. Passive variant**

The spectral bands in the passive variant are achieved by interposing various filters with different transmittance in front of the camera sensor. Then, the spectral datacube is obtained by acquiring images through each of these bands sequentially.

Nowadays, the filters most widely used are based on electro-optical devices, such as liquid crystal tuneable filters (LCTF) and the acousto-optic ones (AOTF). With the emergence, mechanical systems based on filter wheels are no longer used because of the limitation on the number of filters, the need of mechanical moving parts to achieve the rotation, which often caused vibrations and could alter the picture quality, the big size and the poor portability of the system (Figure 2.6) [23].

LCTFs are based on the application of an electric field to the different elements of a liquid crystal that, with the use of polarizers, allow the transmission to be changed along a certain spectral range in a rapid and efficient way. The transmittance achieved corresponds to a single narrow spectral band that can be tuned in the VIS spectrum and

## 2. STATE OF THE ART

part of the near infrared (NIR); however, the transmission is generally low in the short wavelengths [8], [23], [24] (Figure 2.7).



Figure 2.6 Commercially available liquid crystal tuneable filter [25] (left), acousto-optic tuneable filter [26] (centre), and filter wheel [27] (right).

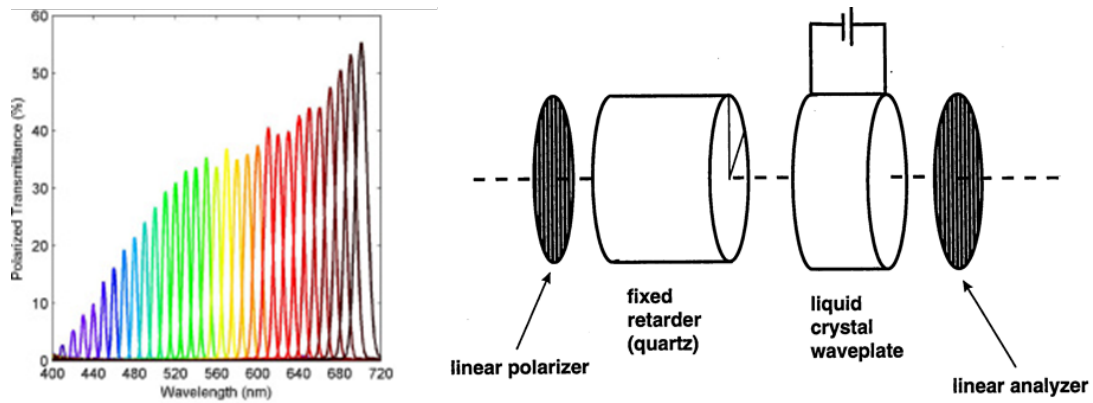


Figure 2.7 : Liquid crystal tuneable filter: spectral transmittances [28] (left) and main components [29] (right).

AOTFs consist of a quartz or a tellurium dioxide crystal attached to a transducer. In response to the application of an oscillating radio frequency signal, the transducer generates high frequency vibrational acoustic waves propagating through the crystal causing periodic changes in its refractive index. Therefore, light is diffracted depending on its wavelength. [23], [30], [31] (Figure 2.8).

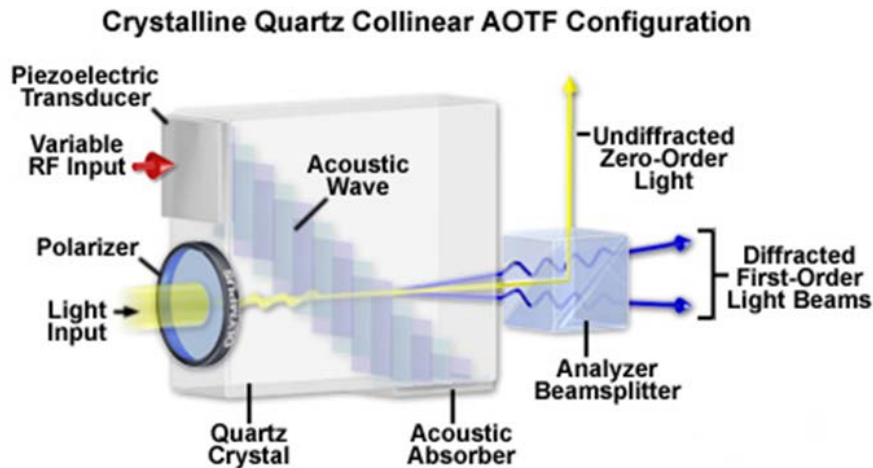


Figure 2.8 Main components of an acousto-optic tuneable filter (RF: radio frequency) [32].



### 2.2.2. Active variant

Unlike the passive variant, in the active variant the illumination itself is composed by different narrow spectral emission sources that provide the spectral bands or acquisition channels. This approach is feasible since the light emitting diodes (LEDs), which have a narrow spectral emission, are available on the market [33].

LEDs are solid-state devices that emit light when an electric current passes through them. They consist of a chip of a semiconductor material with impurities to create an anode-cathode junction. When it is directly polarized, the current flows from the anode to the cathode, the electrons cross the junction, and the recombination of electrons and holes produces photons in a process called electroluminescence [34].

The light emitted by an LED is rather monochromatic and ranges from the ultraviolet (UV) to the infrared (IR). Although its efficiency depends on the emitted wavelength, it can be generally considered as good. In addition, due to their low cost, small size, long durability and low energy consumption, the use of LEDs has become more popular in recent years, especially for lighting applications and in spectral imaging systems [34], [35].

### 2.3. Image sensors

The most used digital sensors in spectral imaging systems, especially in area scanning ones, are the CCD and CMOS cameras. From the 70s, the popularity of these sensors based on silicon has expanded rapidly due to their high image quality and resolution, quantum efficiency, wide spectral response, low noise, low power consumption and good durability. Both sensors convert incident photons into electrons, forming thus, an electrical signal proportional to the amount of light reached at every spatial location [36], [37].

When the exposure is complete in the CCDs, the charge of each pixel is sequentially transferred to a common output structure and converted into voltage, stored in a buffer and sent out of the chip as an analogue signal voltage. In this way, the whole pixel area can be devoted to capture light and therefore, the uniformity of the output signal is high, providing an accurate image quality. In contrast, each pixel of a CMOS sensor has its own charge-voltage conversion, and in addition, the sensor often includes amplifiers, noise correction and digital circuits, which allows that the output information are digital bits. In consequence, the design complexity increases and the area available to capture the signal reduces, providing a lower uniformity because of the non-uniformity in the pixel to pixel circuitry [37]–[39] (Figure 2.9). Nevertheless, CMOS and CCD have currently reached a similar level of performance, and consequently, CCDs are being now replaced by CMOSs due to the simpler manufacturing.

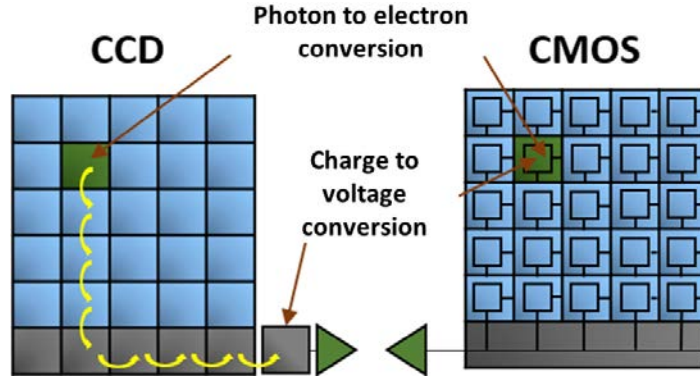


Figure 2.9 Scheme of transference process for CCD and CMOS sensors. Adapted from: [40].

### 2.3.1. Noise sources

The reliability of the information given by a spectral imaging system depends primarily on the quality of the data. Thus, the assessment and removal of noise requires special consideration before starting any kind of measurements [36], [41], [42].

The noise of a digital image sensor can be classified into two main groups: temporal and spatial. Temporal noise is caused by the random arrival of photons at the sensor and quantization and reading noise due to the analogue-digital conversion. Spatial noise is mainly the dark current noise produced by electrons which are excited due to the heat of the camera itself and the non-uniformity in the picture response, which is caused by small differences in sensitivity among pixels [38].

It is essential to reduce the maximum noise sources in any imaging system, especially in applications that need accuracy and resolution. Temporal noise can be decreased with image averaging due to its random nature, and spatial noise through the application of a uniform field correction (flat fielding). The flat fielding is a procedure done through capturing a dark image with the sensor covered and the so-called “base image”, which corresponds to a uniform light sample. This image has to be acquired under the same conditions of temperature, exposure time and position as the image to be corrected. In this way, the basic process of calibration is described mathematically by the equation [43]–[46]:

$$DL_c(i,j) = k \frac{DL(i,j) - DL_0(i,j)}{DL_B(i,j) - DL_0(i,j)} \quad (2.1)$$

where  $DL(i,j)$ ,  $DL_0(i,j)$  and  $DL_B(i,j)$  are the digital level of the image to be corrected in the pixel  $(i,j)$ , the dark image and the base image, respectively, and  $k$  is a calibration constant estimated as the average digital level image resulting from the difference between the base image and the dark image [47], [48].

Even though correcting much of the noise, CCD and CMOS sensors tend to decrease their performance permanently due to the total dose of ionizing and the displacement damage. The total ionization dose causes voltage changes, and the damage displacement reduces the efficiency of charge transfer, increases and produces irregularities in the dark current and creates more random noise in isolated pixels [49]. Therefore, a hot-pixel can be

defined as one in which the dark current is statically anomalous compared to the rest of pixels, generating excessive signal in the absence of illumination [50], [51]. In order to know the location of these hot-pixels, several algorithms can be used looking for those pixels with a digital level around twice above of the dark image average. Once located, they are corrected masking them by interpolation from the surrounding pixels and achieve a good image quality (Figure 2.10).

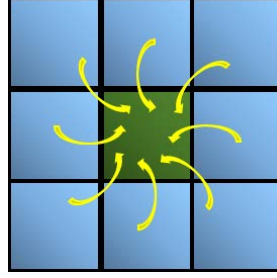


Figure 2.10 Interpolation used to mask a hot-pixel.

#### 2.4. Obtaining spectral and colour information from spectral imaging systems

Once the spectral datacube has been built, i. e., the spectral images at several wavelengths are available, spectral and colour information must be extracted from it.

Spectral reflectance images can be easily computed from the spectral images of the datacube by means of a variation of Eq. (2.1) [52], [53]:

$$Refl_{\lambda}(i,j) = R_{Gi\lambda} \cdot \frac{DL_{\lambda}(i,j) - DL_{\lambda_0}(i,j)}{DL_{\lambda_B}(i,j) - DL_{\lambda_0}(i,j)}, \quad (2.2)$$

where  $Refl_{\lambda}(i,j)$  is the spectral reflectance estimated corresponding to a specific pixel  $(i,j)$ ,  $DL_{\lambda}(i,j)$  the digital level of the original image,  $DL_{\lambda_0}(i,j)$  the digital level of the dark image,  $DL_{\lambda_B}(i,j)$  the digital level of the base image - in this case a uniform and calibrated sample -, and  $R_{Gi}$  the reflectance of the calibrated sample provided by the manufacturer, all them for a certain wavelength  $(\lambda)$  available in the spectral datacube. Again, all images must be taken with the same configuration, under the same illumination and position conditions.

From the spectral reflectance, colour coordinates can be also calculated pixel by pixel. In this context, the colour space XYZ CIE-1931 defined by the CIE (Comission Internationale de l'Éclairage) is one of the most widely used [11]. In this colour space, each colour is represented by three tristimulus values called X, Y and Z which are related with the amount of primaries needed to match the stimulus, and are defined as follows:

$$X = k \sum_{\lambda} S_{\lambda} Refl_{\lambda} \bar{x}_{\lambda} \Delta\lambda, \quad (2.3)$$

$$Y = k \sum_{\lambda} S_{\lambda} Refl_{\lambda} \bar{y}_{\lambda} \Delta\lambda, \quad (2.4)$$

$$Z = k \sum_{\lambda} S_{\lambda} \text{Refl}_{\lambda} \bar{z}_{\lambda} \Delta\lambda, \quad (2.5)$$

$$k = \frac{100}{\sum_{\lambda} S_{\lambda} \bar{y}_{\lambda} \Delta\lambda}, \quad (2.6)$$

where  $S_{\lambda}$  is the spectral emission of the light source used to light the sample,  $\bar{x}_{\lambda}$ ,  $\bar{y}_{\lambda}$ ,  $\bar{z}_{\lambda}$  are the colour matching functions of the CIE 1931 standard observer (for visual angles between 1° and 4°) or the CIE 1964 standard observer (for larger visual angles) and  $\Delta\lambda$  is the wavelength step.

However, when the main objective is to assess colour differences between colours, the uniform CIELAB colour space defined by CIE in the 1976 is more convenient [54]–[57]. In this colour representation space the colour coordinates are:

$$L^* = 116f\left(\frac{Y}{Y_W}\right) - 16, \quad (2.7)$$

$$a^* = 500 \left[ f\left(\frac{X}{X_W}\right) - f\left(\frac{Y}{Y_W}\right) \right], \quad (2.8)$$

$$b^* = 200 \left[ f\left(\frac{Y}{Y_W}\right) - f\left(\frac{Z}{Z_W}\right) \right], \quad (2.9)$$

where:

$$f(\omega) = \omega^{\frac{1}{3}} \quad \text{if } \omega > (24/116)^3, \quad (2.10)$$

$$f(\omega) = 7,787\omega + 16/116 \quad \text{if } \omega \leq (24/116)^3, \quad (2.11)$$

$L^*$  is the lightness and can have values from 0 (black) to 100 (white),  $a^*$  represents the red-green component, and  $b^*$  corresponds to the yellow-blue component. The  $X_W$ ,  $Y_W$  and  $Z_W$  are the tristimulus values for the reference white used that can either be the D65, A or any standard illuminant defined by the CIE.

If the former cartesian coordinates are converted into cylindrical ones, we obtain:

$$C_{ab}^* = \sqrt{(a^*)^2 + (b^*)^2}, \quad (2.12)$$

$$h_{ab} = \arctg\left(\frac{b^*}{a^*}\right), \quad (2.13)$$

where  $C_{ab}^*$  is the chroma and  $h_{ab}$  the hue angle expressed between 0° and 360° (Figure 2.11).

From the previous description it is clear that provided spectral imaging systems give a spectral datacube in terms of digital levels, later any kind of image can be computed in terms of reflectance values, colour coordinates, etc.

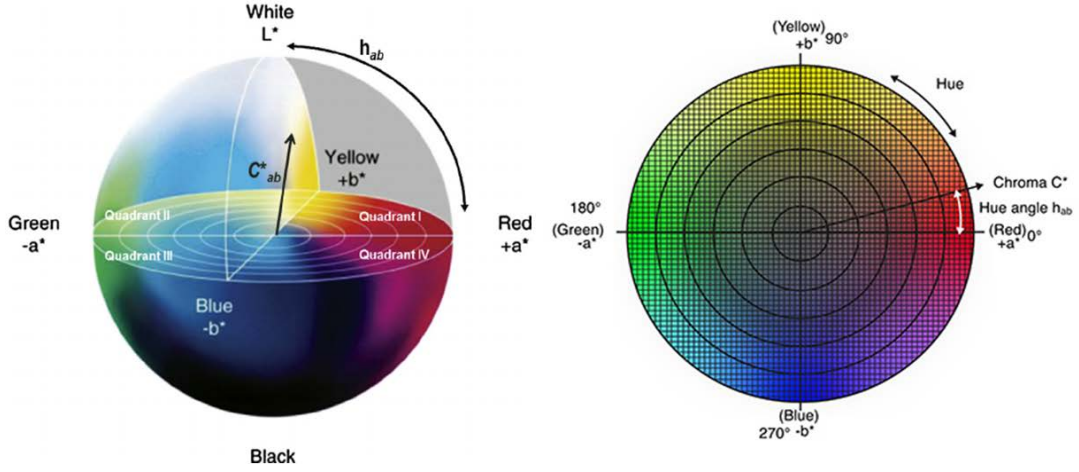


Figure 2.11 space: 3D representation [58] (left), and spatial projection for a constant lightness value [59] (right).

## 2.5. Metrics used for the evaluation of spectral and colour differences

From the reflectance and colour representation described above, there are several ways to measure the spectral and colour deviations between a pair of samples. They are explained next [60].

### 2.5.1. Spectral differences

One of the most common metrics used when spectral curves are to be compared is the RMSE (Root Mean Square Error) [61], [62]:

$$RMSE = \sqrt{\frac{\sum_{\lambda_1}^{\lambda_n} (Refl1_{\lambda_i} - Refl2_{\lambda_i})^2}{n}}, \quad (2.14)$$

where  $Refl1_{\lambda_i}$  and  $Refl2_{\lambda_i}$  refer to the reflectance values of the two samples compared at a specific wavelength, and  $n$  represents the number of wavelengths in which differences are evaluated. For a perfect match between both curves, the RMSE should be zero while in the worst case it tends to infinity.

Alternatively, the GFC (Goodness-of-Fit Coefficient) parameter can also be used, which is based on the Schwartz inequality:

$$GFC = \frac{|\sum_{\lambda_1}^{\lambda_n} (Refl1_{\lambda_i} Refl2_{\lambda_i})|}{\sqrt{|\sum_{\lambda_1}^{\lambda_n} (Refl1_{\lambda_i})^2|} \sqrt{|\sum_{i=1}^{\lambda} (Refl2_{\lambda_i})^2|}}, \quad (2.15)$$

GFC ranges from 0 to 1, where 1 indicates a perfect match [62]. According to the scale commonly linked to this parameter, a  $GFC \geq 0.995$  is considered “colorimetrically accurate”, a  $GFC \geq 0.999$ , a “good spectral fitting” and a  $GFC \geq 0.9999$ , an “excellent spectral fitting” [63].

2.5.2. Colour differences

Colour differences can be easily computed in the CIELAB space as the Euclidean distance between two points (or colour stimuli) [54]:

$$\Delta E_{ab}^* = \sqrt{(\Delta L^*)^2 + (\Delta a^*)^2 + (\Delta b^*)^2}, \quad (2.16)$$

This equation can also be expressed in terms of polar coordinates:

$$\Delta E_{ab}^* = \sqrt{(\Delta L^*)^2 + (\Delta C_{ab}^*)^2 + (\Delta H_{ab}^*)^2}, \quad (2.17)$$

where:

$$\Delta H_{ab}^* = [(\Delta E_{ab}^*)^2 - (\Delta L^*)^2 - (\Delta C_{ab}^*)^2]^{1/2}, \quad (2.18)$$

In practice, the CIELAB space is not entirely uniform although it is a good approach to colour perception for most of the samples under certain conditions of observation. However, as a means of improving the correlation achieved with perceptual estimates, the CIE has recently proposed new formulas to calculate colour differences. The CIEDE2000, which was proposed by Luo et al., 2001 [64] includes weighting coefficients among others to improve the results for blue, dark and neutral colours [65], [66].

Based on the CIELAB space, the Individual Typology angle (ITA) is a parameter often used in the literature to classify the skin colour types in the field of dermatology. In fact, this parameter allows classifying the skin into six different groups: from very light to dark skin types (Figure 2.12). ITA is computed as follows [67]:

$$ITA(^{\circ}) = \left[ \arctan\left(\frac{L^* - 50}{b^*}\right) \times \frac{180}{\pi} \right], \quad (2.19)$$

It can be thought as a customized “hue angle”, similarly to  $h_{ab}$  from the CIELAB, valid to describe common hues of the skin.

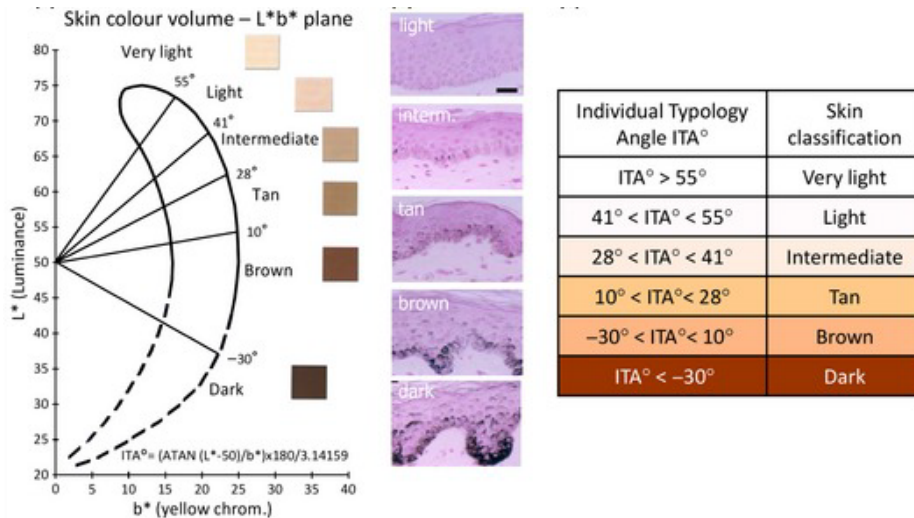


Figure 2.12 ITA examples for different skin types with the corresponding histologies (left), and scale used for classification (right) [67].

## 2.6. Textural analysis

The output of spectral imaging systems are images and thus, they can be used to study the spatial distribution over the samples or texture besides their spectral and colour features.

A frequently used approach to study texture of samples is based on the statistical properties of the image histogram, which encompasses from first to second or even higher order statistics. This strategy has been used to process photomicrographs of sandstones, superconductors, human cholesterol and microprocessors, aerial and satellite images [68], [69], and images of the human iris [70]. These statistical descriptors can be extended to any kind of image that, as previously stated, can be in terms of digital levels, reflectance, colour coordinates, spectral and colour differences, or any other parameter.

The first order statistics performs general evaluations of the histogram, without any consideration on the relationship among neighbouring pixels. A clear example of these measures are statistical moments, for instance the mean ( $m$  or  $\mu$ ), the variance ( $\sigma^2$  or  $\mu_2$ ), whose positive square is the standard deviation ( $\sigma$ ), and the third central moment, also called skewness ( $\mu_3$ ) [71]–[73]:

$$m = \sum_{i=0}^{n-1} i P_i, \quad (2.20)$$

$$\sigma = \sqrt{\mu_2} = \sqrt{\sigma^2}, \quad (2.21)$$

$$\mu_3 = \sum_{i=0}^{n-1} (i - m)^3 P_i, \quad (2.22)$$

where  $P_i$  is the relative frequency of the bin  $i$  of the histogram, and  $n$  is the number of bins or intervals that the histogram is divided into.

A positive/negative value of the  $\mu_3$  parameter means that the histogram is skewed to the right/left about the mean, while it is 0 for symmetric histograms.

Other texture descriptors that are usually employed are the energy ( $En$ ) and the entropy ( $Ep$ ) of the histogram:

$$En = \sum_{i=0}^{n-1} P_i^2, \quad (2.23)$$

$$Ep = - \sum_{i=0}^{n-1} P_i \log_2(P_i), \quad (2.24)$$

Energy is a numerical descriptor of the image uniformity that ranges between 0 and 1, reaching the maximum value for a constant image. On the other hand, entropy is a well-

known statistical measure of randomness, uncertainty or disorder in image values, being 0 the minimum value for a constant image, and  $\log_2(n)$  the maximum.

### 2.7. Applications of spectral imaging systems

The first applications of spectral imaging systems were made in the field of remote sensing, related to studies of the Earth's surface; mostly to create maps of specific areas through capturing satellite images or from airplanes [14], [74] (Figure 2.13 left) or to perform studies on atmospheric or even outer space phenomena; Montmessin et al. 2007).

Another field of application of such systems is culture heritage, as they are non-invasive. Examples of such applications include the analysis and conservation of paintings and manuscripts, monitoring of buildings' surfaces [76], the study of archaeological materials [23], the detection of small vertebrate fossils [77], among others. Due to the large number of spectral bands that some of these systems have, it is possible to measure accurate spectral properties and colour from non-uniform samples as paints, allowing thus, the identification of pigments and inks used, the monitoring and evaluation of conservation treatments, and the image digitalization for documentation and archiving [23], [31] (Figure 2.13 right).



Figure 2.13 Examples of spectral information obtained from different spectral imaging systems: images over Cuprite (Nevada, USA) obtained from the AVIRIS imaging spectrometer with a spectral range from 400 nm to 2500 nm and used to measure and monitor the components of the Earth's surface [74] (left). The monochrome image corresponds to a specific spectral image and the pseudo-coloured image to the mineral distribution of alunite or kaolinite obtained from several bands. Spectral monochromatic images corresponding to 640 nm and 1000 nm, respectively, of a Byzantine painting (right). In the 1000 nm image some corrections of the hand's virgin can be observed [23].

Spectral imaging systems have started to be used recently in the quality control of various industries. In the food industry VIS and IR systems have been used for the study of cucumbers [78], mandarin affected by *Penicillium digitatum* [79] (Figure 2.14 left), bruises on apples [52] (Figure 2.14 right), properties of some fruits and vegetables [16], [80] or the beef tenderness [81]. Other industrial applications are the measurement of the amount of unwanted material in the cotton textile industry [82], the assessment of the density and moisture on wood [83] and the sorting of solid waste particles for further recycling such as glass, plastic etc. [84].



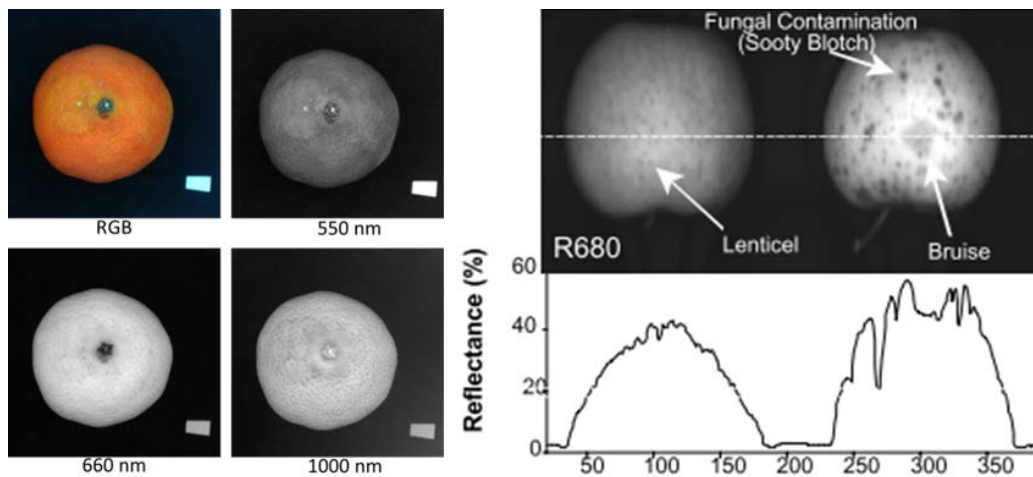


Figure 2.14 Spectral images of a mandarin acquired at 550, 660 and 1000 nm with a VIS and a NIR LCTF [79] (left), images and intensity profiles of two apples at 680 nm where the irregularities in the plot of the right apple indicates a fungal contamination [85] (right).

Another area in which much research is being done nowadays with this type of systems is the forensic science. Spectral imaging systems seem to be able to improve significantly the detection, visualization, identification and age estimation of forensic traces without destroying or contaminating them, such as fingerprint, hair, strokes, blood and fibres [18] (Figure 2.15).

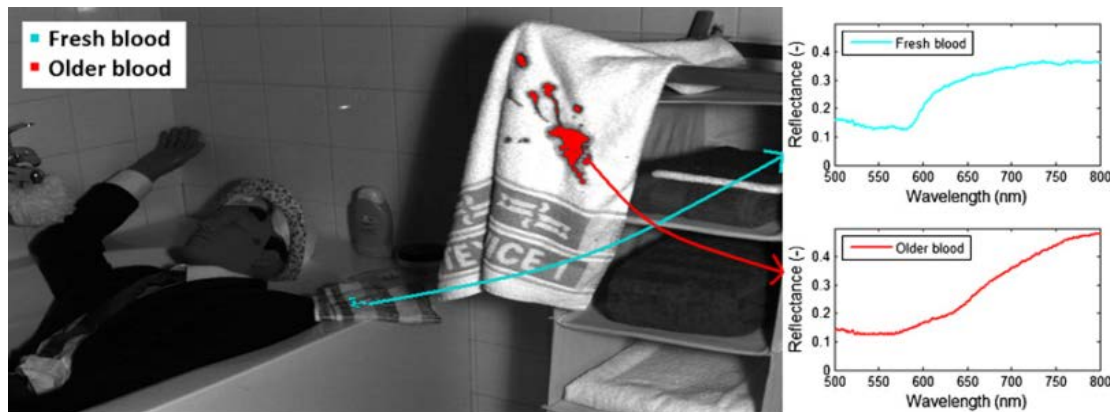


Figure 2.15 Simulation of a crime scene, in which fresh and older blood stains were automatically detected based on their reflectance and coloured in blue and red, respectively [18].

In addition to the applications described above, the field that has more open research lines in regard to spectral imaging systems is biomedicine. Examples range from the spectral analysis through a microscope to obtain information on tissue allowing different molecules to be differentiated despite being superimposed [86]; the detection of subcutaneous veins for the insertion of intravenous catheters with the aid of a NIR source [87]; the oxygen blood flow and saturation measurement and the intracellular calcium dynamics assessment [88], [89]; and systems for the diagnosis of retinal diseases and the oxygen saturation maps

measurement [90]–[92] (Figure 2.16). Other medical applications include the diagnosis of diseases through the spectral study of the tongue [93] and the diagnosis of cancer.

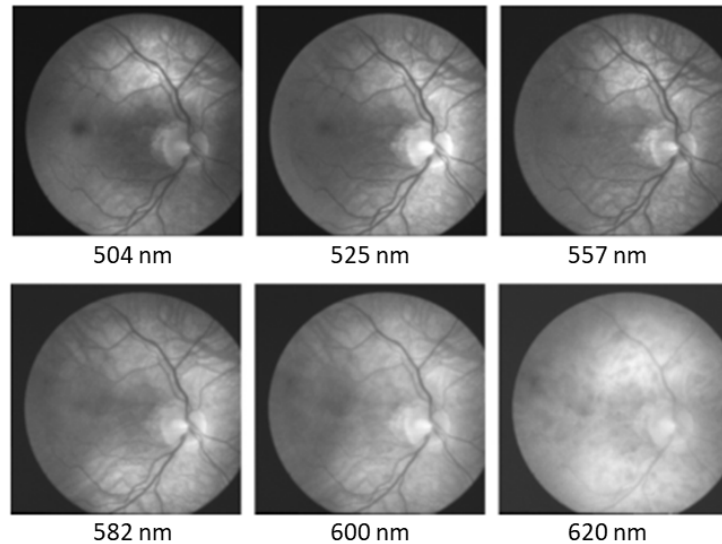


Figure 2.16 Images of the retina at several wavelengths from a spectral imaging system based on LEDs [90].

In this context, attempts have been made to achieve automatic detection of white blood cells in the bone marrow [94], improve diagnosis of prostate cancer [95], cervical cancer [96] or gastric cancer [97], among others. Furthermore, spectral imaging systems have also been used in the detection of skin cancer lesions and they are explained next, as they are the closest application to the scope of this thesis.

### 2.7.1. Spectral imaging systems for the skin cancer detection

As stated in the introduction, clinical (naked eye) and dermoscopy are the conventional techniques used for the diagnosis of skin cancer, but in most cases they are not enough sensitive for the detection of small and early malignancy. This means that there are lots of false positives due to the lack of adequate tools and that better detection and diagnostic tools are still demanded [98].

Skin is composed of several structures and components, such as blood, fat or melanin pigment, among others. Although optical properties of the skin vary from person to person, the 2-layer model from Ohtsuki and Healy can be assumed [99]; it states that the surface reflectance, which takes place at the epidermis, is about 5% of the incident light, independently of the light wavelength and the human race. The rest of the incident light (95%) enters deeper into the skin and becomes absorbed and/or scattered within the epidermis and dermis (Figure 2.17).

The absorption, and therefore the colour of the skin, is mainly caused by groups of organic molecules called chromophores, such as melanin, haemoglobin, water, beta-carotene, collagen and bilirubin; although the last three are not very significant [100], [101]. Melanin absorbs much of blue light and thus it is perceived as brown (Figure 2.18) while

haemoglobin absorbs mostly blue and green wavelengths with peaks at 400 and 550 nm; therefore, it has a reddish appearance. Spectral properties caused by these chromophores might differ among skin lesions of different etiologies.

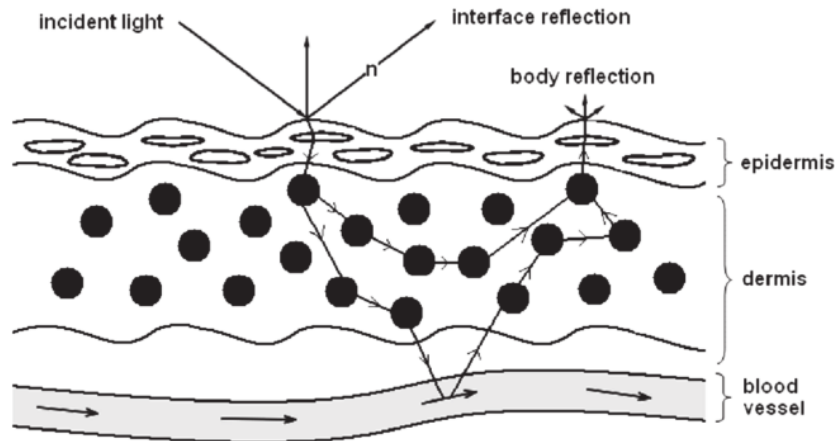


Figure 2.17 2-layer skin model from Ohtsuki and Healy [99]

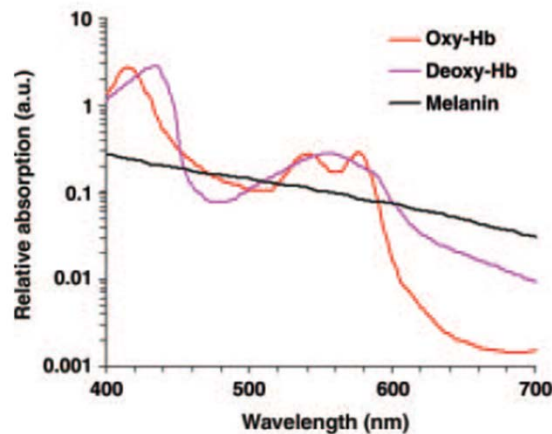


Figure 2.18 Absorption of oxy-, deoxyhaemoglobin and melanin [102].

According to all this, colour and spectral imaging technology that enhances and analyses spectral properties of the skin are currently being explored to improve early detection and diagnosis of skin cancer (Figure 2.19) [103]. However, most of them only use three spectral bands in the VIS range (typically three colour RGB channels), which limits their spectral resolution, and an additional one located at the NIR range. Notably, most tools only analyse the averaged colour and spectral properties.

In this context, commercial devices such as SIAScope [104] and MelaFind [105] have already been proposed as tools for improving skin cancer diagnosis. The SIAScope V<sup>TM</sup> system, sold together with the MoleMate<sup>TM</sup> program [98], [106], [107], consists of a 4-spectral bands system (blue, green red and IR). The system provides the distribution maps of haemoglobin, collagen and melanin, and the latter identifies whether the melanin is from the epidermis or the dermis (dermis location indicates that the melanoma is expanding and could reach the bloodstream and thus spread). Regarding the MoleMate<sup>TM</sup> program, it is

ready to be used by non-specialist physicians in identifying melanomas with a previous training for interpreting the images. It is based on a diagnostic tree monitoring in which not only the colour of the lesion is considered, but also the diameter, the presence of dermic melanin, the vessels of the lesion, or even the age of the patient. If the final score is equal or greater than 6, the lesion is considered as suspicious (Figure 2.20).

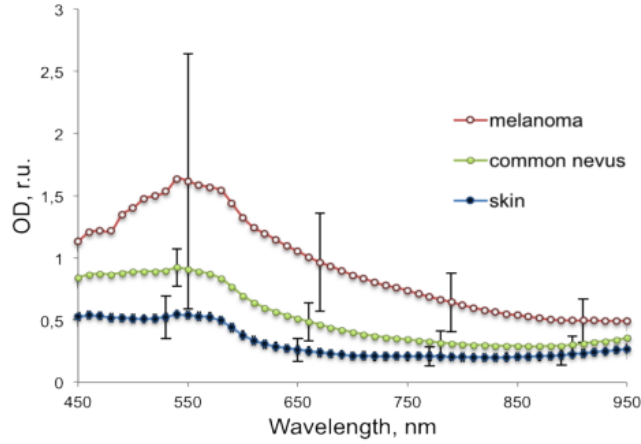


Figure 2.19 Mean spectral optical density of 17 melanomas, 65 common nevi and 82 healthy skin samples [103].

On the other hand, MelaFind® is a 10-wavelengths (430, 470, 500, 550, 600, 650, 700, 770, 880, 950 nm) imaging system; from the images acquired, 6 linear classifiers are used to differentiate melanomas from other pigmented lesions with 100% sensitivity such as common nevi, low-grade dysplastic nevi, congenital nevi, seborrheic keratosis, solar lentigos and pigmented basal cell carcinomas. They are trained by means of a database of approximately 10,000 excised lesions [108]. A lesion is recommended for biopsy if all the scores are above the threshold value [109]. After the measurement, the system provides a disorganization value and a treatment suggestion for dermatologists: positive or negative for high degree of morphological disorganization, where positive means the lesion should be considered for biopsy (Figure 2.21).

Besides the commercial devices described, prototypes such as those developed by Bekina et al. [110], Diebele et al. [103] and Kapsokalivas et al. [111] have also been proposed to improve skin cancer diagnosis.

The system from Bekina and colleagues [110] was composed of a commercial video-microscope which was modified and equipped with four different LEDs at blue (450 nm), green (545 nm), red (660 nm) and IR (950 nm) wavelengths. From the images acquired, the authors proposed the following calculations to resemble distribution maps of bilirubin (B), and erythema (E) (Figure 2.22):

$$E = I_{660}(i, j) / I_{545}(i, j) \quad (2.25)$$

$$B = I_{450}(i, j) / I_{660}(i, j) \quad (2.26)$$

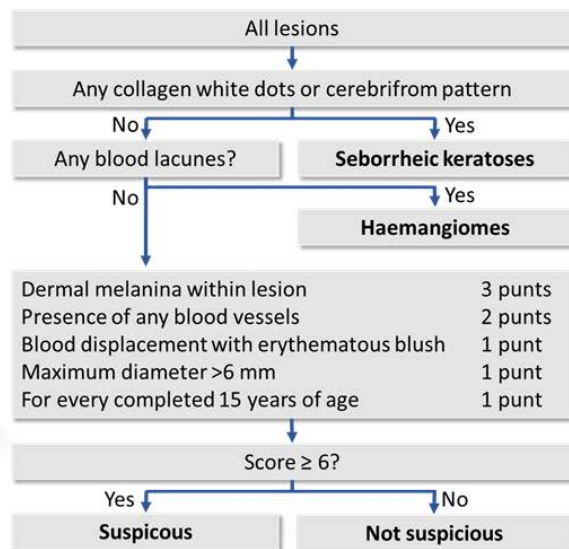
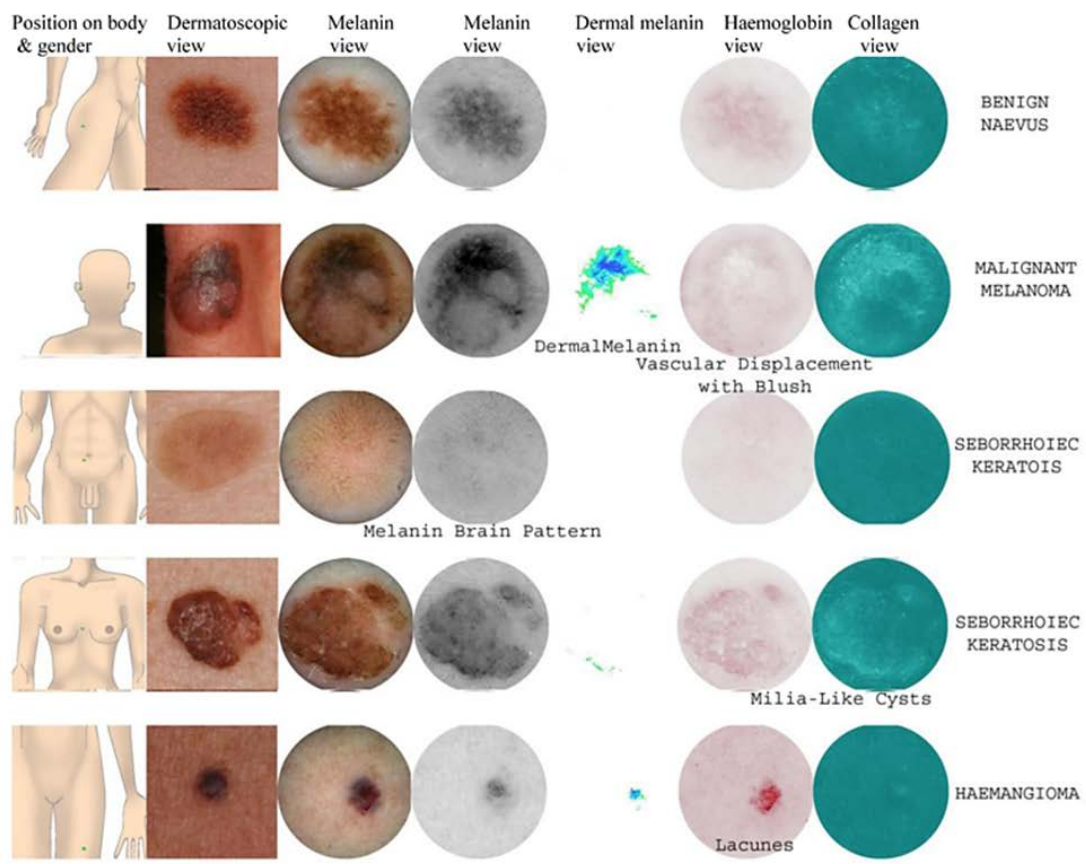


Figure 2.20 Distribution maps measured with the SIAscope V™ [104] (top), system and MoleMate™ program [112] (bottom left), and scoring algorithm based on a diagnostic tree [98] (bottom right).

## 2. STATE OF THE ART

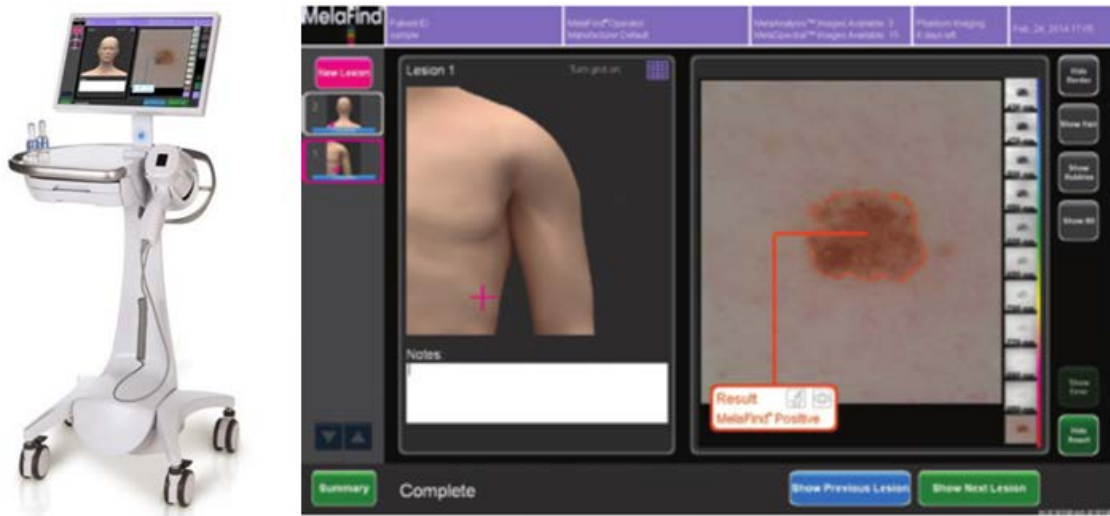


Figure 2.21 Melafind® system [113] (left) and software screenshot [108] (right).

where  $I_{545}$ ,  $I_{660}$  and  $I_{940}$  are the intensities of the diffuse light reflected from the skin at these wavelengths.

Furthermore, the system also provided a fluorescence map obtained by the irradiation with blue light.

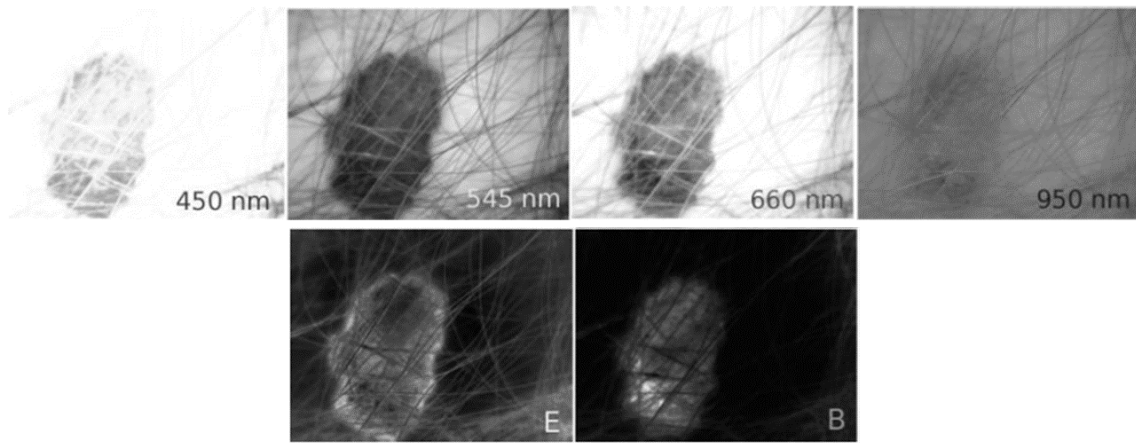


Figure 2.22 Spectral images at 450, 545, 660 and 940 nm (top), and maps of a melanoma (E: erythema, B: bilirubin) (bottom) [110].

Moreover, the same authors developed a similar system [103] that consisted of a multispectral imaging system with a CCD imaging sensor and a LCTF (from 450-950 nm in steps of 10 nm) (Nuance EX), a spectral optimized lens and internal optics. The illumination system was a ring of halogen lamps with a polarizer orthogonal to the camera in order to remove the artifacts caused by light reflection. In order to differentiate between melanoma and nevi, a new parameter was suggested:

$$p = k \cdot (I_{540}(i, j) / (I_{650}(i, j) * I_{950}(i, j))) \quad (2.27)$$

where  $k$  is the intensity coefficient that describes the white etalon reference used for the calibration of the system. The parameter  $p$  was calculated for each pixel, and then parametric  $p$ -images. Furthermore, a clinical study in a small group of skin lesions, 17 of which corresponded to melanomas and 65 to benign lesions (nevi), was conducted. The results suggested that, in general, the parameter  $p$  was higher for melanomas (Figure 2.23).

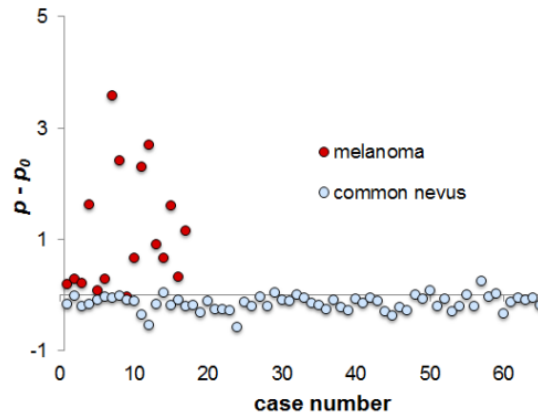


Figure 2.23 Scatter plot with the averaged parameter  $p$  for nevi and melanomas subtracted by the same parameter of the surrounding healthy skin of the patient ( $p_0$ ) [103].

Kapsokalyvas, et al. [111] also developed a prototype for the analysis of skin lesions composed of a CMOS camera and a light source. The illumination consisted of 3 LEDs emitting at 470, 530 and 625 nm with a polarizer in front of it. The lesion under analysis was placed on a glass window optically coupled by means of a drop of water. Furthermore, an analyser was placed in front of the camera mounted on a motorized rotator configured to rotate at  $0^\circ$  and  $90^\circ$  with respect to the polarizer. So, images containing reflected light from the first surface of the skin and images containing scattered light from deeper layers were obtained. Operating among these images, the authors provided distribution maps of melanin contrast to enhance pigmented structures of the skin, blood contrast to highlight the contrast of haemoglobin absorption and scattering contrast to enhance the structures with high scattering properties (Figure 2.24).

It should be remarked that not all devices described are able to diagnose by themselves, but an experienced dermatologist must interpret the data. Furthermore, many of them, especially MelaFind®, generate a large number of false positives and, consequently, a large number of unnecessary biopsies.

Besides spectral imaging systems, other non-invasive optical techniques have started to be used to aid in the diagnosis of skin cancer [114]. For instance, optical coherence tomography (OCT), which is an interferometric technique that generates images corresponding to transversal sections of the skin tissue in 2D or even in 3D through the measurement of the reflected light. This technique provides information of deeper structures of the skin and tumours as energy penetrates into the tissue around 2-3 mm [115]. Fluorescence spectrometry involving the use of ultraviolet energy to light the tissue, which is later reemitted at longer wavelengths depending of the skin fluorophores, might

## 2. STATE OF THE ART

---

also provide information of tissue composition, and therefore, it is now investigated as a means of distinguishing among different lesions types [116]. Raman spectroscopy, based on the scattering that occurs after exciting the molecules of samples with an IR laser beam is nowadays investigated to provide information of different chemical components present in skin lesions [117]. Finally, confocal microscopy, which provides vertical and horizontal images from the tissue with high contrast and good lateral resolution, is nowadays one of the most accepted complementary tools to improve skin cancer diagnosis [118]. More information on this technique is provided in the next chapter.

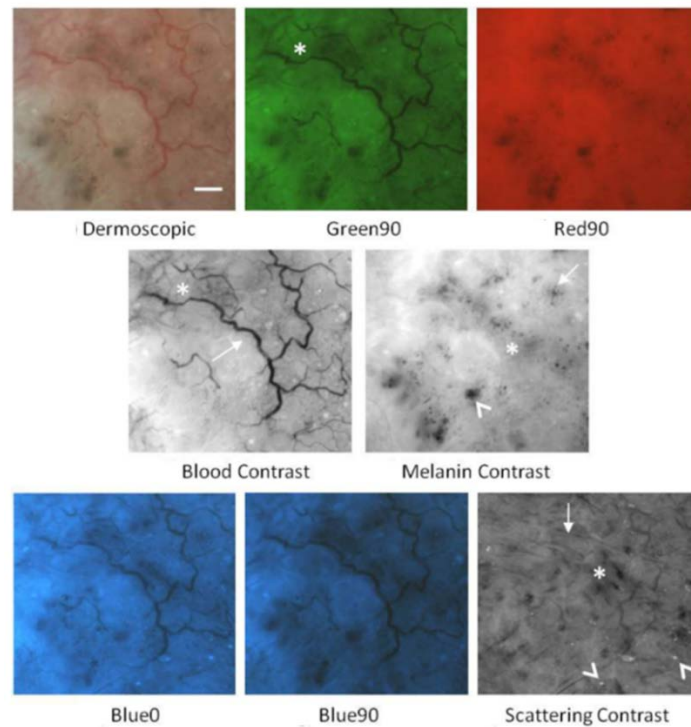


Figure 2.24 Spectral images and distribution maps of a malignant lesion (basal cell carcinoma) [111].



---

## 3. Experimental system

---

This chapter comprises the “Multiphotonic platform” section, which describes the system developed in the context of the European Project DIAGNOPTICS including several optical and photonic techniques for in-vivo imaging of skin cancer lesions; and the “Multispectral system” section, which explains with a particular emphasis the new multispectral imaging system based on LEDs developed in this doctoral thesis, including details of the components, design and performance, and some clinical issues related with the device that are relevant for its use in the hospitals.

### 3.1. Multiphotonic platform

As stated in the introduction, this thesis was part of the European Project DIAGNOPTICS seventh call for proposals 2013, CIP-ICT-PSP.2013.3.5; GA621066), the aim of which was to launch a hospital service to help in the detection and the prognosis evaluation of the skin cancer at earlier stages with novel optical and photonic technologies.

Besides examining the skin lesions from patients with conventional dermoscopy, physicians were asked to use a multiphotonic platform to complete the diagnosis of the lesion. Accordingly, the lesions suspicious of malignity were also examined with confocal microscopy (MAVIG VivaScope®), which helped to decide if the cytology of the lesion was needed; 3D technology, which provided topographic information of the skin lesion; optical feed-back interferometry (OFI) providing information of the amount of blood flow; and finally, multispectral imaging technology to obtain spectral information of the tissue at several wavelengths.

Two identical multiphotonic platforms were developed and simultaneously installed in two hospitals: Hospital Clínic i Provincial de Barcelona (Spain), and Università degli Studi di Modena e Reggio Emilia (Italy), where they were applied to over 600 patients.

The different systems included in the platform were assembled in a medical cart, as it can be seen in Figure 3.1. Each of the systems are briefly described in the next sections.

### 3. EXPERIMENTAL SYSTEM

---

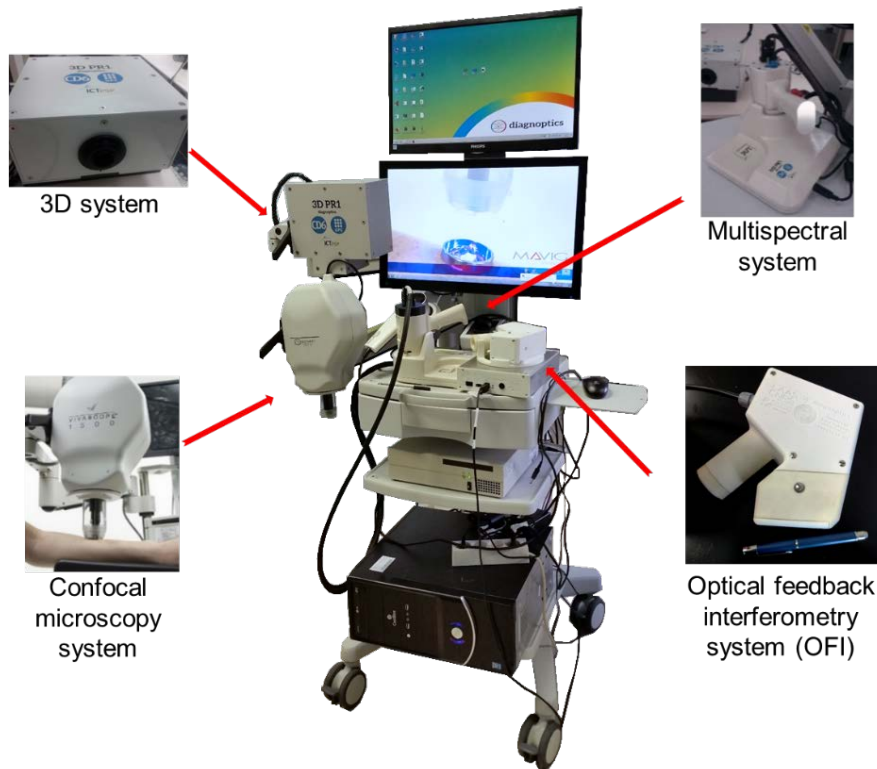


Figure 3.1 Medical cart with the confocal microscope, the OFI, the 3D and the multispectral systems.

#### 3.1.1. Confocal microscopy

Confocal microscopy is a modern medical imaging technology that serves as an additional non-invasive tool for the diagnosis of equivocal skin lesions including screening and diagnosis, image-guided biopsy, pre- and intraoperative mapping of tumour margins to guide surgery, and monitoring of treatment efficacy [119]. The system based on this technology (MAVIG VivaScope®) included in the platform allowed obtaining real-time maps of cells in grayscale images in which it was possible to observe the cellular size and shape, the epidermal structure, the dermal collagen morphology and the keratin with a zoom field of view of  $0.5 \times 0.5$  mm, i. e., with high optical resolution. Furthermore, information in different skin depths - one layer/depth at a time - as the epidermis and dermis skin layers, were also available [120].

The ability to acquire in-focus images from selected depths is achieved thanks to a pinhole placed in front of the detector. Light that scatters from the plane of focus is focused on the pinhole plane while light that scatters in other layers is imaged in a plane other than the pinhole and is blocked from reaching the detector. Images of an illuminated spot of few micrometers are acquired point-by-point, scanned all over the sample and reconstructed with a computer.

To generate confocal images with the available system, a laser beam at 830 nm is directed through an interconnected lens system including a beam splitter and onto the area of the skin to be examined. The laser beam reflected by the skin returns through the beam

splitter and hits the detector after crossing the pinhole. The light source, the illuminated spot on the skin, and the aperture opening of the detector are on optically conjugated focal planes, so they are confocally interconnected (Figure 3.2). As it can be seen, the confocal generates single images of tissue that are parallel to the tissue surface. The position of the single image inside the tissue can be changed by moving the objective lens up, down, or laterally, relative to the surface.

With a monochromatic laser illumination and a confocal optical system, the quality of the image is greatly enhanced over conventional microscopy because the image information from multiple depths in the specimen is not superimposed. A conventional microscope "sees" as far into the specimen as the light can penetrate, while a confocal microscope only "sees" images one depth level at a time, as formerly mentioned.

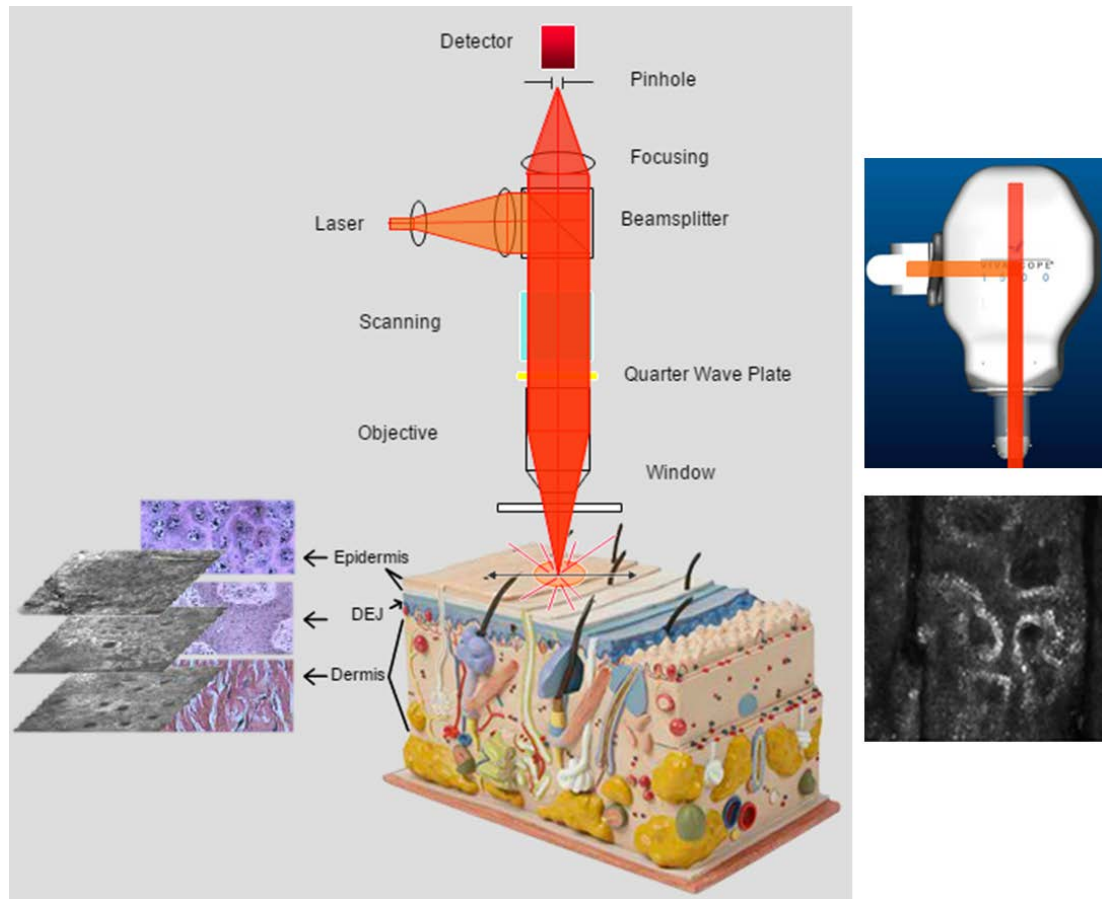


Figure 3.2 Confocal microscopic system (MAVIG VivaScope®) included in the multiphotonic platform: layout (left), picture of the head and image provided (right) [121].

### 3.1.2. 3D technology

The 3D system included in the platform used a stereoscopic optical technology which provides accurate 3D measurements of the human skin surface. It is worth noting that, nowadays, the palpation of the lesion is made in order to obtain clinical information of the lesion shape, border irregularity, and lesion diameter, and so, 3D information is expected to bring more knowledge on skin cancer.

### 3. EXPERIMENTAL SYSTEM

---

The system included in the platform was composed by two monochrome cameras placed in a standard stereo geometry, a light picoprojector and a colour camera, located both between the two monochrome cameras. All cameras had an objective lens with fixed focal length (25 mm) with a working distance of 110 mm, obtaining a field of view of 19x14 mm [122].

The principal measurement used is based on a stereovision technique combined with the projection of a sinusoidal pattern set shifted over the skin [123]. For each projected pattern, both monochrome cameras capture the images in a synchronized way and after the measurement, the skin is uniformly illuminated with the projector in order to acquire a colour image of the lesion. Afterwards, the phase maps are unwrapped based on the Goldstein algorithm which allows a good balance between a fast processing time and a good performance quality [124]. Finally, the corresponding phases between both cameras are identified and the 3D data is obtained by triangulation based on the epipolar geometry [125] and the calibration of the system previously computed (Figure 3.3).

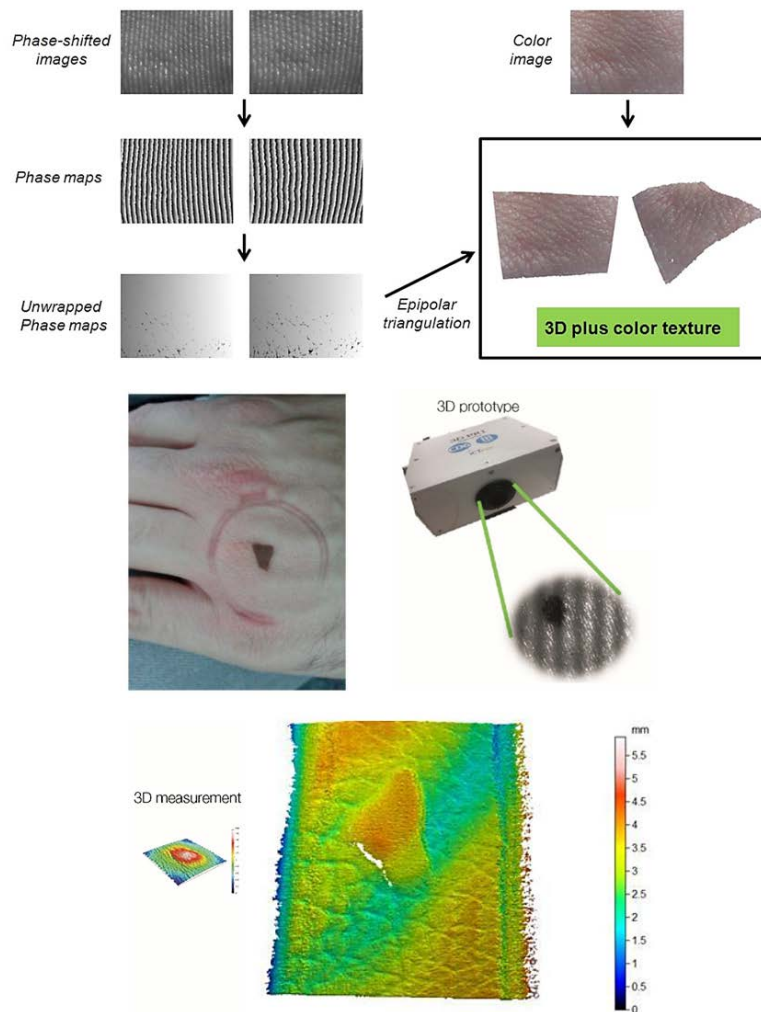


Figure 3.3 Projected fringes, colour image and epipolar triangulation used (top), lesion and 3D prototype (middle) and topographic images of the skin and the lesion (bottom) obtained with the 3D system.

### 3.1.3. Laser self-mixing technology (Optical Feedback Interferometry, OFI)

The platform also included a laser self-mixing technology system, also known as OFI. This technique is based on the projection of a laser onto the skin, which is back-scattered by seeding particles in flows, e. g., red blood cells. Interferences between the backscattered and the laser itself are then registered, providing a 2D skin micro-capillarity blood flow image (Figure 3.4). This method is envisaged to detect abnormal vascularization network on regions of malignant lesions, especially, melanoma, which is the most aggressive form of skin cancer.



Figure 3.4 OFI system.

The OFI system used in this project consisted of a distributed feedback (DFB) laser diode at 1310 nm, packaged with a monitoring photodiode located at the back facet of the laser which enabled acquisition of the power variations induced by the interferences inside the active cavity of the laser, and a collimating lens placed in front of the laser to fit and keep the beam width along the optical path and onto the circular aluminium coated mirror of diameter 4.2 mm. The mirror used was a 2 axis beam-steering which was mounted in a Micro-Electro-Mechanical Systems (MEMS) to scan the skin across two directions. It presented an angle of  $-5^\circ$  to  $+5^\circ$  in each direction (X/Y), with a step angle of  $0.0025^\circ$ , which implies a maximum resolution of  $5\ \mu\text{m}$ . A focusing lens was placed at its focal length from the target to focus the beam (Figure 3.5) [126], [127]. The interferometric signal was recovered by monitoring of the laser output power in the internal photodiode. The system also included a base to provide the power supply, a signal acquisition card and the connections to the computer. The system allowed to scan 225 different points in a 11 mm x 12 mm skin surface to obtain a 2D image of the lesion blood flow. The information provided at each measurement point by the OFI sensor is a parameter proportional to the blood perfusion level in the skin.

Due to the fact that this thesis is focused on the development of the multispectral system, next section (3.2) describes this system in more detail.

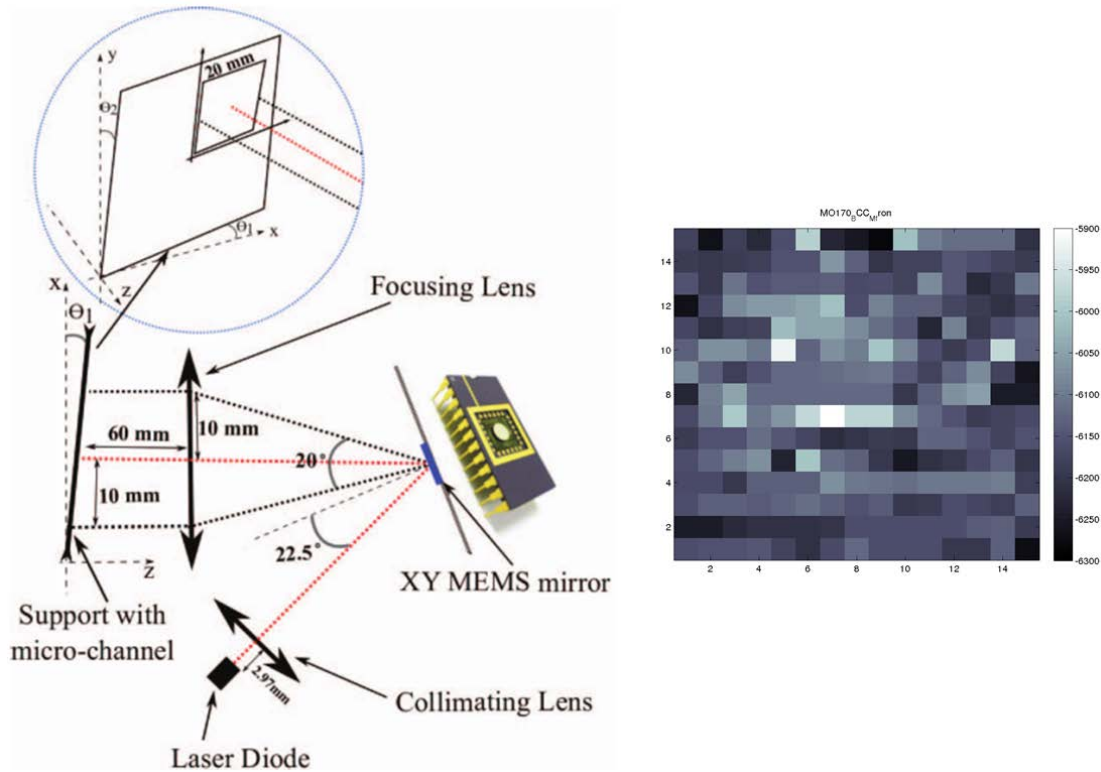


Figure 3.5 Scheme of the laser beam, where the red dot lines indicate the laser path when X and Y are at  $0^\circ$  and the black dot lines indicate the path in the extremes of the angular range of the mirror [127] (left). 2D OFI signal image proportional to the blood perfusion level (right).

#### 3.1.4. Barcelona and Modena platforms: operation, computers and metal rings for the spatial correlation

Figure 3.6 shows pictures of the two multiphotonic platforms installed in Barcelona and Modena, respectively. The confocal microscope was attached to the lower telescopic arm and the 3D system to the upper one. Although they were placed at different heights, both devices could be moved by the operator using the possibilities of extension and rotation of the arms, to reach the different parts of the patient's body in an easy and comfortable way. Given that the OFI and multispectral systems were handheld devices, they were located on the top shelf of the cart.

A total of two computers were also included in each platform with their own computer screen. The first computer controlled exclusively the confocal microscope with the VivaScan<sup>TR</sup> software application developed by Mavig GmbH that enabled the acquisition and visualization of the confocal images of a lesion. The second computer run the software applications implemented in the DIAGNOPTICS project to get the data from the 3D, the OFI and the multispectral systems. The main reason for having two different computers was that the VivaScope needed a dedicated computer to run properly, i. e., to guarantee a smooth imaging process without overloading the computer. Both computers ran under

Windows 7 64 bits Operating System and were connected with a switch which allowed the use of only one keyboard and one mouse.



Figure 3.6 Multiphotonic platforms installed in Barcelona and Modena, respectively.

The four devices of the platform were used one by one in the in-vivo examination of the patient's lesion. Therefore, there was no more than one device simultaneously measuring a particular lesion, and consequently, just the corresponding software of the active device was needed to run at the same time. For this reason, the transfer speed, the CPU performance and the RAM capacity was not a problem. Accordingly, each device was controlled independently through its program interface, as it is schematically shown in Figure 3.7.

Since the four technologies included in the platform provided images, a scheme to enable correlation of the data collected from the different devices was designed. In this context, two metal rings were built: a big one, with 41 mm and 32 mm of outer and inner diameters, respectively, enabling the acquisition of 3D, OFI and multispectral images. It was attached to the skin through a double-sided adhesive film that covered just the ring area; and a small one, with 31 mm and 27 mm of outer and inner diameters, respectively, used for the confocal microscopy. The outer diameter of this last ring almost equals the inner diameter of the big one. The adhesive ensured that the location did not change during the clinical measurements. The coincidence of the two types of ring (outer and inner diameters) and also a notch to control the tilt made it possible to spatially correlate the images obtained with all devices (Figure 3.8).

### 3. EXPERIMENTAL SYSTEM

---

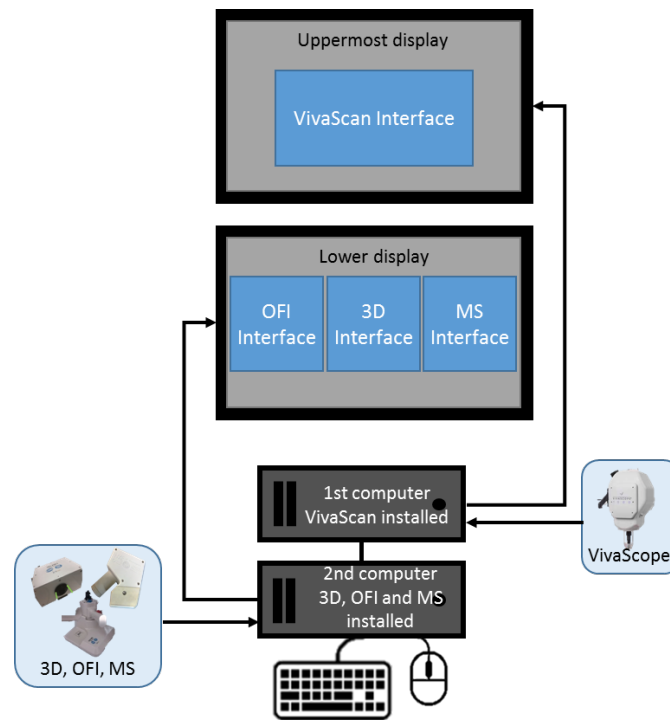


Figure 3.7 Connection scheme and computers to operate with the different devices included in the platform.



Figure 3.8 Big metal ring for the acquisition of the 3D, OFI and multispectral system (top left), small metal ring for the confocal microscopy acquisition (top right), and the big metal ring being used at the clinical setting (bottom).

The metal rings were made of rust free stainless steel - they were not allergy-inducing - and could be reused repeatedly with an appropriate disinfection after each use. The double coated adhesives were a medical tape of polyethylene with acrylate adhesive designed for medical/surgical use. It was a one-time use product, and so a new one had to be used for each examination.



### 3.2. Multispectral system

#### 3.2.1. Design and components

This thesis deals with the development of a new handheld multispectral system with spectral bands along the VIS and the NIR ranges for the diagnosis of skin cancer. The goal is to compute spectral features, e. g., the reflectance, and colour information from the lesions trying to determine if there are differences between malignant and benign ones. This is the reason why in this section the multispectral system prototype developed is presented individually in more detail.

The system was designed taking into consideration the requirements in hospitals, where the space is usually limited because of the architectural fittings [128] and where the dedication time to each patient is restricted [129]. For this reason, the system consisted of a handheld ergonomic cylindrical multispectral head of approximately 10 cm in length and 7.5 cm in diameter coupled to a conus of 5 cm length including a camera, a lens, an illumination system with two polarizers, and a separate base which permitted to hold the multispectral head between measurements making the whole procedure more comfortable for physicians and nurses (Figure 3.9).



Figure 3.9 Several views of the multispectral system with the base.

The cylinder was made of polyvinyl chloride (PVC), and had a weight of 0.5 Kg approximately. The conus had an aperture of 2.5 cm of diameter and a positioning notch which perfectly fitted together with the metal ring designed for the correlation of data of different technologies (see section 3.1.4) (Figure 3.10) (Appx. A.1).

The camera used in the multispectral head was a DMK 23U445 (Appx. A.2) with a 1/3" CCD sensor of Sony ICX445ALA with 1280x960 pixels of resolution and 12-bit depth (Appx. A.3). The lens coupled was a Schneider-Kreuznack Cinegon (Appx. A.4) with spectral sensitivity from 400 nm to 1000 nm and a working distance from infinite to 20 mm, which allowed focusing the skin lesions at a distance of 4 cm with a field of view of 15 mm x 20 mm. This field was selected taking into account that most of the skin lesions

### 3. EXPERIMENTAL SYSTEM

---

are smaller than 20 mm in diameter [130]. The f-number used for the lens was  $f/5.6$  which ensured a good compromise between depth of focus and chromatic aberration along the spectral bands of the system.



Figure 3.10 Overview of the multispectral head including the cylinder and the conus.

Our approach to obtain spectral images of the lesion was to use sequential multiplexed illumination. In order to fulfil the requirements of reduced space and easy control, a ring composed of several LEDs with narrow spectral emission over the VIS and NIR ranges was considered as the best option. Specifically, Surface Mounted Devices (SMD) were used. These kinds of LEDs are prepared to be mounted directly on printed circuit boards (PCB) and, therefore, their dimensions are smaller than conventional ones. Furthermore, to reduce the exposure time required for the image acquisition and to obtain a uniform illumination, the use of high power LEDs with a broad spatial emission was also necessary.

The criteria for selecting the different LEDs wavelengths was to be able to obtain information of the absorption curves of the principal chromophores of the skin, especially taking into account their most representative minima and maxima and the spectral bands with considerable differences among them. Despite of this, the commercial availability was also a limiting factor. Table 3.1 contains the peak wavelengths ( $\lambda_p$ ), the spatial emission, i. e., the angle of emission  $\phi(^{\circ})$ , the dimension of the LEDs and the relationship between the peak of the LEDs chosen and the reason of selection, taking into account the chromophores' absorption features.

Figure 3.11 shows the normalised spectral emission of the 8 LEDs purchased and Table 3.2 contains the corresponding peak wavelengths ( $\lambda_p$ ) and the full width at half maximum (FWHM). These values were measured with the spectrometer SPECTRO 320 and the optical probe EOP-146 from Instrument Systems GmbH (Appx. B.1 and B.1.1, respectively). The differences found between the measured values and those provided by the manufacturer were always below 25 nm in terms of  $\lambda_p$ .

Four units of each wavelength (clusters) distributed over the ring, each of them with an angular separation of  $90^{\circ}$ , were used to achieve a good illumination uniformity over the lesion. Therefore, 32 LEDs (8 clusters) were finally mounted on the ring (Figure 3.12 top). The board and the electronic board for their precise control can be found in Appendix. A.5 and A.6, respectively.

Table 3.1 Peak wavelength ( $\lambda_p$ ), spatial emission (angle in degrees), and dimension of the LEDs given by the manufacturer, and the reason of selection of the wavelength.

Manufacturer reference	$\lambda_p$ (nm)	Viewing angle ( $\phi$ [°])	Dimensions of the LED (mm)	Reason of selection
RLCU-440-410	410-415	120	3.8 x 3.8 x 0.9	Hb* and HbO <sub>2</sub> ** peaks of maximum absorption.
LXML-PR01-0500	440-460	125	4.9 x 3.2 x 2.1	Melanin maximum absorption
LXML-PB01-0040	460-485	125	4.9 x 3.2 x 2.1	Bilirubin peak of maximum absorption.
LXML-PM01-0100	520-540	125	4.9 x 3.2 x 2.1	Hb* minimum absorption
LXM3-PD01-0350	650-670	125	4.9 x 3.2 x 2.1	Intermediate wavelength allowing a complete spectral sampling.
RLCU-440-720	720	120	3.8 x 3.8 x 0.9	HbO <sub>2</sub> ** minimum absorption
RLCU-440-880	880	120	3.8 x 3.8 x 0.9	Typical wavelength used in pulse oximetry (allowing differentiation between Hb* and HbO <sub>2</sub> **).
RLCU-440-970	970	120	3.8 x 3.8 x 0.9	Typical wavelength used in pulse oximetry (allowing differentiation between Hb* and HbO <sub>2</sub> **).
				Information from deeper layers of the skin.
				Information from deeper layers of the skin.

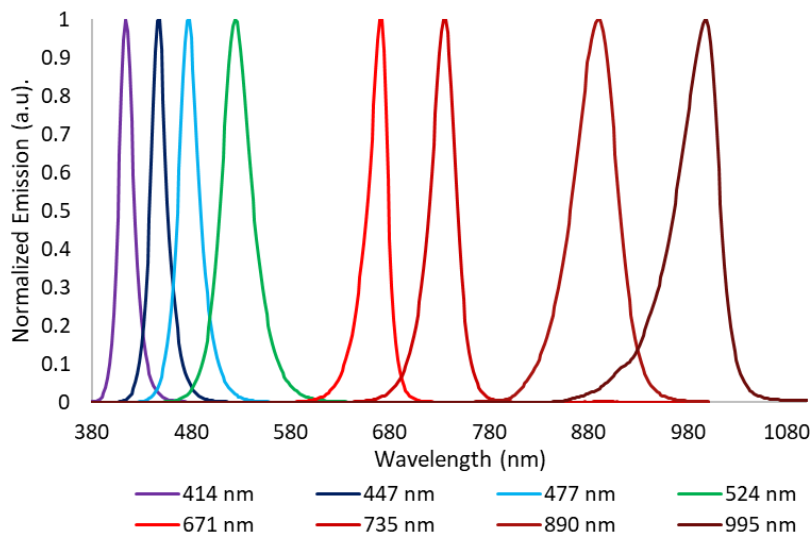


Figure 3.11 Normalised spectral emission of the purchased VIS and NIR LEDs.

### 3. EXPERIMENTAL SYSTEM

---

Table 3.2 Measured peak wavelength ( $\lambda_p$ ) and FWHM of the purchased VIS and NIR LEDs.

Manufacturer reference	$\lambda_p$ (nm)	FWHM (nm)
RLCU-440-410	414	17.2
LXML-PR01-0500	447	18.2
LXML-PB01-0040	477	23.4
LXML-PM01-0100	524	34.5
LXM3-PD01-0350	671	22.1
RLCU-440-720	735	28.9
RLCU-440-880	890	49.9
RLCU-440-970	995	44.6

The ring was placed in front of the objective lens to avoid the light of LEDs reaching directly the camera. The inside of the front conus was wrinkled and black preventing the light coming from the illumination system and reflected back by the conus reaching the sensor (Figure 3.12 bottom).



Figure 3.12 PCB with the LED ring and view of the LED ring mounted inside the cylinder (top) and view of the inside of the front conus (bottom).

In addition, the system contained two rotating polarizers located in front of the LEDs and the lens, respectively, which allowed the removal of the specular reflection from the skin, if desired (Figure 3.13 top). The first polarizer was attached to the conus with some screws in order to avoid any rotation. On the other hand, the second polarizer was attached to a cylinder with a lever which could be rotated to acquire the spectral images at 3

different degrees of polarization:  $90^\circ$  (when the polarizers are crossed),  $45^\circ$  and  $0^\circ$  (when the polarizers are parallel) (Figure 3.13 bottom).



Figure 3.13 Distribution of the multispectral head components (top): (1) camera, (2) objective lens, (3) LED ring, (4) polarizers; Polarizer attached to the conus (bottom left) and top view of the multispectral head with the lever allowing the degree of polarization to be changed (bottom right).

When the polarizers are crossed ( $90^\circ$ ), the specular reflection of the skin is removed as only light which is backscattered from deeper layers with changed polarization is allowed to pass; on the contrary, when the polarizers are parallel ( $0^\circ$ ), the information obtained comes mostly from the first surface of the skin where the specular reflection takes place. It must be noted that specular reflection does not change the polarization of light (Figure 3.14). This effect is more obvious at shorter wavelengths as they are usually strongly reflected by the skin. On the contrary, NIR wavelengths penetrate deeper into the tissue and therefore, they suffer from more scattering.

The main criteria for choosing the polarizers was to find one with a good performance along the whole spectral range of the camera (400 nm to 1000 nm). Nevertheless, because no polarizer with a so broad range could be found in the market, a laminated film with a 38% of transmission for unpolarised light from 400 nm to 700 nm was finally selected. Moreover, this flexible material helped in the final system assembly (Appx. A7).

Another issue requiring special attention was the inclusion of a trigger in the handle of the multispectral head, which made the measurement acquisition easier. In a preliminary design only a button in the keyboard of the PC was available and, consequently, an

### 3. EXPERIMENTAL SYSTEM

---

accidental movement from the physician could cause undesired translations of the multispectral head meaning that the spectral images of a lesion would be acquired at slightly different positions (therefore losing correlation between them).

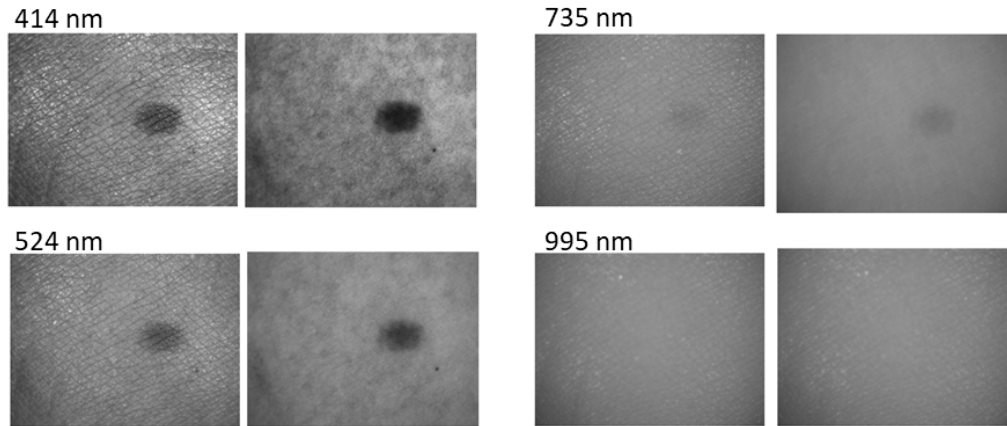


Figure 3.14 Spectral images taken at different wavelengths (414 nm, 524 nm, 735 nm and 995 nm) with the polarizers parallel (left) and crossed (right). The removal of the specular reflection can be clearly seen, mainly at shorter wavelengths. The longer wavelengths do not show this effect so clearly as they penetrate deeper into the tissue.

As formerly stated, a base was also designed and included in the system. It was manufactured by the CD6 and INEO Prototipos S.L., with the selective laser sintering (SLS) technique and Nylon 12 material. The base was used to make the measuring procedure more comfortable as the multispectral head was placed there between measurements. It has also a storing function of the power supply, the electronic boards and other parts of the system which are outside of the head. Moreover, it also incorporated a standard calibrated sample from the X Rite ColorChecker® Classic CCCR chart (Neutral 6.5) (Appx. A.8), which could be sheltered from external agents like dust by locating a tab in the “IN” and “OUT” positions, thus avoiding any possible change of its reflectance characteristics (Figure 3.15).



Figure 3.15 standard calibrated sample in the “IN” and “OUT” positions (left); and design of the interior of the base where the power supply, electronic boards, standard calibrated sample and other parts of the system are located (right).

This sample had a rather uniform spectral reflectance along the VIS and NIR ranges and was needed for the calibration of the system which was done daily before starting any measurement (see section 3.2.3.1) (Figure 3.16). For further information on the base the reader may refer to Appx. A.8.

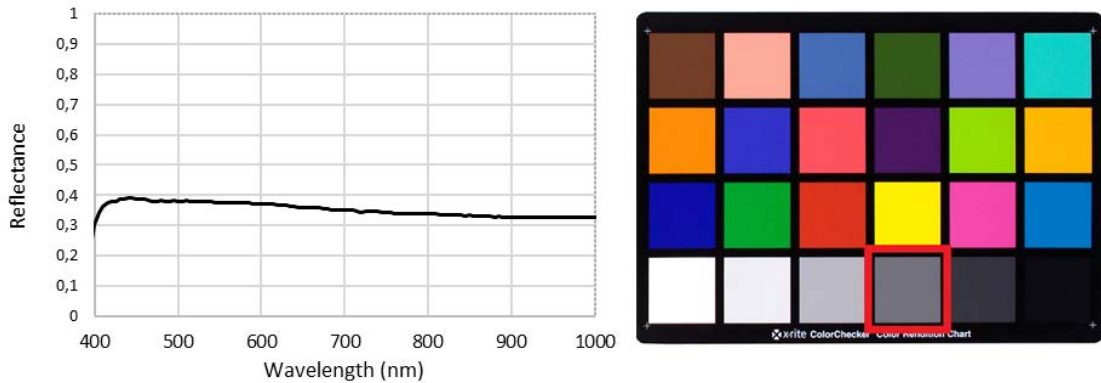


Figure 3.16 Reflectance of the “Neutral 6.5” from the X Rite ColorChecker® Classic CCR chart measured with the spectrometer SPECTRO 320 attached to the integrating sphere ISP80 from Instrument Systems, GmbH (Appx. B.1 and B.1.2, respectively) [131].

### 3.2.2. Acquisition software

An acquisition software to control all the components included in the multispectral system was developed. First an extended version to work at the laboratory level, including internal operating procedures needed to perform the whole spectral acquisition and the calibration of the system, was built. Secondly, a simplified user version for its use in the hospitals was also developed. This task was done with the support of a technician of the CD6 and using the Borland Builder C++ programming software.

#### 3.2.2.1. Extended software

Regarding the extended version of the software, it included internal operating procedures needed to perform the whole spectral acquisition of any lesion as well as calibrations to ensure the good operation of the system and the good quality of the images taken.

Both the LED board and the camera were firstly programmed allowing to control for the emission of each LED cluster individually and the acquisition of the images, respectively. The next step was to synchronize them in order to acquire sequentially the spectral images at all wavelengths for the 3 degrees of polarization.

To prevent overheating of the LEDs as a consequence of their close arrangement, which could cause a change in their emission, the sequential acquisition process of switching them on and off and acquiring the corresponding images was programmed avoiding the consecutive use of adjacent LEDs. The order was the following: 414 nm, 447 nm, 731 nm, 477 nm, 890 nm, 524 nm, 995 nm and 671 nm.

### 3. EXPERIMENTAL SYSTEM

---

As explained in the State of the art (Section 2.4), to calculate the reflectance it is completely necessary to acquire the reflectance image of a uniform calibrated reference (flat field correction) and the dark current image with the same camera settings as the sample measured, i. e., exposure time and gain.

The uniform calibrated reference used for this purpose was the “Neutral 6.5” from the X Rite ColorChecker® Classic CCCR chart with known and almost constant spectral reflectance in the wavelength range used as previously described. This sample was included in the base of the multispectral system (see Figure 3.16) and was measured every day before any skin measurement to guarantee a good daily computation of the reflectance at all wavelengths along all LEDs lifecycle. This measurement procedure was called “daily calibration”.

On the other hand, in order to properly remove the dark current noise, due to straylight (e. g., from internal backreflections of the LEDs from the conus) or non-uniformities of the pixels of the camera sensor, an image was also taken in a dark room avoiding any object in front of the multispectral system. This measurement, called as “dark calibration”, was done only once in the laboratory because of the technical difficulties of doing it in the hospital as it requires a dark environment and no objects close to the system.

However, another key aspect for the acquisition along all wavelengths was to adapt the exposure time of the camera to be able to acquire an image of any lesion and its surrounding skin within the dynamic range and thus, avoiding saturated or noisy areas with digital values similar to those of the dark calibration. In fact, not all skin cancer lesions are necessarily pigmented [132], [133] and also very different reflectance values can be present inside the image of a unique lesion; therefore, a high variation can be registered in terms of digital levels within a single image, mainly if the surrounding skin of Caucasian individuals is considered.

According to all this, an iterative algorithm to adapt the exposure time for each measured lesion was developed. It worked as follows: the exposure time chosen was that for which the average of the image acquired at each wavelength for a skin lesion was about half of the dynamic range of the camera. After performing several measurements of common moles of different sizes and from people with different skin pigmentation, the selected averaged value was of  $1800 \pm 200$  digital levels. This value allowed not having many saturated images when specular reflection was not removed by means of the polarizers (i. e., they were parallel), while keeping good image quality when the polarizers were crossed.

Nonetheless, the next issue to be considered was that the calibrated uniform sample “Neutral 6.5” had to be measured with the same exposure times in order to calculate the reflectance of the lesion at each wavelength. The problem of doing so was the time needed for all the acquisitions, which was unacceptable for the clinical practice due to the fact that after each lesion measurement the calibration was required lasting about 5 minutes.

In order to solve this, the adapting algorithm was limited to 10 specific exposure times for each wavelength and degree of polarization, and only those were included in the daily calibration. These fixed exposure times were firstly calculated looking for the exposure time



needed to obtain an average image of the calibrated sample “Neutral 6.5” from 900 to 3600 digital levels, with steps of 300, with a maximum error of  $\pm 200$  for each wavelength and polarization positions. And only one of them was later used to acquire the image of a particular skin lesion.

In accordance, the daily calibration was finally defined as the spectral image acquisition using the 10 exposure times shown in Table 3.3 for the calibrated sample “Neutral 6.5”, which had to be done only once every day before any lesion acquisition. Similarly, the dark calibration was limited to the 10 exposure times selected. Both procedures took around 5 minutes to be done. It is worth noting that the exposure times for the IR wavelengths were almost the same for the 3 different polarization levels, due to the fact that polarizers were not working properly above 700 nm.

This adaptive algorithm allowed dark or light, big or small lesions from individuals with ivory to very dark brown skins to be measured.

The operating protocol to acquire any particular skin lesion using the adaptive algorithm was then programmed as follows: firstly, the polarizers were crossed ( $90^\circ$ ). Secondly, the software searched for the optimal exposure time needed to obtain a digital level of  $1800 \pm 200$  for each wavelength. Thirdly, the exposure time found was compared with the 10 fixed ones available in Table 3.3. The exposure time chosen for each wavelength to perform the final measurement of the skin lesion was the closest one to the optimal exposure time previously found. The sequence was then repeated for the polarizers at  $45^\circ$  and when they were parallel ( $0^\circ$ ) using the corresponding exposure times shown in Table 3.5. By using this process, a measurement of one single skin lesion took around 40 seconds.

A Guide User Interface (GUI) was created to allow both calibrations (daily and dark) as well as measurements of the skin lesions. Figure 3.17 shows the main screen of the extended version of the software, which was divided in two different areas: the turquoise box on the left, which was used for testing in the laboratory (not available for physicians), and the grey box on the right, corresponding to the user interface to conduct the clinical measurements at the clinical site.

The commands inside the turquoise box allowed the good operation of the multispectral system and the software to be tested as well as the dark calibration to be done. Starting from the top, in the white box the real-time commands sent and received from the system are shown. The “Delay” box was used to include a time delay between switching a LED on and capturing the corresponding image. The final delay used was 2 seconds to ensure a constant emission of the LEDs minimizing registered variations among acquisitions (see section 3.2.3.1 for further information on this). When the “SEARCH Texp” checkbox was checked, the software looked for the specific exposure times shown in Table 3.3 after pressing the “CALIBRATION” button available below.

The “DARK CALIBRATION” button allowed the dark calibration to be performed. The dark calibration images were stored in “.raw” format in an specific folder for only dark calibrations, and finally, the last button at the bottom (“Apaga Leds”) was used to switch off all LEDs to avoid them remain switched on erroneously.

### 3. EXPERIMENTAL SYSTEM

---

The commands inside the grey box are explained in the next section as they were part of the user interface.

Table 3.3 Exposure times (in milliseconds) needed to obtain the averaged digital levels (DL) from 900 to 3600 ( $\pm 200$ ) in steps of 300 for the 3 degrees of polarization and the uniform calibrated sample “Neutral 6.5”.

Polarizers	Averaged	414	447	477	524	671	735	890	995
	DL	nm	nm	nm	nm	nm	nm	nm	nm
<b>90° (crossed)</b>	900	346	36	37	58	73	214	113	516
	1200	466	48	50	78	98	288	153	700
	1500	587	61	63	99	123	364	193	885
	1800	713	73	76	119	149	440	233	1070
	2100	836	87	91	139	174	516	274	1260
	2400	984	98	102	160	200	593	315	1492
	2700	1112	111	115	184	225	671	364	1675
	3000	1237	123	128	201	251	748	406	1874
	3300	1365	136	141	225	276	826	448	2112
3600	1498	150	154	242	302	903	490	2425	
<b>45°</b>	900	287	28	30	47	58	171	15	541
	1200	386	38	40	63	77	231	155	727
	1500	485	48	50	79	97	291	195	913
	1800	585	58	61	96	118	350	235	1131
	2100	688	68	71	112	137	410	275	1292
	2400	789	78	83	129	158	470	323	1521
	2700	907	89	92	145	178	530	364	1706
	3000	1010	99	104	162	198	602	407	1902
	3300	1115	109	113	178	218	654	448	2139
3600	1215	119	124	195	239	724	490	2455	
<b>0° (parallel)</b>	900	255	25	26	42	50	148	115	546
	1200	343	34	35	56	68	200	155	732
	1500	430	42	46	71	86	251	195	919
	1800	518	52	54	86	104	303	235	1136
	2100	622	60	65	101	121	354	274	1295
	2400	715	69	74	118	139	414	315	1520
	2700	806	79	82	133	157	468	363	1704
	3000	895	88	91	145	175	521	404	1934
	3300	987	96	102	162	193	573	445	2143
3600	1077	105	110	175	210	626	487	2443	

---

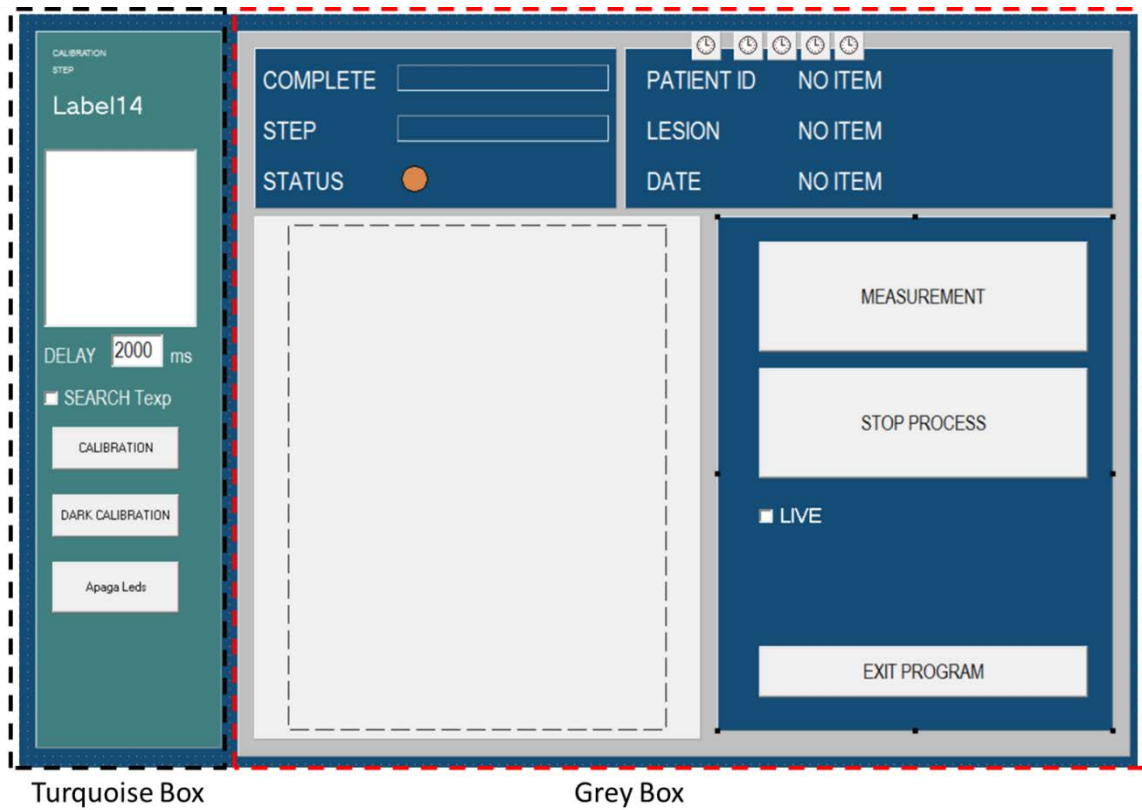


Figure 3.17 Screenshot of the extended software. The turquoise box used for testing is shown on the left while the grey box available for physicians is on the right side.

### 3.2.2.2. User interface

A simplified version of the software was delivered to physicians with only the grey box of the extended version available. In this version, physicians could only interact with the following buttons: “MEASUREMENT” to proceed with a lesion acquisition (or the daily calibration if it was the first measurement of the day), “STOP PROCESS” to stop a measurement or the calibration at any moment, and “EXIT PROGRAM” to exit the software. Furthermore, the checkbox “LIVE” was added to see in real time the camera’s video signal to make the placement of the multispectral system on the lesion easier.

Each time that the “MEASUREMENT” button was pressed, the software checked if the daily calibration of that day was done before or not. If not, a pop-up screen with the message “DEVICE MUST BE CALIBRATED” appeared (Figure 3.18) and the daily calibration was carried out. At the end of this calibration, the spectral images obtained were stored in “.raw” format in a specific folder for the daily calibrations.

After the daily calibration, the “PATIENT SELECTION” screen appeared (Figure 3.19). Pressing the “NEW” button, it was possible to insert the patient identification (PATIENT ID), which was an internal numerical code used in the hospitals for this project to preserve the patient’s information, and the approximate location of the LESION on the patient’s body (e. g., arm). The date was taken automatically from the Windows® OS. Then, the software checked if this information already existed. If not, a new window to

### 3. EXPERIMENTAL SYSTEM

---

confirm the information entered was shown; otherwise, a warning message to overwrite the data appeared. The spectral images were stored in “.raw” format in the computer hard disk in a specific folder for the lesions measured.

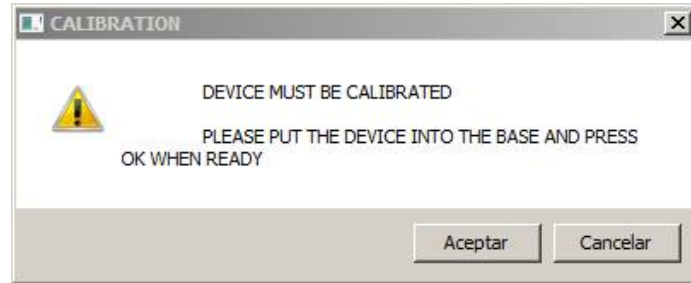


Figure 3.18 Pop-up message that appeared if the calibration was not already done.

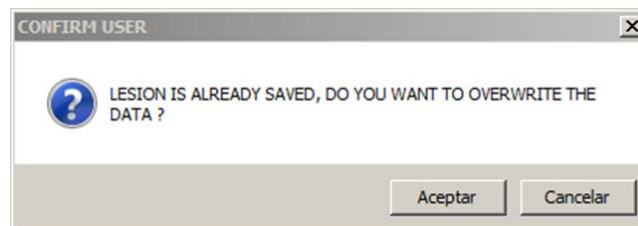
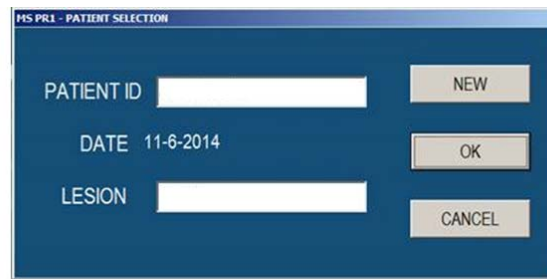


Figure 3.19 “PATIENT SELECTION” screen (top), confirmation screen (centre) and pop-up warning message (bottom).

Several pop-up windows were also enable to remind physicians to perform some actions during the whole process: when the calibrated sample was needed in the “IN” or “OUT” positions of the base for the daily calibration, and when the polarizers needed to be crossed (90°), at 45° or parallel (0°) for the daily calibration and for a lesion measurement.

Finally, it is also worth noting that the software included several automatic verifications to ensure its correct operation, and also a security function to ensure that the LEDs could

only be switched on when a measurement was being performed. Further information of the software can be found in the user manual of the system in Appx. C.

### 3.2.3. Validation of the system's performance

Once the multispectral system was built several tests were carried out to ensure its correct operation. They are described next. For the sake of simplicity only the results of the Barcelona system are reported here as very similar performances were found for both systems (Barcelona and Modena).

#### 3.2.3.1. Temporal behaviour of the LEDs emission

The changes over time of the emission of the LEDs were analysed by measuring the radiance corresponding to each wavelength at different forward currents. This was achieved by using an International Light Radiometer (IL 1700) with the input optics R #415 and the filter F #16702 (Appx. B.2). As an example, Figure 3.20 shows the radiance over time of the LEDs emitting at 414 nm at different current values (100, 250 and 500 mA). As it can be observed, the stability of LEDs improves when the current applied is lower. Furthermore, it is also shown that LEDs need at least 2 seconds to stabilize their emission.

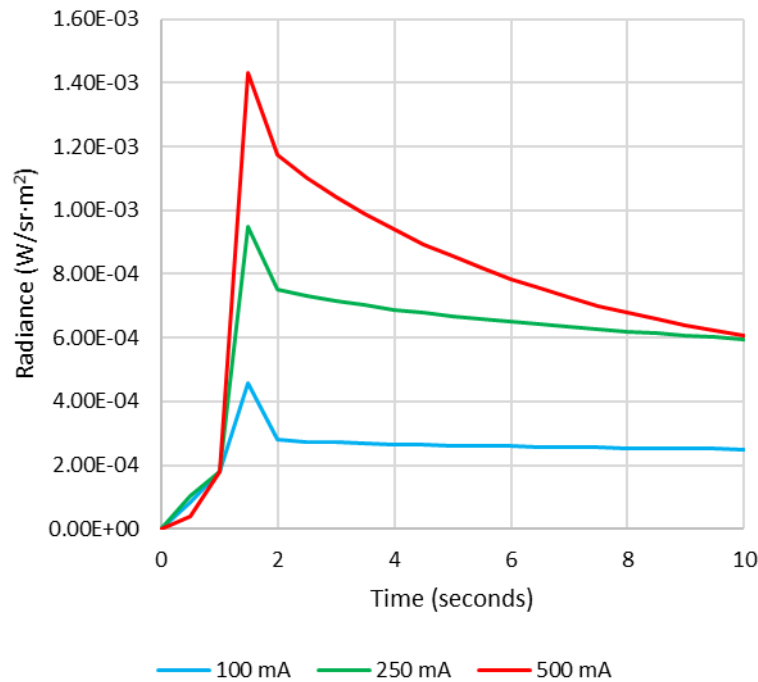


Figure 3.20 Radiance ( $\text{W}/\text{sr}\cdot\text{m}^2$ ) of the 414 nm LEDs at different forward currents measured every second over 10 seconds.

The same behaviour was observed for the rest of wavelengths (LEDs). Accordingly, Table 3.4 shows the final currents used for each wavelength, which were selected taking into account the compromise between the LEDs stability and also the exposure time needed to make use of the whole dynamic range (0-4095) of the camera for each wavelength.

### 3. EXPERIMENTAL SYSTEM

Table 3.4 Forward current used for each wavelength (expressed in mA).

414 nm	447 nm	477 nm	524 nm	671 nm	735 nm	890 nm	995
100	200	200	200	200	200	200	150

Furthermore, a delay was also implemented each time any LED was switched on to avoid measuring in the peak of emission. A 2-seconds time delay was found to be suitable for all wavelengths.

#### 3.2.3.2. Linearity, uniformity and repeatability of the system

Three additional characteristics were also measured to ensure the good performance of the multispectral system as a whole: the linear response of the camera for each wavelength, the uniformity of the LEDs emission and the repeatability of the system acquiring images.

In order to test the linearity of the camera response, spectral images of the uniform sample “Neutral 6.5” from the X Rite ColorChecker® Classic CCR chart were taken at different exposure times and their averaged digital levels were computed for all wavelengths.

As it is shown in Figure 3.21, the response of the camera can be considered almost linear at all wavelengths as only small differences between the fitting and the response were reported. The small mismatches might be probably caused due to small instabilities of the LEDs emission rather than the camera response itself. Additionally, it is worth noting the lower sensitivity of the camera sensor at 414 nm and at NIR wavelengths, especially 995 nm, which implies the use of longer exposure times.

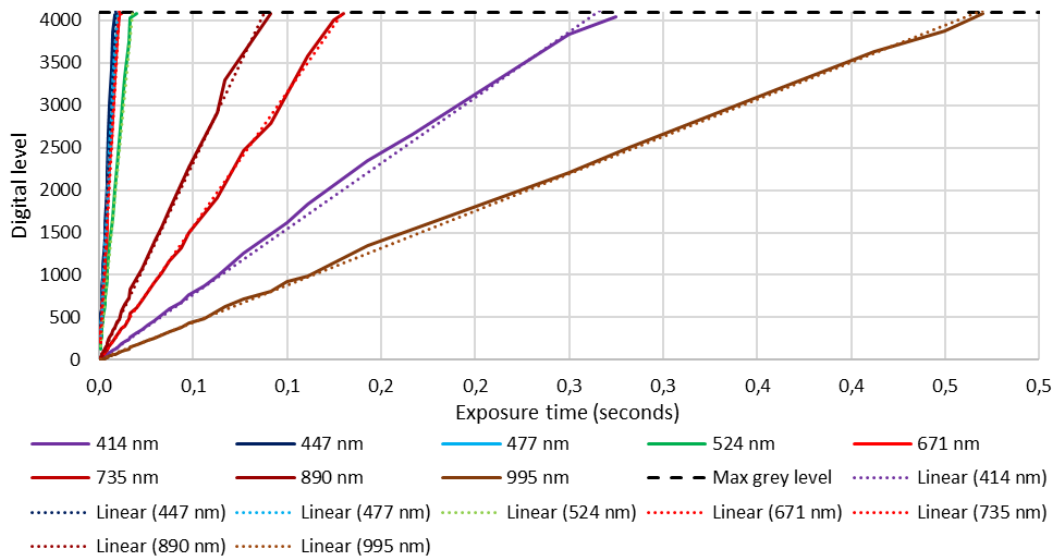


Figure 3.21 Digital levels vs. exposure time at different wavelengths to test for the linearity of the camera response.

Regarding the uniformity of the LEDs emission, the same images corresponding the uniform sample (“Neutral 6.5”) were characterized quantitatively by means of the

statistical descriptor SNUP (Spatial Non-Uniformity Percentage) [43], which is defined as follows:

$$SNUP = 100 \times \frac{\sigma(\tilde{x}_{DL})}{\tilde{x}_{DL}}, \quad (3.1)$$

where  $\tilde{x}_{DL}$  stands for the mean digital level of all the pixels in the image and  $\sigma(\tilde{x}_{DL})$  is the standard deviation. The exposure time used was the one needed to obtain images with a mean digital level of  $1800 \pm 200$  (in the middle of the dynamic range approximately).

Figure 3.22 shows the images acquired for each wavelength with their corresponding SNUP values. In all cases, the SNUP values were between 2.5% and 3.5%, so a good uniformity was achieved by means of the 4 LED units scheme used in the prototype.

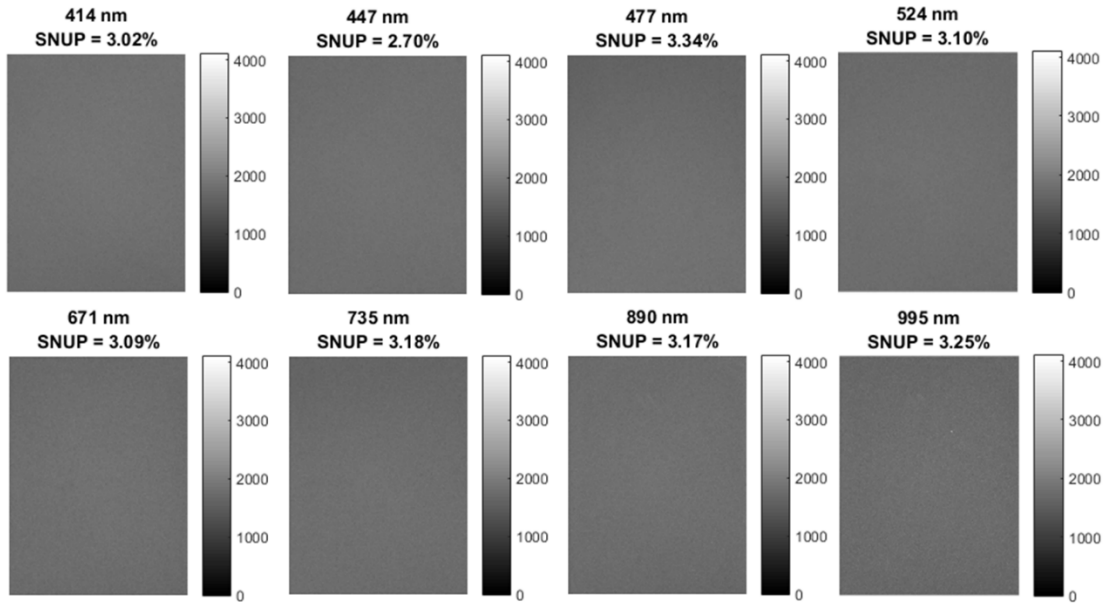


Figure 3.22 Spectral images of the uniform sample “Neutral 6.5” from the X Rite ColorChecker® Classic CCCR chart and their corresponding SNUP values.

Finally, the repeatability of the system was tested by comparing the averaged values of 9 images for each wavelength taken along 9 different days (mid-term repeatability) as well as 9 measurements taken consecutively (short-term repeatability) [134]. All images were captured with the same exposure time in order to obtain a mean digital level of  $1800 \pm 200$  approximately. The uniform sample used was again the “Neutral 6.5” from the X Rite ColorChecker® Classic CCCR chart.

Figure 3.23 depicts the averaged digital levels obtained for the 9 acquisitions along the 9 different consecutive days; Table 3.5 shows the percentage of variation in terms of digital levels calculated similarly to the SNUP formerly used to account for the uniformity, but considering the readings done over time instead in this case. As it can be observed, the temporal repeatability is always below 2%, so that the system can be considered to have a good mid-term repeatability.

### 3. EXPERIMENTAL SYSTEM

---

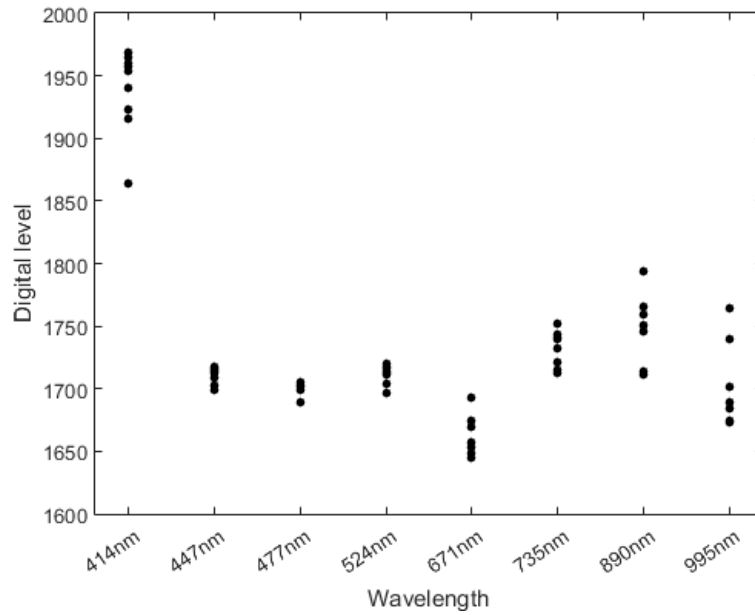


Figure 3.23 Mean digital levels of the 9 spectral images obtained along 9 different days for each wavelength.

Table 3.5 Percentage of variation in terms of digital levels of the 9 images acquired in 9 different days for each wavelength.

414 nm	447 nm	477 nm	524 nm	671 nm	735 nm	890 nm	995
1.70%	0.37%	0.27%	0.42%	1.00%	0.84%	1.60%	1.87%

Similarly, the short-term repeatability results are depicted in Figure 3.24 and Table 3.6. As it can be seen, the percentages were lower than 0.5% in this case.

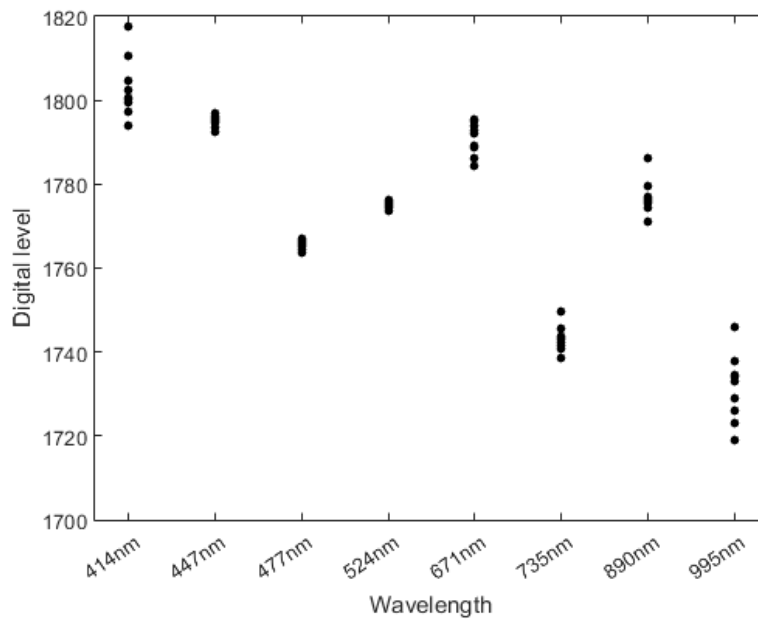


Figure 3.24 Mean digital levels of the 9 spectral images acquired consecutively for each wavelength.



Table 3.6 Percentage of variation in terms of digital levels of the 9 images acquired consecutively for each wavelength.

414 nm	447 nm	477 nm	524 nm	671 nm	735 nm	890 nm	995
0.40%	0.08%	0.06%	0.05%	0.22%	0.18%	0.23%	0.47%

Due to the good results achieved in terms of repeatability, images were acquired only once and no averaging was performed in the final measurements.

### 3.2.4. Safety issues

In order to proceed with the Ethical Committee approval and to launch the systems in both hospitals, irradiance and radiance measurements were done according to the standard UNE-EN 62471 “Photobiological safety of lamps and lamp systems”[135], to ensure that the multispectral system provided light emissions under the limits established by this regulation and to guarantee that patients could not be accidentally damaged under any circumstance.

In this standard, the limits of emission for the skin and corneal surface in terms of irradiance are defined. Moreover, the limits of emission regarding the light reaching the retina are also given in terms of radiance.

Regarding the irradiance measurements, the following quantities were calculated:

- Exposure limit of thermal risk of the skin (380-3000 nm):  $E_H$
- Exposure limit of actinic UV for the skin and the eye (200-400 nm):  $E_s$
- Exposure limit of UV-A for the eye (315-400 nm):  $E_{UVA}$
- Exposure limit for the risk of blue light of small sources on the retina (300-700 nm):  $E_s$
- Exposure limit of IR for the eye (780-3000 nm):  $E_{IR}$

The former exposure limits were calculated according to the equations provided by the standard, which includes weighting functions along the different spectral ranges to evaluate all the photobiological risks.

In order to compute these limits, the irradiance for all wavelengths included in the multispectral head were measured at the same position as the skin was located in real measurements. The exposure time used for each wavelength was defined as the sum of the highest exposure time at the 3 polarization positions, simulating the largest possible exposure time.

Measurements were taken with a commercial spectroradiometer Instrument Systems, Spectro 320 (D) Release, serial number n<sup>o</sup> 30932004 with the EOP-146 accessory (Appx. B.1 and B.1.1, respectively), which has an uncertainty smaller than 4% in terms of the irradiance according to the specifications of the instrument. Furthermore, the instrument has traceability with standards of the National Institute of Standards and Technology (NIST) and the Physikalisch-Technische Bundesanstalt (PTB). Table 3.7 contains the equations and the different emission limits in terms of irradiance which were calculated for

### 3. EXPERIMENTAL SYSTEM

the multispectral head. As it can be seen, all irradiance values obtained for all the spectral bands were much lower than the emission limits established by the regulation.

Table 3.7 Equations, irradiance limits and irradiance measured according to UNE-EN 62471.

Risk Name	Equation	Irradiance limit (W · m <sup>-2</sup> · nm <sup>-1</sup> )	Irradiance measured (W · m <sup>-2</sup> · nm <sup>-1</sup> )
<b>Thermal for skin</b>	$E_H = \sum_{380}^{3000} E_\lambda \cdot \Delta\lambda$	414 nm:	414 nm:
		5.81E+3	5.51
		447 nm:	447 nm:
	$E_{H\ max} = \frac{20000}{t_{max}^{0,75}}$	1.08E+4	34.55
		477 nm:	477 nm:
		9.37E+3	34.59
	Where:	524 nm:	524 nm:
	$E_\lambda$ = spectral irradiance [W · m <sup>-2</sup> · nm <sup>-1</sup> ]	9.16E+3	18.04
	$\Delta\lambda$ = wavelength step [nm]	671 nm:	671 nm:
	$t_{max}$ = maximum exposure time [s]	9.51E+3	29.00
		735 nm:	735 nm:
		9.00E+3	6.42
		890 nm:	890 nm:
	8.38E+3	14.31	
	995 nm:	995 nm:	
	7.54E+3	8.12	
<b>Actinic UV exposition for the skin and the eye</b>	$E_S = \sum_{200}^{450} E_\lambda \cdot S(\lambda) \cdot \Delta\lambda$	414 nm:	414 nm:
		5.77	9.42E-6
	$E_{S\ max} = \frac{30}{t_{max}}$	447 nm:	447 nm:
		13.12	2.16E-4
	Where:		
$E_\lambda$ = spectral irradiance [W · m <sup>-2</sup> · nm <sup>-1</sup> ]			
$S_{UV}(\lambda)$ = UV actinic risk weighting function			
$\Delta\lambda$ = wavelength step [nm]			
$t_{max}$ = maximum exposure time [s]			

<b>UV-A for the eye</b>	$E_{UVA} = \sum_{315}^{400} E_{\lambda} \cdot \Delta\lambda$	414 nm: 1.92E+3	414 nm: 0.28
	$E_{UVA max} = \frac{10000}{t_{max}}$	447 nm: 4.38E+3	447 nm: 0.25
Where:			
$E_{\lambda}$ =Spectral Irradiance [W · m <sup>-2</sup> · nm <sup>-1</sup> ]			
$\Delta\lambda$ = wavelength step [nm]			
$t_{max}$ = maximum exposure time [s]			
<b>Blue Light of small Sources</b>	$E_B = \sum_{300}^{700} E_{\lambda} \cdot B(\lambda) \cdot \Delta\lambda$	414 nm: 19.21	414 nm: 3.50
	$E_B max = \frac{100}{t_{max}}$	447 nm: 43.82	447 nm: 15.99
Where:			
$E_{\lambda}$ = spectral irradiance [W · m <sup>-2</sup> · nm <sup>-1</sup> ]		477 nm: 36.44	477 nm: 15.99
$B(\lambda)$ = blue light risk weighting function		524 nm: 35.16	524 nm: 0.81
$\Delta\lambda$ = wavelength step [nm]		671 nm: 37.18	671 nm: 0.08
$t_{max}$ = maximum exposure time [s]		735 nm: 34.52	735 nm: 0.03
		890 nm: 31.44	890 nm: 0.03
		995 nm: 27.25	995 nm: 0.03
<b>Infrared for the eye</b>	$E_{IR} = \sum_{780}^{3000} E_{\lambda} \cdot \Delta\lambda$	414 nm: 5.23E+3	414 nm: 0.12
	$E_{IR max} = \frac{18000}{t_{max}^{0.75}}$	447 nm: 9.69E+3	447 nm: 0.10
Where:			
$E_{\lambda}$ = spectral irradiance [W · m <sup>-2</sup> · nm <sup>-1</sup> ]		477 nm: 8.43E+3	477 nm: 0.13
$\Delta\lambda$ = wavelength step [nm]		524 nm: 8.25E+3	524 nm: 0.14
$t_{max}$ = maximum exposure time [s]		671 nm: 8.56E+3	671 nm: 0.16
		735 nm: 8.10E+3	735 nm: 0.18
		890 nm: 7.54E+3	890 nm: 14.01
		995 nm: 6.79E+3	995 nm: 7.84

### 3. EXPERIMENTAL SYSTEM

---

On the other hand, regarding the radiance measurements, the following quantities were also calculated:

- Retinal exposure limit for the risk of blue light (300-700 nm):  $L_B$
- Thermal retinal exposure limit (380-1400 nm):  $L_R$
- Thermal retinal exposure limit, weak visual stimulus (780-3000 nm):  $L_{IR}$

In order to compute these limits, the radiance for all wavelengths were measured by placing a radiance sensor at 50 cm of the multispectral head. The region of emission of the lamp was of 26 mm in diameter. Therefore, the angle  $\alpha$  (source size) considered in the calculations was of 0.052 rad. The exposure time used for each wavelength was defined as the sum of the highest exposure time at the 3 polarization positions, simulating the largest possible exposure time.

The measurements were taken with the commercial spectroradiometer Instrument Systems, Spectro 320 (D) Release, serial number n° 30932004 with the TOP-100 accessory (Appx. B.1 and B.1.3, respectively), which has an uncertainty smaller than 5% in terms of the radiance according to the specifications of the instrument.

Table 3.8 depicts the equations and the different emission limits in terms of radiance. As it can be seen, all radiance values obtained for all the spectral bands were several orders of magnitude lower than the emission limits established by the regulation.

Table 3.8 Equations, radiance limits and radiance measured according to UNE-EN 62471.

Risk Name	Equation	Radiance Limit ( $W \cdot m^{-2} \cdot nm^{-1}$ )	Radiance measured ( $W \cdot m^{-2} \cdot nm^{-1}$ )
Blue light for retina	$L_B = \sum_{300}^{700} L_\lambda \cdot B(\lambda) \cdot \Delta\lambda$	414 nm:	414 nm:
		1.92E+5	6.38E-4
		447 nm:	447 nm:
	$L_{B\ max} = \frac{1000000}{t_{max}}$	4.38E+5	1.27E-2
		477 nm:	477 nm:
	Where:	3.64E+5	5.82E-3
	$L_\lambda =$ spectral radiance	524 nm:	524 nm:
	[ $W \cdot m^{-2} \cdot sr^{-1}nm^{-1}$ ]	3.53E+5	3.41E-4
	$B(\lambda) =$ blue light risk	671 nm:	671 nm:
	weighting function	3.71E+5	3.91E-5
	$\Delta\lambda =$ wavelength step	735 nm:	735 nm:
	[nm]	3.45E+5	2.81E-5
	$t_{max} =$ maximum exposure	890 nm:	890 nm:
time [s]	3.14E+5	3.27E-5	
	995 nm:	995 nm:	
	2.72E+5	3.21E-5	

---

<b>Thermal for retina</b>	$L_R = \sum_{380}^{1400} L_\lambda \cdot R(\lambda) \cdot \Delta\lambda$	414 nm: 6.73E+5	414 nm: 6.90E-3	
	$L_{R\max} = \frac{50000}{\alpha \cdot t_{\max}^{0.25}}$	447 nm: 7.82E+5	447 nm: 1.27E-1	
	$\alpha = 0.052 \text{ (rad)}$	477 nm: 7.47E+5	477 nm: 5.88E-2	
	Where:	524 nm: 7.41E+5	524 nm: 8.04E-3	
	$L_\lambda$ = spectral radiance [W · m <sup>-2</sup> · sr <sup>-1</sup> nm <sup>-1</sup> ]	671 nm: 7.50E+5	671 nm: 1.30E-2	
	R( $\lambda$ ) = burn risk weighting function	735 nm: 7.37E+5	735 nm: 3.73E-3	
	$\Delta\lambda$ = wavelength step [nm]	890 nm: 7.20E+5	890 nm: 2.99E-3	
	$t_{\max}$ = maximum exposure time [s]	995 nm: 6.95E+5	995 nm: 1.87E-3	
	<b>Thermal for retina (Weak]visual stimulus)</b>	$L_{IR} = \sum_{780}^{1400} L_\lambda \cdot R(\lambda) \cdot \Delta\lambda$	414 nm: 1.15E+5	414 nm: 4.04E-4
		$L_{IR\max} = \frac{6000}{\alpha}$	447 nm: 1.15E+5	447 nm: 3.19E-4
	$\alpha = 0.052 \text{ (rad)}$	477 nm: 1.15E+5	477 nm: 1.10E-4	
Where:	524 nm: 1.15E+5	524 nm: 2.80E-5		
$L_\lambda$ = spectral radiance [W · m <sup>-2</sup> · sr <sup>-1</sup> nm <sup>-1</sup> ]	671 nm: 1.15E+5	671 nm: 7.22E-4		
R( $\lambda$ ) = burn risk weighting function	735 nm: 1.15E+5	735 nm: 8.05E-4		
$\Delta\lambda$ = wavelength step [nm]	890 nm: 1.15E+5	890 nm: 2.44E-3		
$t_{\max}$ = maximum exposure time [s]	995 nm: 1.15E+5	995 nm: 1.32E-3		



## 4. Image processing and analysis

In this chapter, the software developed for the spectral image processing and corresponding analysis is presented. Firstly, a software devoted to compute spectral and colorimetric features from the spectral images (spectral datacube) acquired with the multispectral system is described, including also the segmentation algorithm used to extract the former information of the lesion from the whole image. Another software used to operate with the spectral images to enhance any particular spectral feature potentially different in healthy and malignant tissue is also explained. In the last section, the parameters computed for each lesion measured in both hospitals are detailed.

### 4.1. From spectral to reflectance and colour images

A multispectral image system allows a spectral datacube of images to be obtained. Each image in this cube corresponds to the digital level taken in a specific spectral range, so that the extraction of spectral and colorimetric information is necessary. To achieve this purpose, a Graphical User Interface (GUI) was programmed using the Matlab® R2015a software (Figure 4.1) by the author of this thesis.

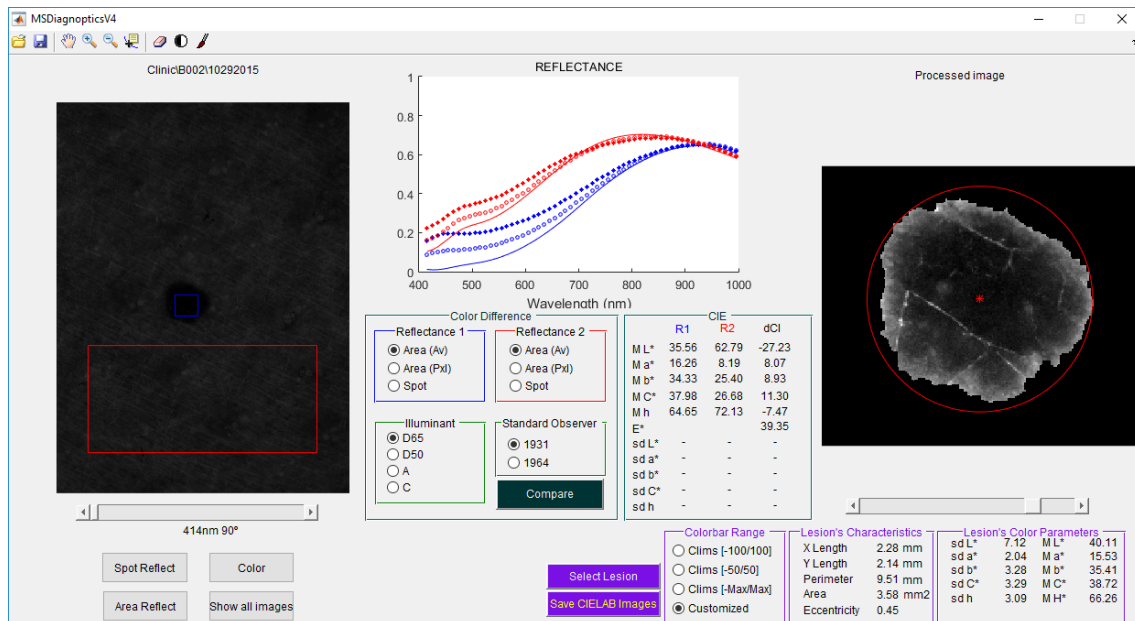


Figure 4.1 Graphical User Interface (GUI) to compute spectral and colorimetric images.

In order to calculate the reflectance images from the spectral images taken, an automatic algorithm was created. Besides the spectral images of the lesion itself, the daily and dark calibrations acquired were also needed to compute the reflectance cube.

Specifically, from the spectral images of the 8 spectral bands available in the multispectral system, 8 reflectance and 8 absorbance images were computed for a given wavelength  $\lambda_i$  (i. e., 414 nm, 447 nm, 731 nm, 477 nm, 890 nm, 524 nm, 995 nm and 671 nm) (Figure 4.2) as follows:

$$Refl_{\lambda_n}(i, j) = Refl_{ref_{\lambda_n}} \cdot \frac{DL_{\lambda_n}(i, j) - DL_{0_{\lambda_n}}(i, j)}{DL_{ref_{\lambda_n}}(i, j) - DL_{0_{\lambda_n}}(i, j)}, \quad (4.1)$$

$$Abs_{\lambda_n}(i, j) = -\log(Refl_{\lambda_n}(i, j)), \quad (4.2)$$

where  $Refl_{\lambda_n}(i, j)$  is the reflectance,  $DL_{\lambda_n}(i, j)$  is the digital level of the acquired raw image of the lesion,  $DL_{0_{\lambda_n}}(i, j)$  is the digital level of the dark calibration image,  $DL_{ref}(i, j)$  is the digital level of the calibrated sample “Neutral 6.5” available in the daily calibration,  $Refl_{ref_{\lambda_n}}$  is the calibrated reflectance of the same sample measured with the spectrometer SPECTRO 320 and  $Abs_{\lambda_n}(i, j)$  is the absorbance.

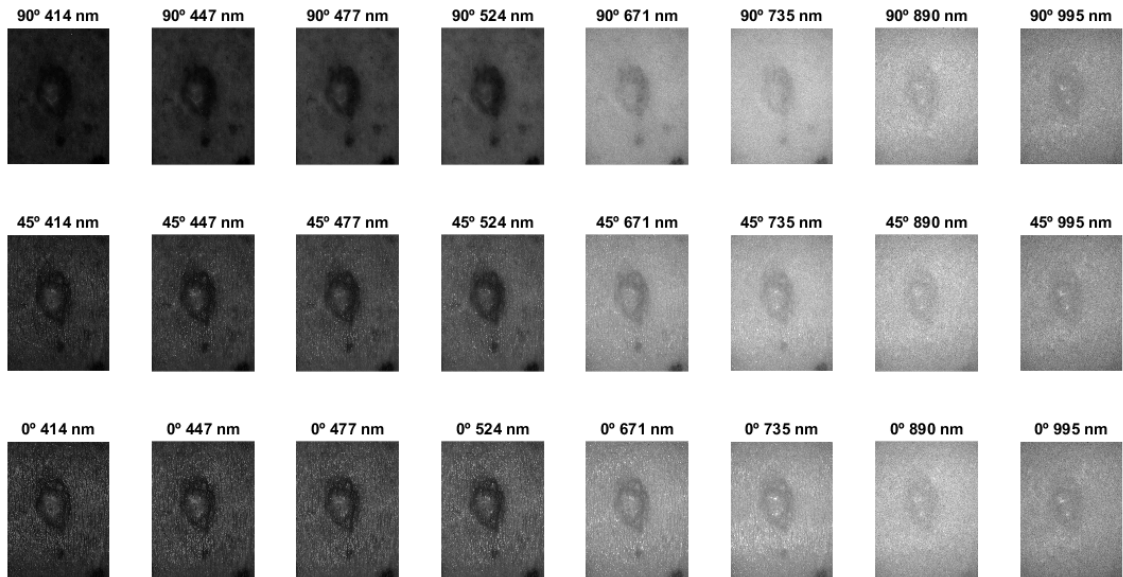


Figure 4.2 Reflectance images at different wavelengths (414 nm, 447 nm, 731 nm, 477 nm, 890 nm, 524 nm, 995 nm and 671 nm) and degrees of polarization ( $0^\circ$ ,  $45^\circ$ ,  $90^\circ$ ) for a common nevus.

The GUI also allowed computing a pseudo-coloured image from the spline interpolation of the reflectance images from 415 nm to 700 nm with steps of 10 nm (Figure 4.3 left). Furthermore, averaged reflectance curves and colour differences between two selected areas were also computed. It is worth noting that colour differences were only approximate as they were computed from partial spectral information acquired through the 8 spectral



bands of the system and the posterior interpolation rather than using precise measurements taken every 5 nm or 10 nm as recommended by the CIE. On the other hand, the selected areas could be a region of interest (ROI) of 3x3 pixels (“Spot”) or, alternatively, a squared area selected on the image (“Area”) (Figure 4.3 right).

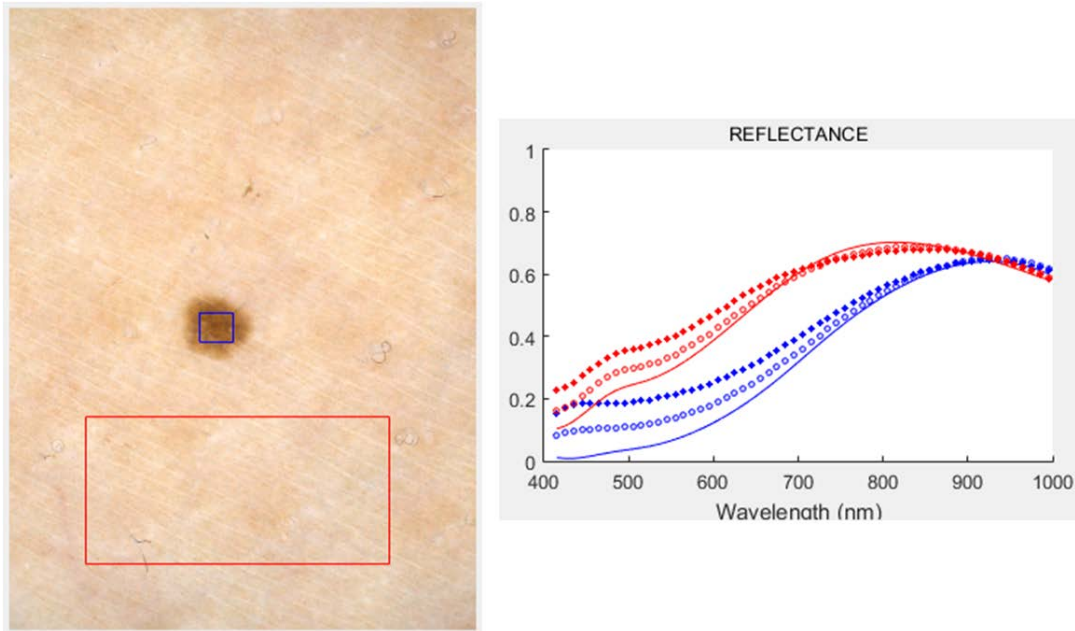


Figure 4.3 Pseudo-coloured image (left) and averaged reflectance curves from the ROIs selected (right). In the reflectance plot the solid line corresponds to the crossed polarizers ( $90^\circ$ ), the empty circles to  $45^\circ$  and the filled circles to  $0^\circ$  (parallel polarizers).

On the other hand, it allowed to compute images in terms of CIELAB colour coordinates, i. e.,  $L^*$ ,  $a^*$ ,  $b^*$ ,  $C^*_{ab}$  and  $h_{ab}$  (Figure 4.4), although they are called pseudo-CIELAB colour coordinates in this thesis because they are only approximate as described above. For the calculation of the pseudo-CIELAB values, it was possible to select the CIE standard illuminant (C, D65, and D50 as daylight simulators and A as tungsten-filament lightning) and the standard observer (1931 ( $2^\circ$ ) or 1964 ( $10^\circ$ )).

In order to check the proper operation of the software and the calculation of the reflectance, two skins from different people were measured with the multispectral system and also with the spectrometer SPECTRO 320 attached to the integrating sphere ISP80 from Instrument Systems, GmbH (Appx. B.1 and B.1.2, respectively) (Figure 4.5 top); the reflectance obtained from the multispectral system using the crossed polarizers was used for the comparison. Furthermore, these results were also converted to absorbance values as  $-\log(\text{reflectance})$  (Figure 4.5 bottom).

As it can be observed, the reflectances obtained from the multispectral head are similar to those measured by the spectrometer, although slightly larger differences are reported at wavelengths above 700 nm. This can be attributed to the fact that even if we use the crossed polarizers and quite diffuse illumination (LEDs and conus) we do not reach the levels of diffusion to resemble the geometry of the integrating sphere. One must take into

account that above this wavelength the operation of the polarizers is not optimal. On the other hand, the colour differences obtained between both systems were, in terms of  $\Delta E$  (CIELAB), of 6.4 and 5.0 for Skin1 and Skin2, respectively. Even they are not very small, they can be considered still acceptable taking into account the tolerances often used in the industry when dealing with colour differences: differences below 3 are considered to be hardly perceptible and therefore small, from 3 to 6 acceptable (normal tolerance) and above 6 noticeable (large tolerance). The colour differences obtained in this work are acceptable if one considers the smooth reflectance or absorbance profiles linked to skin samples and lesions as already reported by other authors (see Figure 2.19). In this figure, the optical density of melanomas, nevi and healthy skin samples reported by Diebele et al. are shown. It can be seen that the curves are pretty similar to the absorbance ones obtained with the multispectral system developed in this thesis (Figure 4.5 (bottom)).

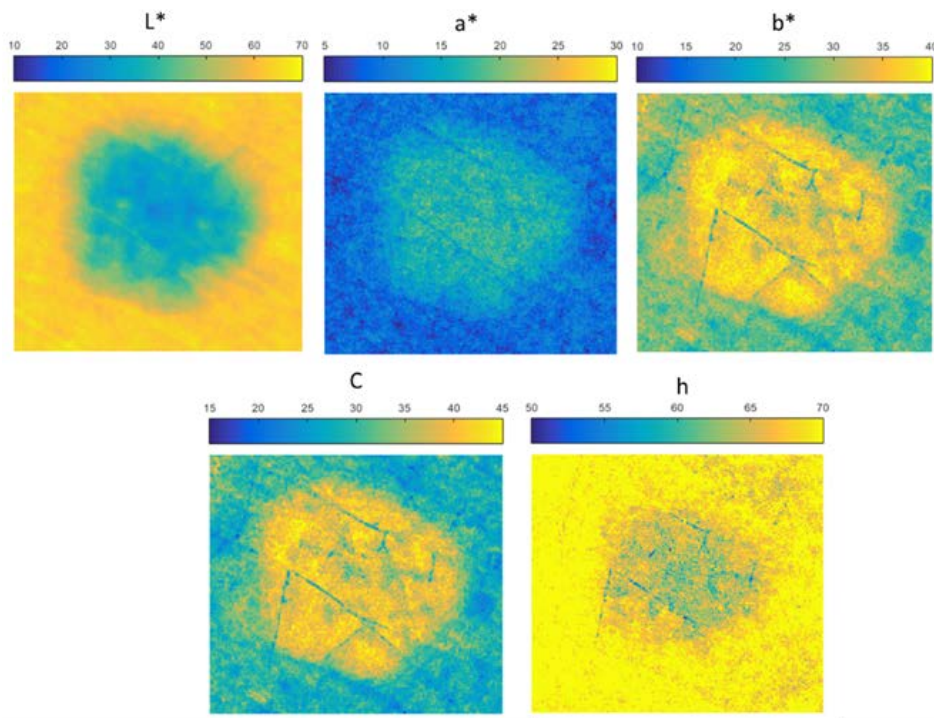


Figure 4.4 Images in terms of pseudo-CIELAB colour coordinates:  $L^*$ ,  $a^*$ ,  $b^*$ ,  $C^*_{ab}$  and  $h_{ab}$  for a common nevus.

The implemented software also allowed performing the segmentation of the lesion to analyse its spectral and colour features independently from the surrounding skin. The algorithm used consisted of searching the digital level threshold to establish which pixels belonged to the patient's lesion and which ones to the surrounding healthy skin. To do so, the reflectance image used was the bluest one (414 nm), due to the fact that melanomas are pigmented lesions and the melanin chromophore has a stronger absorbance in the blue range of the electromagnetic spectrum; thus, this image provides information from the most superficial layers of the skin and allows for a better discrimination between the lesion and the surrounding healthy skin. As it can be seen in Figure 4.6 (top), the lesion seems to be smaller at 671 nm because of the lower absorbance of the melanin at this wavelength.

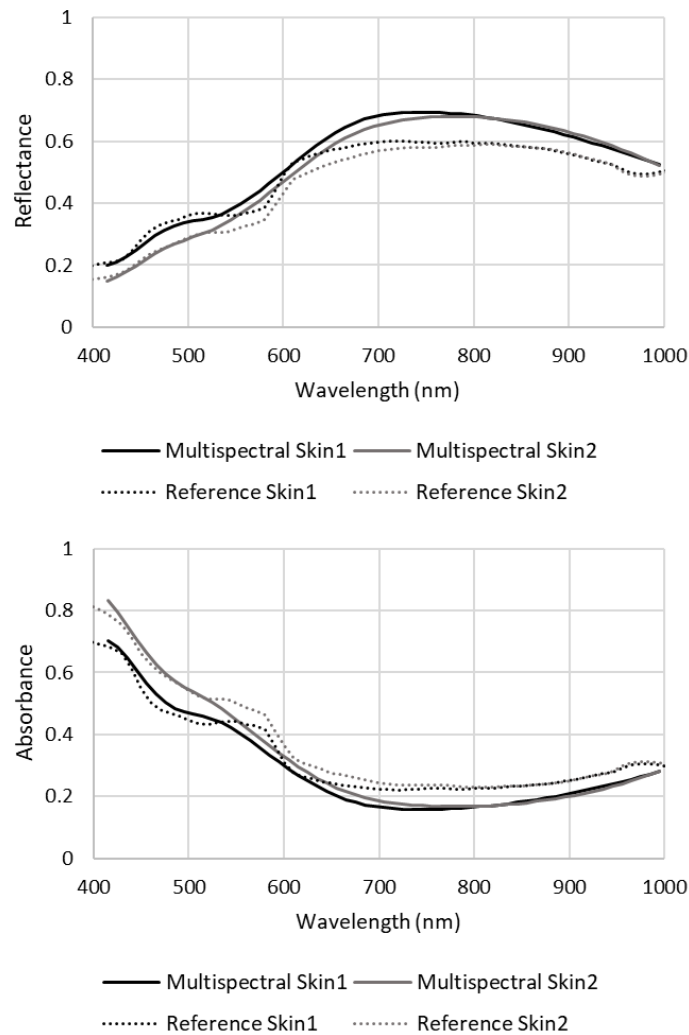


Figure 4.5 Reflectance (top) and absorbance curves (bottom) obtained for two skins from different people with the multispectral system with crossed polarizers and the spectrometer SPECTRO 320.

The digital level threshold needed for the segmentation of the lesion was calculated with the Otsu method, which consists of maximizing the between-class variance of the lesion and the skin digital level of the pixel values, based on the intensity of the histogram [136]. Then, a binary image was created in which all pixels with a lower value than that of the threshold had a digital value of 0 (pixels inside the lesion); otherwise the value was 1 (pixels of the surrounding healthy skin). Because of the inhomogeneity of the lesions, some pixels inside the lesion were classified erroneously as skin pixels, and vice versa.

To solve this, the algorithm worked as follows: firstly, the binary image was transposed, being 0 for the pixels of the skin and 1 for the pixels of the lesion; secondly, the lesion was considered as that with the biggest group of pixels with a value of 1, while the rest of groups with a value 1 but less than 15.000 pixels were considered to belong to the skin, so,

their value was automatically changed to 0; finally, the black areas inside the lesion (with a value of 0) were converted to a value of 1, obtaining the mask to segment the lesion.

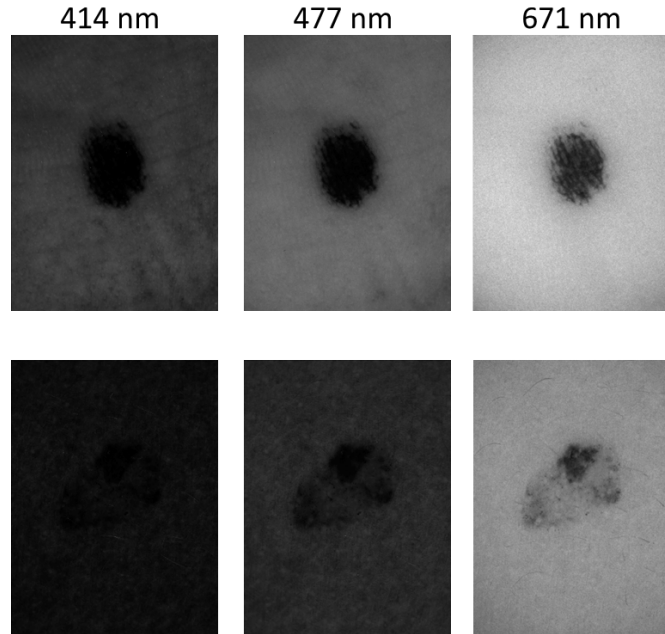


Figure 4.6 Reflectance images at 414 nm, 477 nm and 671 nm for two different lesions; the lesion on the top is a clear example of a highly pigmented lesion. Higher melanin absorbance at shorter wavelengths make the lesion to appear smaller at 671 nm; in this case, the image at 414 nm was used for the segmentation. In the one in the bottom, the contrast of the lesion and the surrounding skin at 414 nm is not enough as it is not as pigmented as the first one, so the next spectral image at 477 nm was used for the segmentation.

The Otsu method is as global thresholding which can only be used in lesions which are clearly different from the skin. In consequence, a good segmentation was difficult for those lesions that were not homogeneous at all. In such cases, the reflectance image was divided into 4 different subimages, allowing different thresholds adapted to the different areas of the lesion to be calculated (Figure 4.7). Moreover, in order to check if the lesion was well-segmented, its image appeared at the GUI software window. Figure 4.8 shows the flow chart of the segmentation process used.

Once the segmentation was done, the software automatically computed several images in terms of pseudo-CIELAB colour differences ( $\Delta E$ ) between the segmented lesion and the averaged surrounding skin, the goodness-of-fit coefficient (GFC), and the Individual Typology Angle (ITA) (Figure 4.9).

Besides spectral and colour information, several physical characteristics of the lesion could be also computed with the developed GUI: the dimensions in the X and Y axis, the area and the perimeter, which were obtained in terms of number of pixels and were converted to millimetres using a conversion factor; and the eccentricity, computed as the ratio of the distance between the foci of the ellipse which envelops the lesion and its major axis lengths; 0 means that the lesion is a circle and 1 a line segment. However, these

parameters were not finally used due to fact that the 3D system also included in the multiphotonic platform allowed this information to be obtained in a more precise way (Figure 4.10).

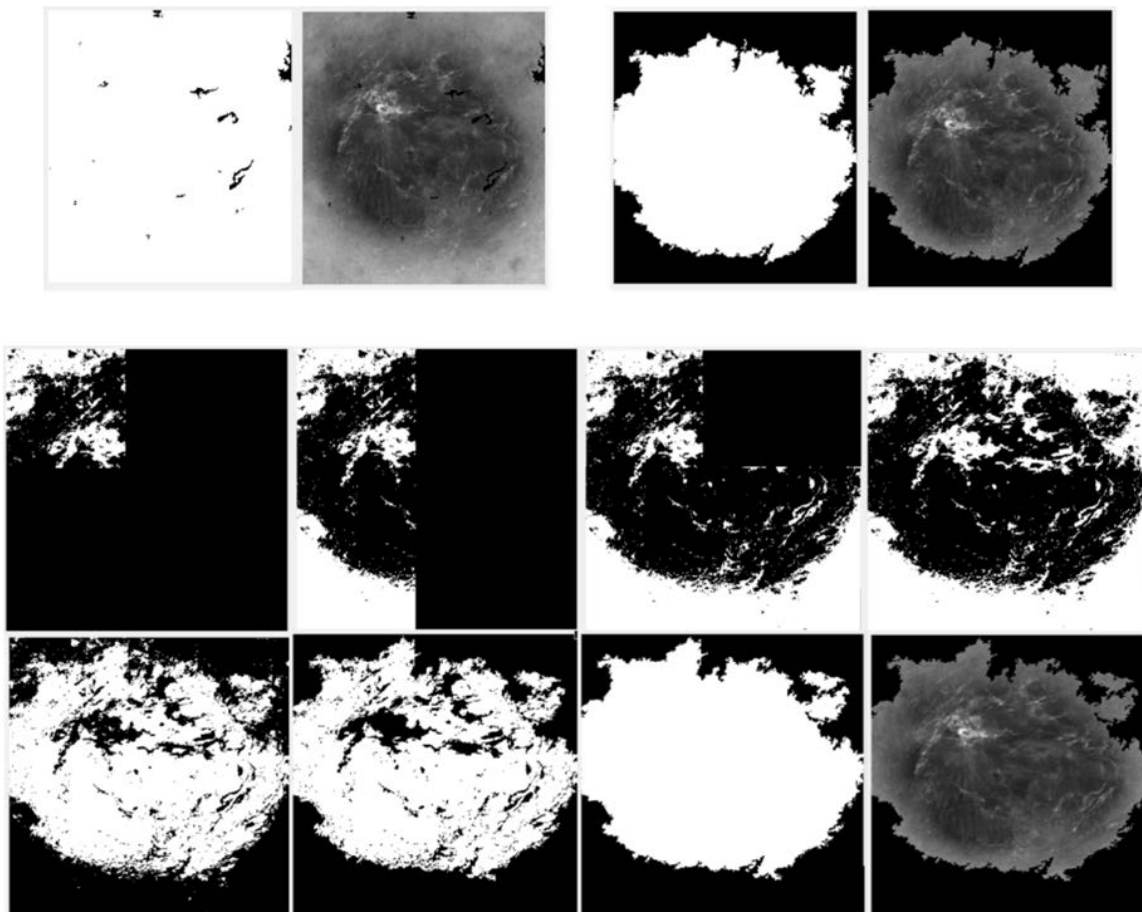


Figure 4.7 Top: From left to right, a non-homogenous lesion segmented with only one threshold and the same lesion segmented with 4 different thresholds, respectively. Bottom: steps of the segmentation algorithm. The upper images correspond to the implementation of the Otsu method for each subimage. The images at the bottom are (from left to right): transposition, removal of pixel groups of the lesion with less than 15.000 pixels, fill in the black areas to obtain the final mask, and finally, the segmented lesion.

Besides spectral and colour information computed using the former software, a second GUI with Matlab® was also programmed in order to operate with the reflectance images at different wavelengths, trying to enhance any particular spectral feature potentially different in healthy and malignant tissue that might be useful in discriminating among different types of skin lesions. The idea behind this was proposing easy calculations to resemble distribution maps of chromophores as other authors have already proposed. For instance, bilirubin (B), erythema (E), and the parameter to differentiate melanomas from nevi (p) suggested by Diebele et al. [103] and Bekina et al. [110] (see section 2.7.1 and 4.2 for more information on these parameters).

#### 4. IMAGE PROCESSING AND ANALYSIS

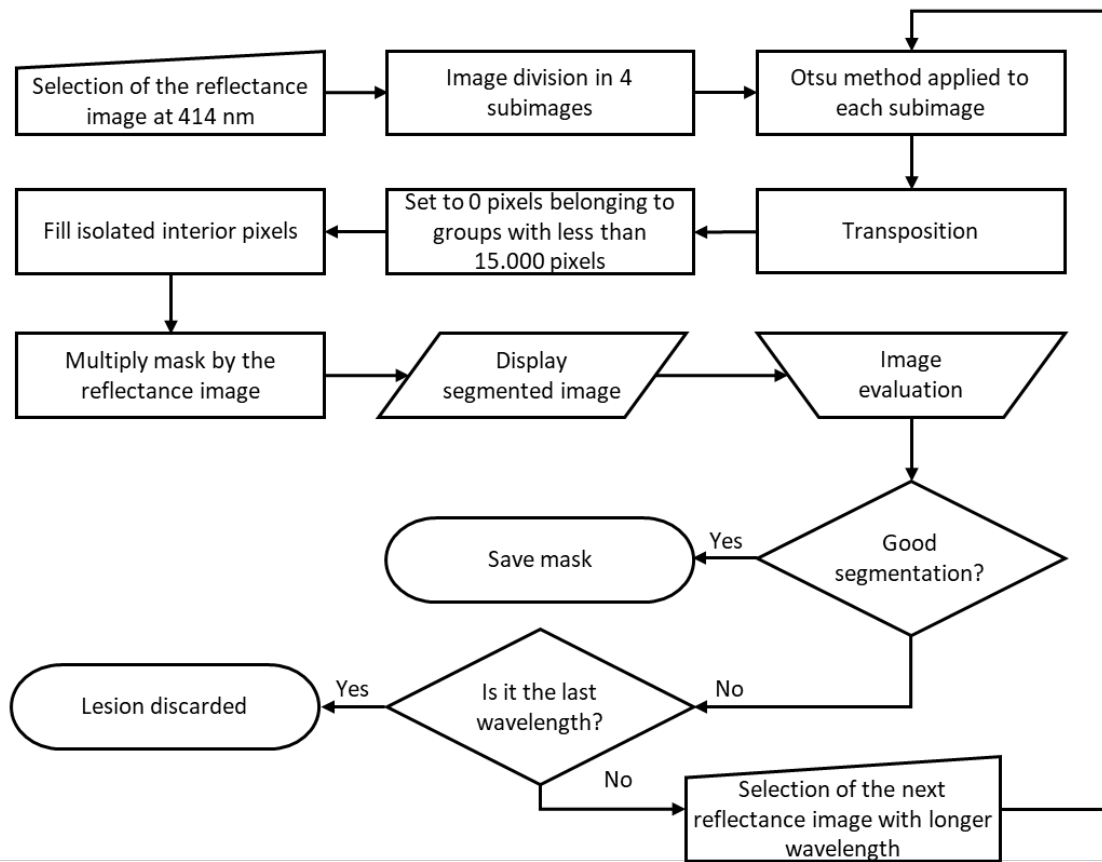


Figure 4.8 Flow chart of the segmentation process.

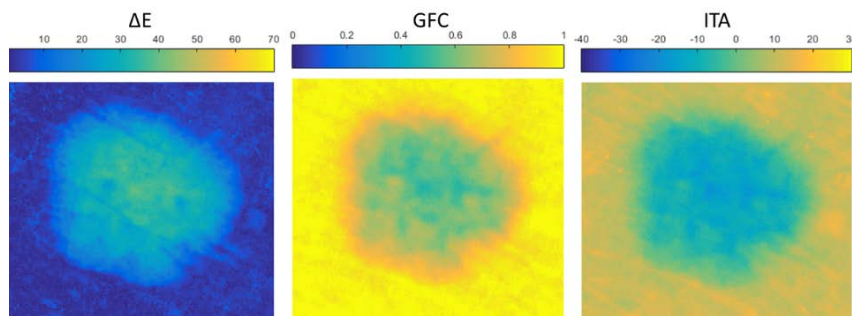


Figure 4.9 Images in terms of pseudo-CIELAB colour differences ( $\Delta E$ ), goodness-of-fit coefficient (GFC) and Individual Typology Angle (ITA) between the lesion and the averaged surrounding skin for a common nevus (refer to figure 4.4. for the images in terms of pseudo-CIELAB colour coordinates of the same lesion).

Lesion's Characteristics	
X Length	2.28 mm
Y Length	2.14 mm
Perimeter	9.51 mm
Area	3.58 mm <sup>2</sup>
Eccentricity	0.45

Figure 4.10 Physical parameters calculated after the segmentation of the lesion.

As it can be seen in Figure 4.11, the 24 reflectance images (8 corresponding to each degree of polarization) were shown simultaneously on the screen with an identification number at the left upper corner.

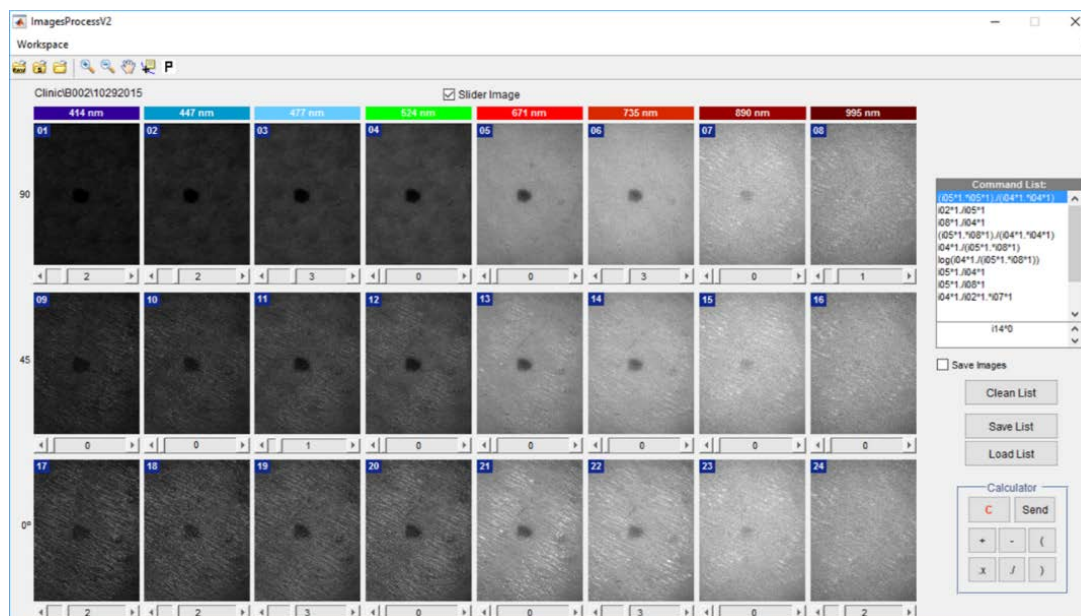


Figure 4.11 Graphical User Interface (GUI) using Matlab® software to operate with reflectance images.

In order to perform any math operation within reflectance images, a “calculator” was implemented with the following buttons: add (+), subtract (-), multiply (\*), divide (/), parenthesis “()” and clear (C). To insert the name of a reflectance image in the calculator command box, only a click on the desired image was necessary and, after sending the formula, a new window with the resulting image was opened.

#### 4.2. Parameters analysed: spectral, colour and textural information

Based on a preliminary analysis of a small group of lesions with both softwares presented and also taking into account the existing literature, three different groups of parameters were computed from the reflectance images of the lesions in order to be considered for further discrimination between benign and malignant ones.

The first group consisted of pixel by pixel spline interpolation values (from 415 nm to 995 nm with steps of 10 nm) of the 8 previous reflectance and absorbance images, in order to obtain more accurate information. Additionally, differences between the average of a region of interest (ROI) of healthy surrounding skin, which was selected manually to avoid other small lesions and hairs, and the segmented lesion itself were also computed in terms of reflectance and absorbance to prevent the patient’s skin influencing the results.

Additional images containing a second group of parameters were computed to look for colour features of the skin lesions; pseudo-CIELAB colour coordinates obtained from the interpolation of the reflectance images from the wavelengths of the system, as well as the

ITA parameter were used for this purpose. Additionally, more complex parameters based on colour differences between each pixel of the lesion and the averaged colour of the whole lesion were also considered, as well as colour differences between each pixel of the lesion and the averaged colour of the surrounding healthy skin, including the pseudo-CIELAB  $\Delta E$  colour difference and the GFC. The interpolated reflectance values, the D65 illuminant, and the CIE 2<sup>o</sup> standard observer were used to compute the colour data in all cases [134], [137].

The third group of parameters consisted of what we called *empirical parameters*, i. e., parameters empirically computed by operating with reflectance values at different wavelengths to enhance any particular spectral feature potentially different in healthy and malignant tissue that might be useful in discriminating among different types of skin lesions, as previously described:

$$Par_m(i, j) = f(Refl_{\lambda n}(i, j)), \quad (4.3)$$

where  $Par_m(i, j)$  is a particular parameter and  $f(Refl_{\lambda n}(i, j))$  is a function of the reflectance images computed from several wavelengths (they can be added, subtracted, multiplied etc.) in order to highlight subtle differences among lesions of different etiology.

For instance, Diebele et al, [103] and Bekina et al, [110] proposed the following parameters to account for erythema (E) and bilirubin (B), respectively, and were used in this thesis:

$$E = I_{660}(i, j)/I_{545}(i, j) \quad (4.4)$$

$$B = I_{450}(i, j)/I_{660}(i, j) \quad (4.5)$$

where  $I_{\lambda}$  is the intensity of diffuse light reflected from the skin at a specific wavelength of a multispectral system composed of 4 different spectral bands - three in the VIS (450 nm, 545 nm and 660 nm) and one in the NIR (940 nm).

The same authors also proposed a melanoma index (p) as follows:

$$p = k \cdot (I_{540}(i, j)/(I_{650}(i, j) \cdot I_{950}(i, j))), \quad (4.6)$$

where  $k$  is the intensity coefficient that describes the white etalon reference used for the calibration of the system.

These empirical parameters have been adapted to the wavelengths of our system and other empirical ones, which were also considered useful to highlight spectral differences between benign and malignant lesions. Up to our experience, the following ones were added too for the analysis:

$$Emp1 = \frac{Refl_{671}^2(i, j)}{Refl_{524}^2(i, j)}, \quad (4.7)$$

$$Emp2 = \frac{Refl_{477}(i, j)}{Refl_{671}(i, j)}, \quad (4.8)$$



$$Emp3 = \frac{Refl_{995}(i, j)}{Refl_{524}(i, j)}, \quad (4.9)$$

$$Emp4 = \frac{Refl_{671}(i, j) \cdot Refl_{995}(i, j)}{Refl_{524}^2(i, j)}, \quad (4.10)$$

$$Emp5 = \frac{Refl_{524}(i, j)}{Refl_{671}(i, j) * Refl_{995}(i, j)}, \quad (4.11)$$

$$Emp6 = \log(Emp5), \quad (4.12)$$

$$Emp7 = Emp5 - \left( \frac{Refl_{524_{skin}}(i, j)}{Refl_{671_{skin}}(i, j) \cdot Refl_{995_{skin}}(i, j)} \right), \quad (4.13)$$

$$Emp8 = \frac{Refl_{671}(i, j)}{Refl_{524}(i, j)}, \quad (4.14)$$

$$Emp9 = \frac{Refl_{671}(i, j)}{Refl_{995}(i, j)}, \quad (4.15)$$

$$Emp10 = \frac{Refl_{524}(i, j)}{Refl_{447}(i, j) \cdot Refl_{890}(i, j)}, \quad (4.16)$$

where  $Refl_{\lambda n}(i, j)$  is the reflectance at a specific wavelength and the subindex skin refers to the averaged reflectance of the parameter for the healthy skin surrounding the lesion.

Specifically, they were proposed as a means to obtain information of haemoglobin (Emp1), bilirubin (Emp2), melanin (Emp3, Emp4), index of melanoma (Emp5, Emp6, Emp7), erythema (Emp8), oximetry (Emp9) and an additional parameter to highlight the reflectance and absorbance differences between melanomas and nevi (Emp10).

Next, classical statistical descriptors were obtained for every segmented lesion in terms of all parameters, i. e., mean ( $\tilde{x}$ ), standard deviation ( $\sigma$ ), maximum and minimum.

Moreover, as a first approach to the extraction of textural information, we used the analysis of the statistical properties of the histogram for any of the parameters calculated, also known as first order statistics [69], [71]. This analysis includes the study of some features such as entropy (Ep), a well-known statistical measure of randomness, energy (En), a numerical descriptor of the image uniformity having 1 as its maximum value for a constant image, and the third central moment ( $\mu_3$ ), which accounts for the skewness of the histogram. The mathematical description of these features are shown in the following equations:

$$Ep = - \sum_{i=0}^{n-1} P_i \log_2(P_i), \quad (4.17)$$

$$En = \sum_{i=0}^{n-1} P_i^2, \quad (4.18)$$

$$\mu_3 = - \sum_{i=0}^{n-1} (i - m)^3 P_i, \quad (4.19)$$

where  $n$  is the number of bins or intervals in which the histogram is divided into,  $P_i$  is the relative frequency of the bin  $i$  of the histogram and  $m$  is the mean of the parameter (see section 2.6 for a more detailed explanation of these statistical descriptors).

Accordingly, for any parameter from each of the three groups, as the reflectance at 415 nm or the ITA, the  $\tilde{x}$ ,  $\sigma$ , maximum, minimum,  $E_p$ ,  $E_n$  and  $\mu_3$  were calculated.

---

## 5. Results

---

In the fifth chapter the main results obtained with the multispectral imaging system developed are presented. Particular attention is firstly drawn to the measurement protocol, inclusion criteria and clinical measurements conducted. Then, the classification algorithm based on parameters explained in the former chapter and corresponding outcomes are shown. The chapter ends with a discussion section in which the results obtained are compared with others from the bibliography available.

### 5.1. Inclusion criteria and measurement protocol

Individuals included in the study were patients with potential skin tumours attended at the outcare patient clinic in the Melanoma Unit of the Dermatology Department from the Hospital Clinic i Provincial de Barcelona (Spain), and the Skin Cancer Unit from the Policlinico di Modena - University of Modena and Reggio Emilia (Italy), referred for a single suspicious lesion (priority access with other medical doctor indications of the lesion of interest) or for a total body screening.

Each lesion which was referred as priority access was considered as a suspicious lesion unless presenting a clearcut clinical-dermoscopic features of benign nature. All suspicious lesions were included to be measured with the novel technologies. One or multiple benign lesions belonging to one of the classification categories, explained below, were also included depending on the criteria of the physician. However, it was necessary to take into account that some areas of the body were difficult to measure, such as folds, scalp and some areas of the face due to the fact that the 41-mm metal ring needed to be used with the OFI, 3D and multispectral systems. In these cases, the lesions were discarded.

The benign lesions detected during the examination were classified as seborrheic keratosis, vascular lesion, dermatofibroma or melanocytic nevus; and the suspicious lesions were classified as predominantly clinical suspect (i. e., ugly duckling lesions), predominantly dermoscopic suspect (dermoscopic criteria), suspect because changing digital monitoring, combination of them and not defined.

All patients provided written informed consent before any examination and ethical committee approval was obtained. The study complied with the tenets of the 1975 Declaration of Helsinki (Tokyo revision, 2004). The lesions were diagnosed by dermatologists (JM, SP, FP and AB in Barcelona, SB, AC, BF, CF in Modena) using a commercial dermoscope and the confocal laser scanning microscope VivaScope® 1500 from MAVIG [138].

## 5. RESULTS

---

A basic measurement protocol was implemented to ensure the measurements for all lesions were done correctly and exactly in the same manner in all cases. First of all, the lesion was photographed with a digital camera, obtaining a minimum of two clinical images: the first one to image the skin area where the lesion was located at a distance of approximately 50 cm, with the lesion of interest roughly in the centre of the frame; and the second one closer and, if considered necessary, together with a fixed ruler.

Secondly, a comfortable position for the patient was needed to lie still during measurements. To achieve this, the patient lied on a stretcher, and if needed, with a cushion under the part of the body which was to be measured enabling a more stable surface.

Thirdly, the area of interest was cleaned with alcohol and, if it was a hairy zone, the hair was carefully cut instead of shaving in order to avoid irritation or erythema of the skin, which could influence the information taken by the multiphotonic platform. Concretely, for the multispectral system the hair could difficult the later segmentation of the lesion (see next section), and the erythema could mask effects due to changes in colour of the skin.

Fourthly, lesions were classified according with their clinical presentation based on the elevation upon the skin level as flat, papular (dome shape  $< 1\text{cm}$ ), plaque (palpable, raised lesions) or nodular (dome shaped  $> 1\text{cm}$ ); and coloration as partially/largely pigmented ( $>25\%$ ), light pigmented (light brown colour or colour hues slightly darker than the surrounding skin), hypopigmented ( $< 25\%$ ) or amelanotic (pink or reddish).

Fifthly, the special double-coated adhesive was attached to the metal ring, and then the metal ring was applied to the skin of the patient with the lesion as centred as possible and in the best angle according to the characteristics of the tumour and the positioning of the patient in the bed, according to the anatomical site to explore (Figure 5.1). Then, the measurements with the multispectral, OFI and 3D systems were done, with the help of the user manual explanations, or in the case of the multispectral system, with the indications of the pop-up windows. Finally, the small ring was attached inside the big one, and the measurements with the confocal system were done. If after the evaluation with the information obtained from the confocal system the lesion was still suspicious, it was excised and a histological analysis was carried out.



Figure 5.1 Patient lying in the bed while the practitioner prepares the big metal ring in order to measure a lesion with the multiphotonic platform

## 5.2. Clinical measurements and samples

654 skin lesions from patients of both hospitals were finally included in the study. Many different types of lesions were analysed, but not limited to melanomas, basal cell carcinomas, seborrheic keratosis, nevi, to mention a few. Most of the lesions could be successfully measured with the new experimental devices available in the multiphotonic platform: 94.8% with the multispectral imaging system, 93% with the 3D technology, 76% with the OFI head and 72% with confocal microscopy.

Regarding the multispectral system, while 94.8% of the lesions could be properly measured, the remaining 5.2% could not, due to the difficulty of using the big metal ring in some areas of the patients' body (32.4%) and because it was unavailable for some days along which an upgrading for the inclusion of the handle's button was carried out (67.6%) (Figure 5.2).

As it can be seen, from the 620 (94.8%) lesions that were measured, the clinical or histopathological diagnosis of 48 (7.7%) of them was still pending at the time of this report. From the 572 (92.3%) lesions with a known diagnosis, 502 (87.8%) could be properly segmented. The reasons why the other 70 (12.2%) could not be segmented are described next:

- 27 (38.7%) were non-pigmented lesions, making the definition of borders very difficult. This often happens with non-pigmented basal cell carcinomas (Figure 5.3).
- 18 (25.7%) were pigmented lesions but with irregular and blurred borders (Figure 5.4).
- 11 (15.7%) were lesions larger than the field of view of the camera (Figure 5.5).
- In 5 (7.1%) of the cases, there were misalignments along the spectral images taken at different wavelengths due to the patient's breath movement (Figure 5.6).
- In 5 (7.1%) of them there were hairs superimposed to the lesion, making it difficult to effectively apply the segmentation process (Figure 5.7).
- 4 (5.7%) were very colourful (they included many different colours) and the algorithm could not find a unique grey level which allowed the lesion to be differentiated from the surrounding skin (Figure 5.8).

The diagnosis of the remaining 502 lesions that could be properly segmented and analysed were the following: 290 (57.9%) corresponded to nevi (melanocytic, dysplastic, blue, junctional and Spitz nevi) (Figure 5.9); 95 (18.9%) were melanomas (Figure 5.10), 44 (8.9%) basal cell carcinomas (Figure 5.11 and Figure 5.12); 35 (7%) seborrheic keratosis (Figure 5.13); 34 (6.9%) other benign lesions, such as, angiomas, dermatofibromas and actinic keratosis; and 2 (0.4%) corresponded to squamous carcinomas.

The last three types of lesions were excluded from the analysis due to the low number of samples available in each category, which were not enough to perform the statistical

## 5. RESULTS

analysis and posterior classification method proposed. Therefore, 429 skin lesions were finally included in the study.

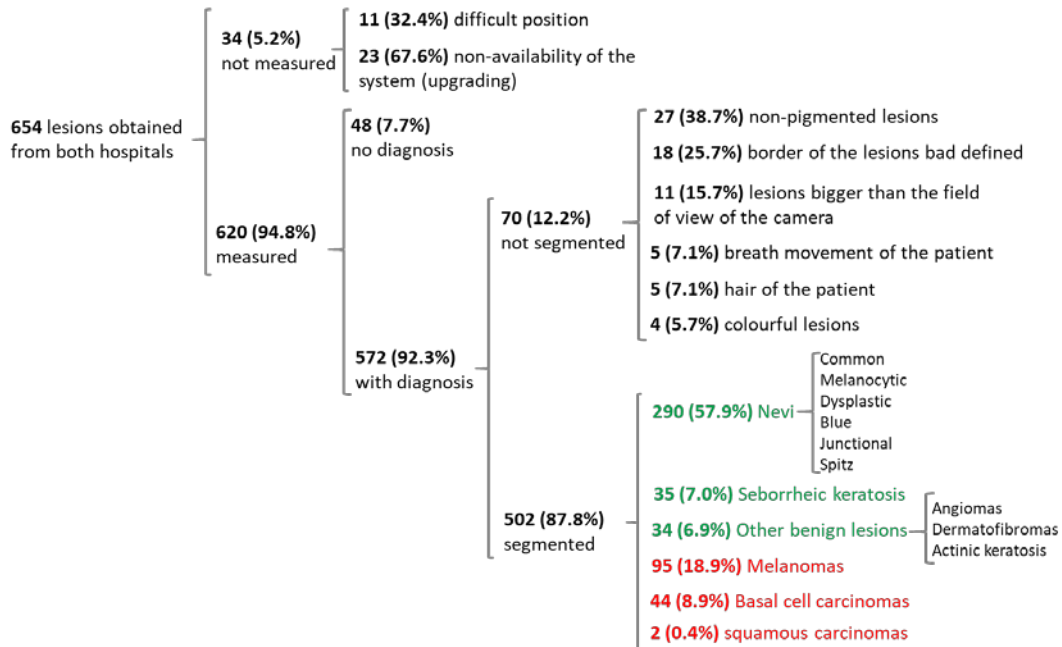


Figure 5.2 Summary of the lesions included in the study and measured with the multispectral imaging system. The lesions in green and red correspond to benign and malignant lesions, respectively.

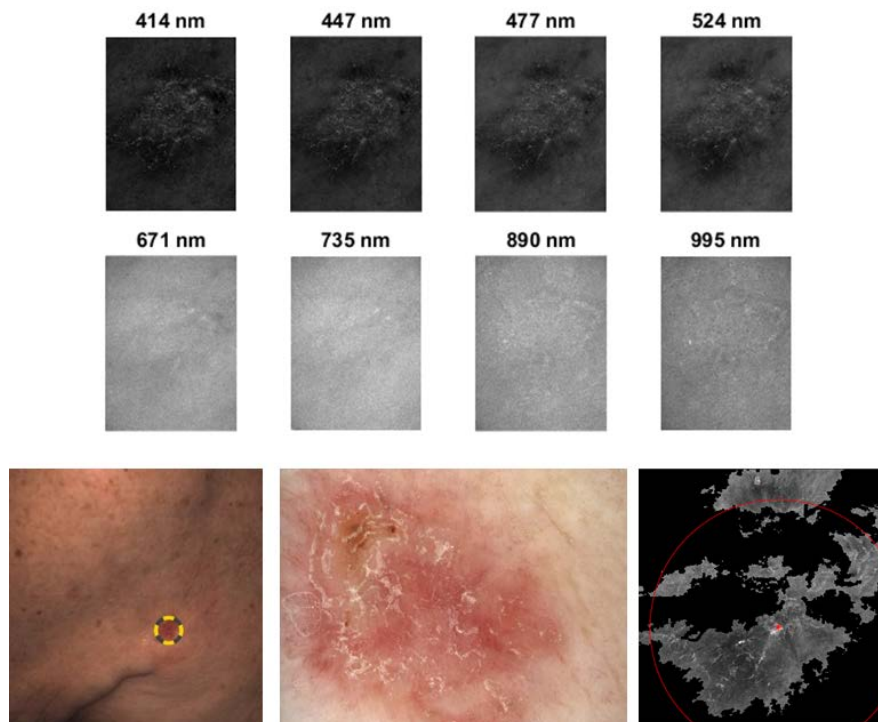


Figure 5.3 Reflectance images (top), conventional colour photography (bottom left), dermoscopic image (bottom centre), and segmented image of a non-pigmented basal cell carcinoma.

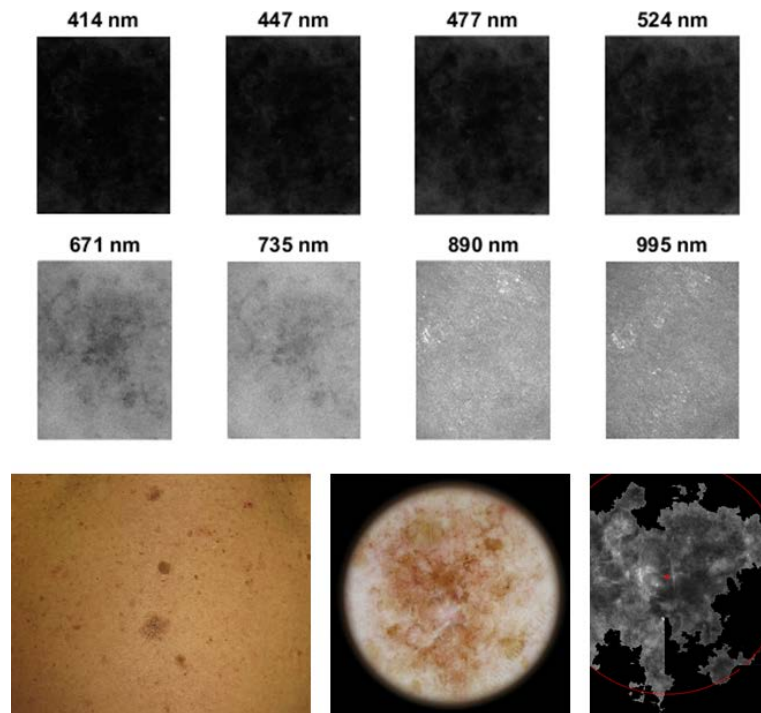


Figure 5.4 Reflectance images (top), conventional colour photography (bottom left), dermoscopic image (bottom centre), and segmented image of a pigmented lesion with irregular and blurred borders. The lesion has two differentiated areas in terms of colour (light and brown).

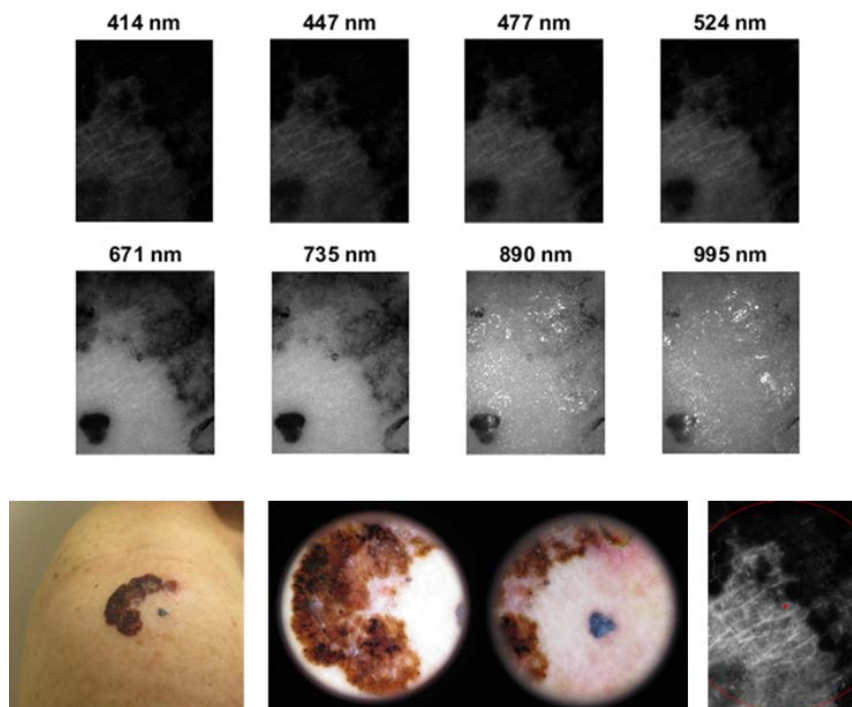


Figure 5.5 Reflectance images (top), conventional colour photography (bottom left), dermoscopic image (bottom centre), and segmented image of a pigmented lesion bigger than the field of view of the multispectral system.

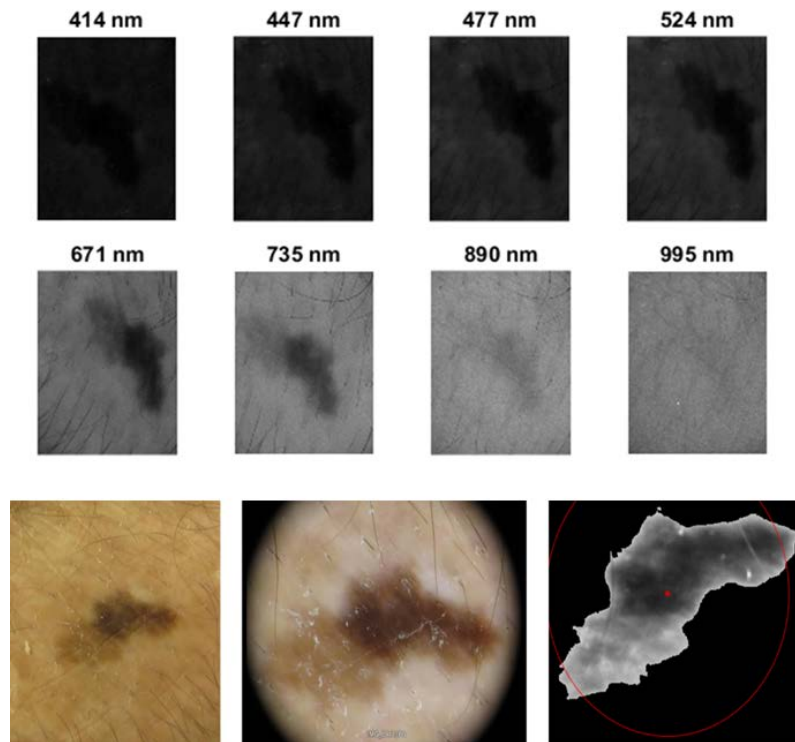


Figure 5.6 Reflectance images (top), conventional colour photography (bottom left), dermoscopic image (bottom centre), and segmented image of a lesion with misalignments of the lesion along wavelengths due to the breath movement of the patient.

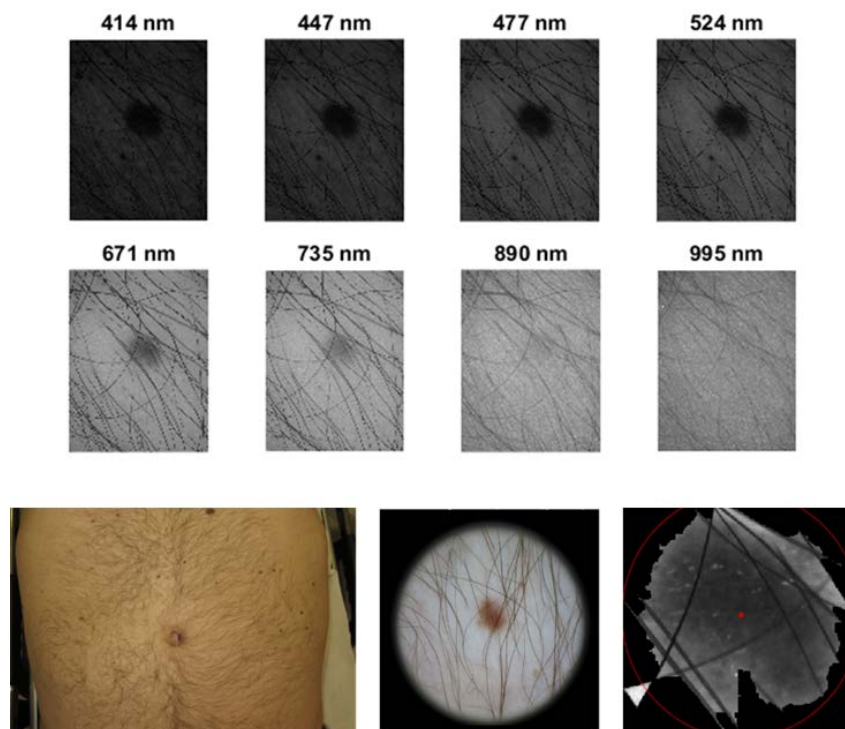


Figure 5.7 Reflectance images (top), conventional colour photography (bottom left), dermoscopic image (bottom centre), and segmented image of a lesion with hairy zones.



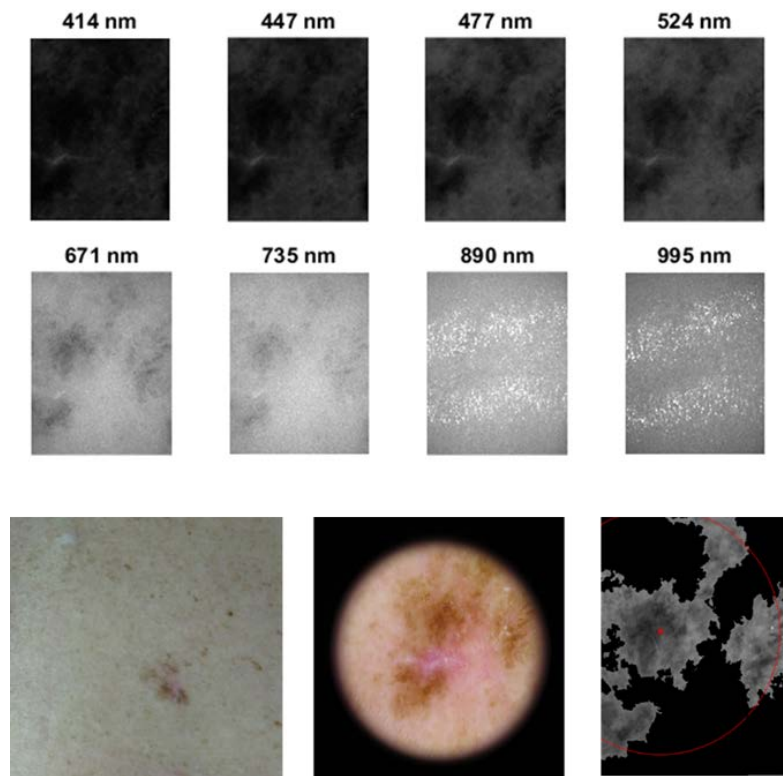


Figure 5.8 Reflectance images (top), conventional colour photography (bottom left), dermoscopic image (bottom centre), and segmented image of a lesion with many different colours.

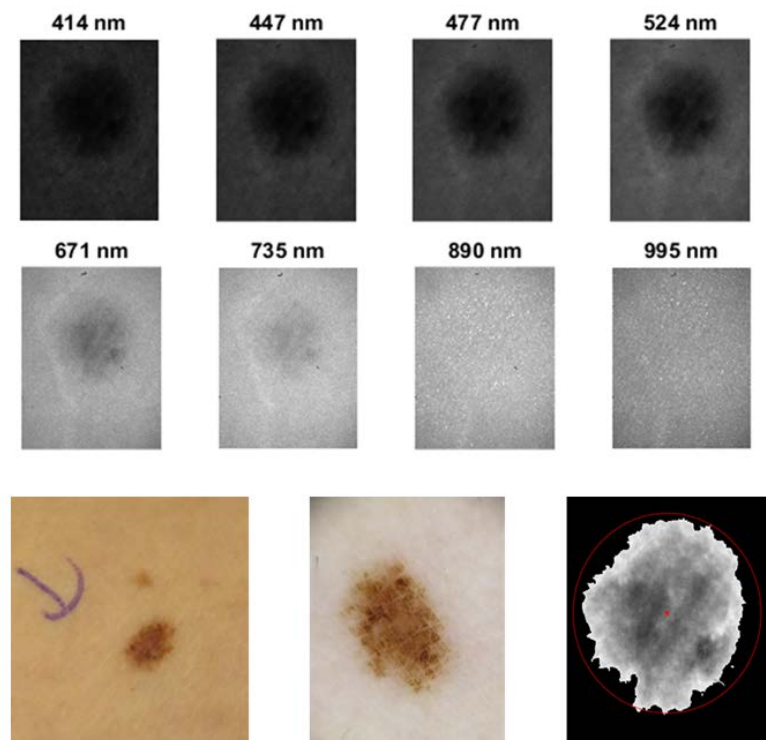


Figure 5.9 Reflectance images (top), conventional colour photography (bottom left), dermoscopic image (bottom centre), and segmented image of a nevus.

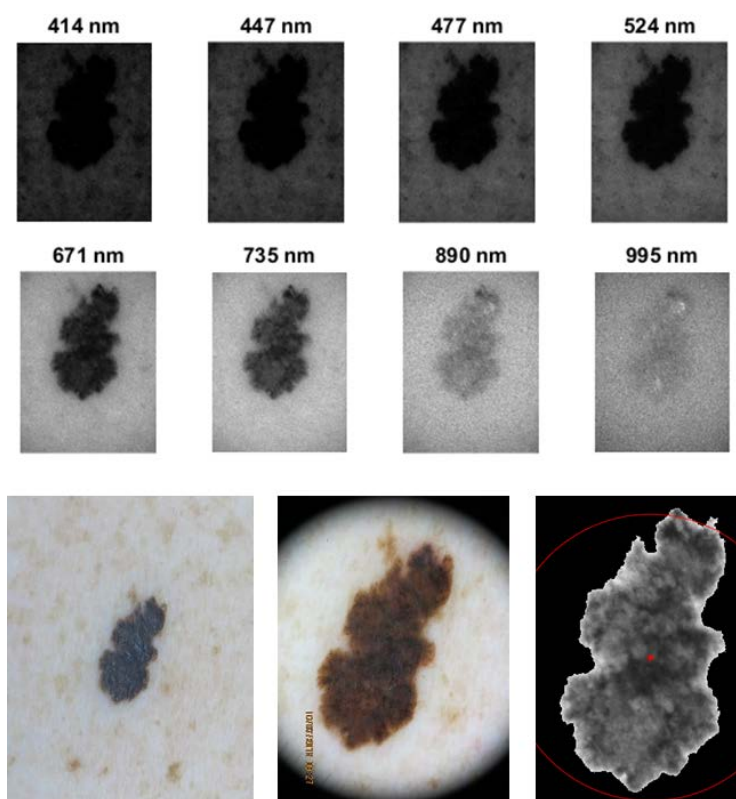


Figure 5.10 Reflectance images (top), conventional colour photography (bottom left), dermoscopic image (bottom centre), and segmented image of a melanoma.

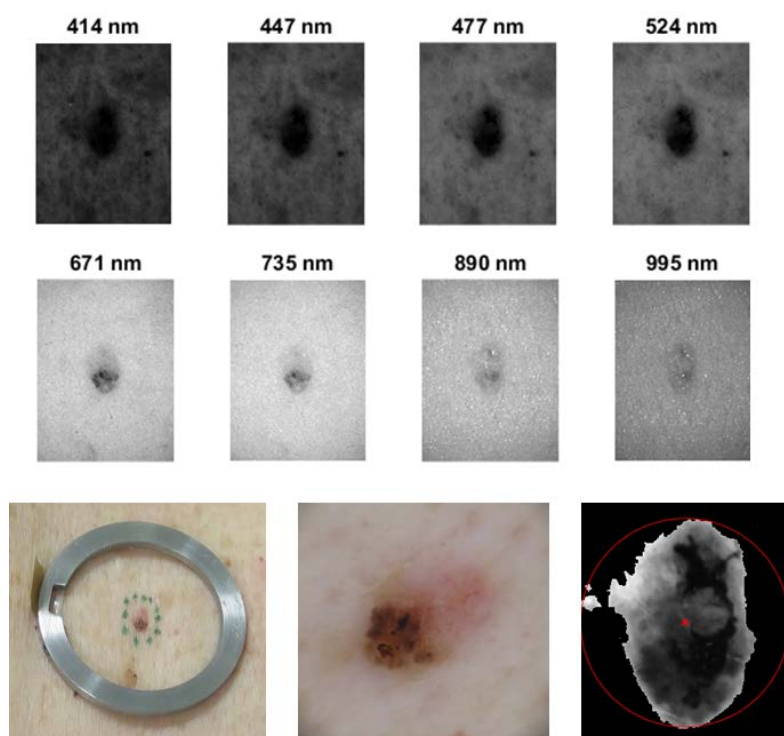


Figure 5.11 Reflectance images (top), conventional colour photography (bottom left), dermoscopic image (bottom centre), and segmented image of a pigmented basal cell carcinoma.

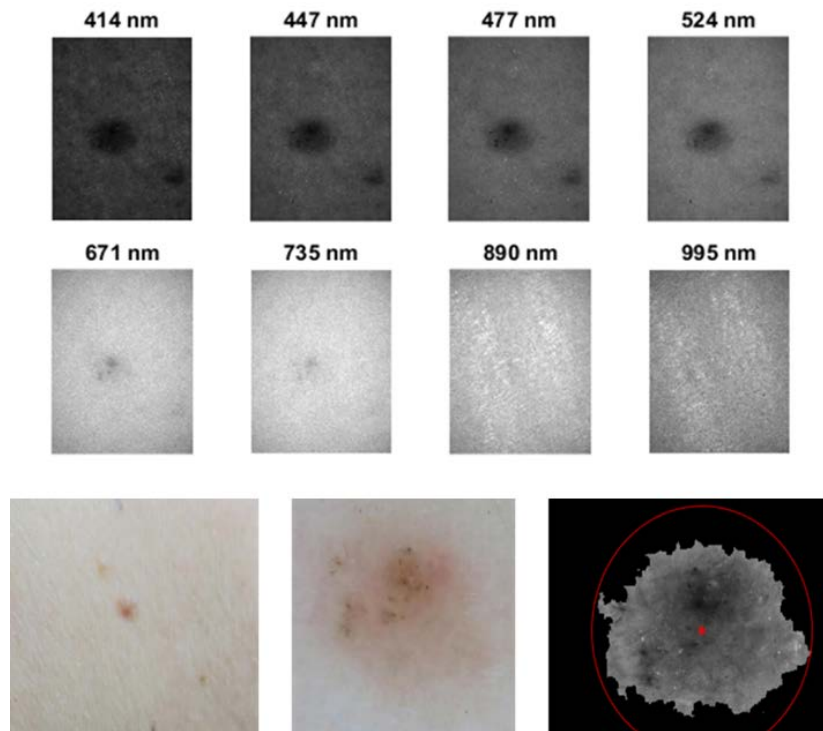


Figure 5.12 Reflectance images (top), conventional colour photography (bottom left), dermoscopic image (bottom centre), and segmented image of a non-pigmented basal cell carcinoma.

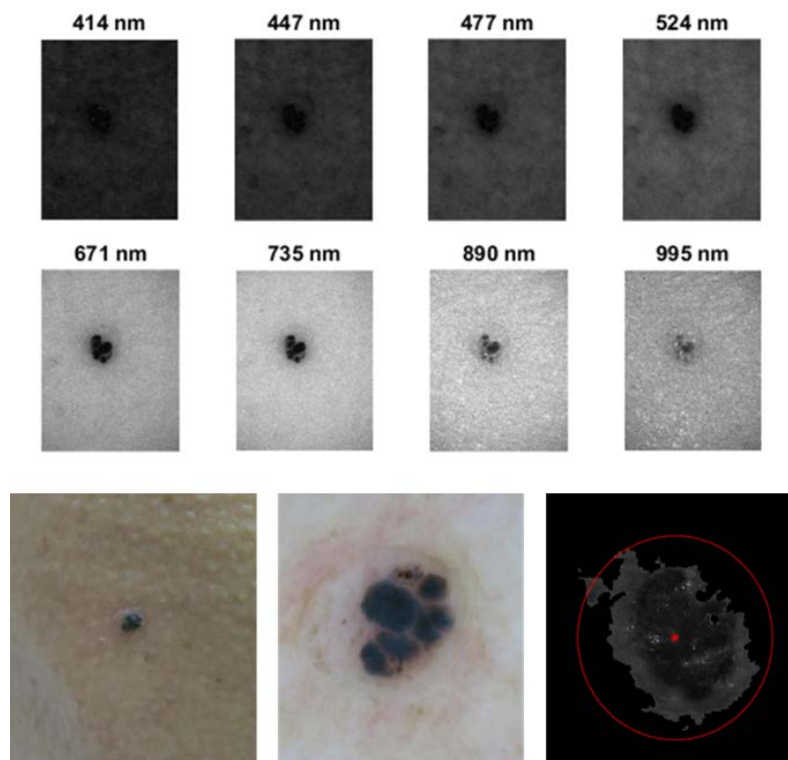


Figure 5.13 Reflectance images (top), conventional colour photography (bottom left), dermoscopic image (bottom centre), and segmented image of a seborrheic keratosis.

In the former figures, which show representative reflectance images of several skin lesions, it can be seen that nevi are usually more homogenous at all wavelengths than the other lesions. Furthermore, the infrared light, which penetrates deeper in the skin, shows that melanomas generally grow deeper as they can be distinguished from the surrounding skin at longer wavelengths. Basal cell carcinomas usually present blurred borders, and the contrast between the lesion and the skin is lower, especially for the non-pigmented ones.

### 5.3. Classification algorithm and outcomes

As commented previously, from the 429 lesions included in the analysis 290 were nevi; and 139 were malignant (95 melanomas and 44 basal cell carcinomas). It is also worth noting that the limitation of most studies is the inclusion of pre-selected lesions according the histopathological diagnosis while our study was a prospective study including consecutive lesions that could enter in the differential diagnosis of melanoma. In general, some basal cell carcinomas can be easily diagnosed clinically but dangerous melanomas, as amelanotic melanomas or nodular melanomas, can be easily misdiagnosed as basal cell carcinomas. Therefore, the approach used in our study is more approximate to what happens in real life were basal cell carcinomas are at least 10 times more frequent than melanomas and can be misdiagnosed if not considered.

The averaged reflectance ( $\pm\sigma$ , standard deviation) of nevi, melanomas and basal cell carcinomas can be seen in Figure 5.14. In agreement with previous publications [1], [139], the averaged reflectance of melanomas (or equivalently absorbance) shows a trend to be lower (higher) than that of nevi. However, this difference decreases when considering the great variance among lesions of the same type, which makes the classification difficult if only averaged values are taken into account.

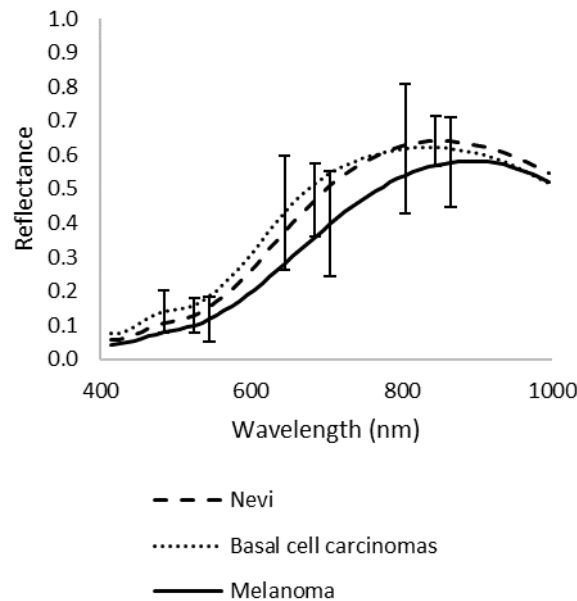


Figure 5.14 Averaged reflectance ( $\pm\sigma$ , standard deviation) of nevi, melanomas and basal cell carcinomas.

In order to overcome this limitation, histograms for the whole lesion with all parameters were also plotted. Figure 5.15 depicts specific examples of histograms of a nevus, a melanoma and a pigmented basal cell carcinoma in terms of reflectance at 414 nm and 671 nm. The averaged spectral reflectance ( $\tilde{x}$ ), the standard deviation ( $\sigma$ ), maximum, minimum and corresponding entropy ( $E_p$ ),  $E_n$ ,  $\mu_3$  are also shown.

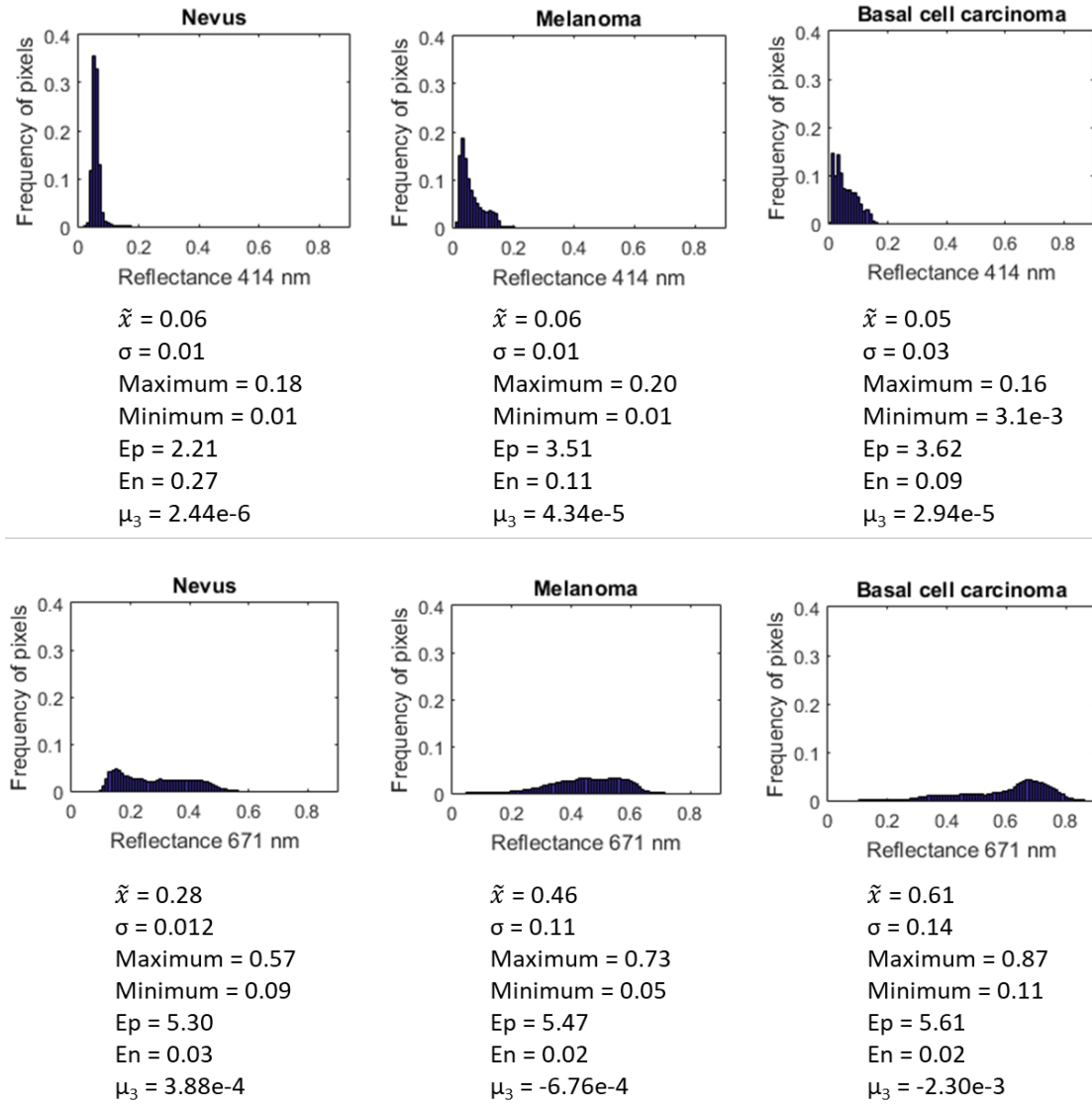


Figure 5.15 Histograms of a nevus, a melanoma and a pigmented basal cell carcinoma in terms of spectral reflectance at 414 nm (top), and at 671 nm (bottom) with their respective values of mean ( $\tilde{x}$ ), standard deviation ( $\sigma$ ), maximum, minimum, entropy ( $E_p$ ), energy ( $E_n$ ), and third central moment ( $\mu_3$ ).

The results show that the averaged reflectance, the standard deviation and the maximum and minimum at 414 nm for the three lesions are very similar. In contrast, the histograms look completely different; the nevus is linked to a higher  $E_n$  and a lower  $E_p$  since its pigmentation is more uniform than the melanoma and basal cell carcinoma. With regard to the skewness ( $\mu_3$ ), the nevus presents a practically symmetrical distribution and

thus, the lowest value. On the other hand, the lesions have enhanced spectral differences at 671 nm, as expected from Figure 5.14, and thus, the averaged reflectance is clearly different; however, the En and the Ep remain more similar in this case in comparison to 414 nm, while the melanoma and basal cell carcinoma are skewed to the left (negative) in terms of the third central moment contrary to what was obtained for the nevus.

In order to decide which lesions were malignant (melanomas and basal cell carcinomas), a classification algorithm was developed including the complete dataset of the 429 skin lesions (nevi, melanomas and basal cell carcinomas) with their corresponding information calculated previously from all the parameters described in section 4.2: first, second and third groups which are based on spectral, colour and empirical information, respectively. And for each parameter the following statistical descriptors were available: mean, standard deviation, maximum, minimum, entropy, energy and third central moment. To this end, the data was splitted in a training and a validation set of the same size including half of the nevi, basal cell carcinomas and melanomas.

Using the training set, upper and lower thresholds were firstly defined for each parameter as the interval limits that included all nevi. The upper (lower) threshold was chosen as the value of the nevus with the highest (lowest) value after some nevi were discarded according to the following formula:

$$\text{Nevi outliers} = \tilde{x}_{nevi} \pm 2 \cdot \sigma_{nevi} \quad (5.1)$$

where  $\tilde{x}_{nevi}$  and  $\sigma_{nevi}$  are the average and standard deviation, respectively, in terms of each parameter calculated from all nevi lesions in the training set. For instance,  $\tilde{x}_{nevi}$  and  $\sigma_{nevi}$  can be those corresponding to the energy of the reflectance at 995 nm or the maximum lightness ( $L^*$ ) of all pixels belonging to a lesion diagnosed as nevus.

All lesions above or under the upper and lower thresholds for at least one parameter were classified as malignant.

Taking into account the difficulty of working with as much as 1309 parameters (187 reflectance, absorbance and colorimetric parameters x 7 statistical descriptors), it was necessary to select only the most useful ones.

This relative importance was achieved in 3 steps: firstly, in order to detect the highest number of melanomas and basal cell carcinomas, the lesions in the training set which were detected using only one parameter were found and this concrete parameter was selected. Secondly, the lesions which were detected using only two parameters were found. However, it was necessary to decide for each lesion which was the best parameter, calculating thus, the rate of differentiation between the amount of melanomas and basal cell carcinomas classified as malignant and the quantity of nevi classified as malignant. Then, the parameter which had the best rate was chosen. Finally, the same process was done successively with those lesions which were detected using 3, 4, 5... parameters, until the maximum number of melanomas were detected. The other parameters were discarded as they did not introduce any significant improvement in the detection of melanomas or basal cell carcinomas.

From all the parameters calculated, only 15 were found not to be redundant and finally selected for use in the classification algorithm. Each parameter with its respective threshold calculated previously in the training set with formula 5.1, was used to classify the lesions of the validation set in benign and malignant. Finally, those lesions which were classified for at least one parameter as malignant, were finally considered a malignant lesion as the final decision of the system. From these values, the sensitivity and specificity of the system were calculated.

The flow chart in Figure 5.16 shows the inner working of the classification algorithm in more detail. As formerly described, only those which allowed increasing the detection of malignant lesions were chosen, until the addition of more parameters did not improve the results in terms of sensitivity in the training set.

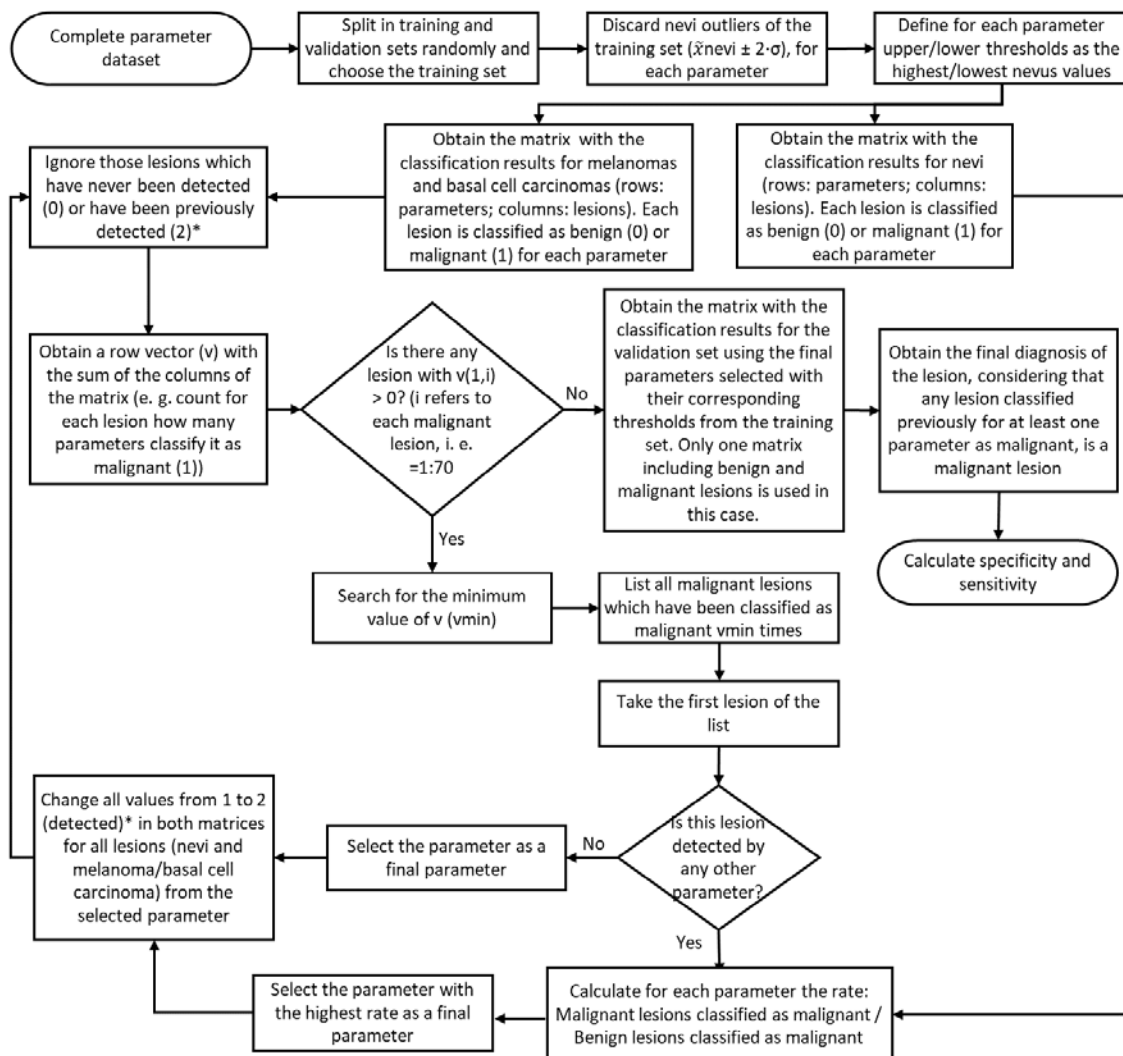


Figure 5.16 Flow chart of the classification algorithm.

From the first group (spectral reflectance (Refl) and absorbance parameters (Abs); and corresponding differences between the lesion and the surrounding healthy skin): En of

Abs<sub>875</sub>,  $\mu_3$  of Refl<sub>745</sub>,  $\tilde{x}$  of Refl<sub>645</sub> and  $\sigma$  of Abs<sub>935</sub>. Also, differences between lesion and surrounding skin in terms Ep of Abs<sub>465</sub>, En of Abs<sub>635</sub>,  $\mu_3$  of Abs<sub>985</sub>, and  $\mu_3$  of Refl<sub>975</sub>.

From the second group (colour-based parameters): maximum of  $L^*$ ,  $\sigma$  of  $a^*$  as pseudo-CIELAB colorimetric coordinates, and minimum  $\Delta E$  with the surrounding healthy skin as the reference, and maximum ITA.

From the third group (empirical parameters): maximum of Emp1, En of Emp6, maximum of Emp9.

Figure 5.17 shows the scatter plots of the 15 selected parameters. The corresponding upper and lower thresholds used for classification were calculated with the training set while the samples shown correspond to the validation set. The plots also show that some of the melanomas and basal cell carcinomas tend to have higher values beyond the upper/lower thresholds. Furthermore, Table 5.1, Table 5.2, Table 5.3 and Table 5.4 summarize the results of each selected parameter including the computed thresholds, mean,  $\sigma$ , maximum and minimum for any kind of lesion analysed, i. e., nevi, melanomas and basal cell carcinomas used in the validation set.

With the classification algorithm based on these 15 parameters, 6 out of 47 melanomas and none of the 22 basal cell carcinomas were misclassified (91.3% sensitivity); in contrast, 66 nevi from 145 were classified as malignant (54.5% specificity). Here, sensitivity or true positive rate is the probability of detecting malignant lesions (melanomas and basal cell carcinomas) and specificity or true negative rate is the proportion of nevi correctly identified. This information, which is often referred as confusion matrix, is shown in Table 5.5.

Many similar studies published in the literature only include in their analysis nevi and melanomas but not basal cell carcinomas; therefore, in order to be able to compare the results, it was necessary to calculate again the sensitivity and specificity of our system but only including nevi and melanomas in the analysis, being then of 87.2% (sensitivity) and 54.5% (specificity). The confusion matrix in this case can be seen in Table 5.6.



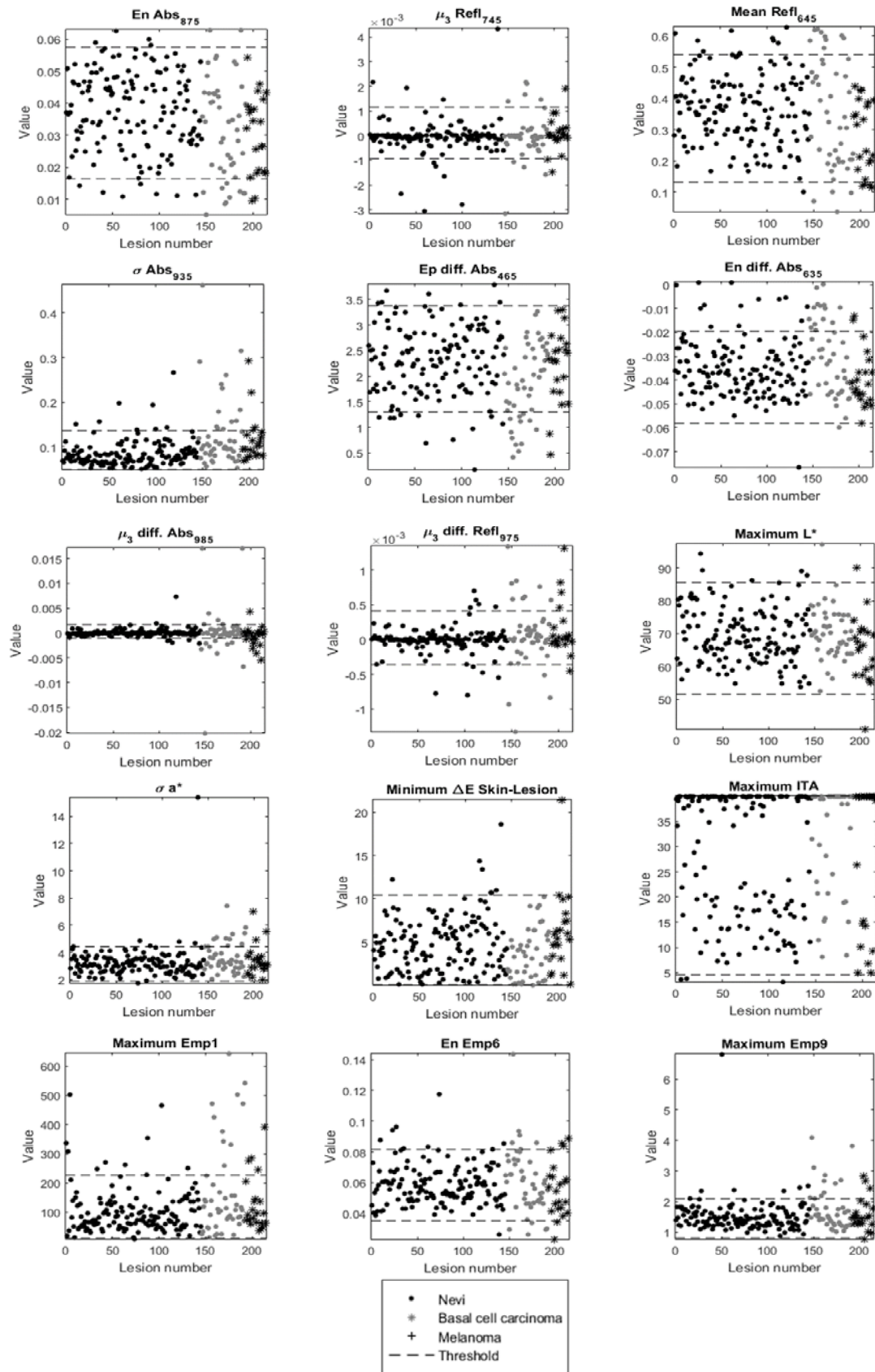


Figure 5.17 Scatter plots of the 15 selected parameters.

5. RESULTS

Table 5.1 Thresholds for the 15 selected parameters.

Parameters	Thresholds	
	Upper	Lower
En Abs <sub>875</sub>	5.75E-02	1.64E-02
$\mu_3$ Refl <sub>745</sub>	1.15E-03	-9.33E-04
Mean Refl <sub>645</sub>	5.40E-01	1.33E-01
$\sigma$ Abs <sub>935</sub>	1.37E-01	4.95E-02
Ep diff. Abs <sub>465</sub>	3.37	1.30
En diff Abs <sub>635</sub>	-1.95E-02	-5.81E-02
$\mu_3$ diff. Abs <sub>985</sub>	1.70E-03	-1.10E-03
$\mu_3$ diff. Refl <sub>975</sub>	4.13E-04	-3.60E-04
Maximum L*	85.59	51.39
$\sigma$ a*	4.44	1.89
Minimum $\Delta E$ Skin-Lesion	10.41	6.42E-02
Maximum ITA	40.00	4.55
Maximum Emp1	227.08	11.49
En Emp6	8.16E-02	3.51E-02
Maximum Emp9	2.10	8.08E-01

Table 5.2 Mean, standard deviation ( $\sigma$ ), maximum and minimum for the nevi included in the validation set, for the 15 selected parameters.

Parameters	Nevi			
	Mean	$\sigma$	Maximum	Minimum
En Abs <sub>875</sub>	3.77E-02	1.22E-02	6.25E-02	1.07E-02
$\mu_3$ Refl <sub>745</sub>	-3.76E-05	6.92E-04	4.35E-03	-3.06E-03
Mean Refl <sub>645</sub>	3.68E-01	1.13E-01	6.29E-01	1.02E-01
$\sigma$ Abs <sub>935</sub>	8.54E-02	2.97E-02	2.67E-01	5.05E-02
Ep diff. Abs <sub>465</sub>	2.30	6.76E-01	3.79	1.82E-01
En diff Abs <sub>635</sub>	-3.52E-02	1.22E-02	1.11E-03	-7.64E-02
$\mu_3$ diff. Abs <sub>985</sub>	4.77E-05	8.32E-04	7.39E-03	-2.04E-03
$\mu_3$ diff. Refl <sub>975</sub>	-6.91	1.84E-04	7.02E-04	-8.05E-04
Maximum L*	69.64	8.37	94.50	53.65
$\sigma$ a*	3.23	1.19	15.36	1.77
Minimum $\Delta E$ Skin-Lesion	4.77	3.22	18.58	9.50E-02
Maximim ITA	28.24	12.61	40.00	3.21
Maximum Emp1	104.07	78.40	503.79	9.79
En Emp6	5.86E-02	1.31E-02	1.17E-01	2.61E-02
Maximum Emp9	1.52	5.44E-01	6.82	8.91E-01

Table 5.3 Mean, standard deviation ( $\sigma$ ), maximum and minimum for the melanomas included in the validation set, for the 15 selected parameters.

Parameters	Melanomas			
	Mean	$\sigma$	Maximum	Minimum
En Abs <sub>875</sub>	2.86E-02	1.37E-02	6.28E-02	8.63E-03
$\mu_3$ Refl <sub>745</sub>	1.06E-04	8.15E-04	2.17E-03	-1.56E-03
Mean Refl <sub>645</sub>	2.79E-01	1.38E-01	6.01E-01	3.83E-02
$\sigma$ Abs <sub>935</sub>	1.23E-01	6.08E-02	3.16E-01	5.25E-02
Ep diff. Abs <sub>465</sub>	2.26	6.52E-01	3.30	4.60E-01
En diff Abs <sub>635</sub>	-3.91E-02	1.20E-02	-9.62E-03	-5.99E-02
$\mu_3$ diff. Abs <sub>985</sub>	-1.09E-04	3.12E-03	1.71E-02	-6.72E-03
$\mu_3$ diff. Refl <sub>975</sub>	9.02	3.43E-04	1.32E-03	-8.40E-04
Maximum L*	67.31	8.53	90.07	40.83
$\sigma$ a*	3.62	1.22	7.41	2.00
Minimum $\Delta E$ Skin-Lesion	5.37	3.85	21.46	5.78E-02
Maximim ITA	31.94	12.57	40.00	4.87
Maximum Emp1	169.58	147.75	644.01	21.39
En Emp6	5.30E-02	1.58E-02	8.89E-02	2.32E-02
Maximum Emp9	1.57	5.78E-01	3.80	7.85E-01

Table 5.4 Mean, standard deviation ( $\sigma$ ), maximum and minimum for the melanomas included in the validation set, for the 15 selected parameters.

Parameters	Basal cell carcinomas			
	Mean	$\sigma$	Maximum	Minimum
En Abs <sub>875</sub>	3.72E-02	1.50E-02	6.29E-02	5.26E-03
$\mu_3$ Refl <sub>745</sub>	-1.90E-04	7.91E-04	1.39E-03	-3.15E-03
Mean Refl <sub>645</sub>	4.37E-01	1.59E-01	6.21E-01	7.03E-02
$\sigma$ Abs <sub>935</sub>	1.25E-01	9.08E-02	4.63E-01	5.53E-02
Ep diff. Abs <sub>465</sub>	1.38	5.69E-01	2.54	4.18E-01
En diff Abs <sub>635</sub>	-2.16E-02	1.42E-02	1.59E-04	-4.63E-02
$\mu_3$ diff. Abs <sub>985</sub>	-3.18E-04	6.04E-03	1.71E-02	-2.01E-02
$\mu_3$ diff. Refl <sub>975</sub>	8.04	5.85E-04	1.35E-03	-1.32E-03
Maximum L*	71.62	9.08	97.37	52.47
$\sigma$ a*	3.53	7.84E-01	5.13	2.03
Minimum $\Delta E$ Skin-Lesion	2.09	1.74	5.20	1.17E-01
Maximim ITA	30.90	11.08	40.00	8.02
Maximum Emp1	123.50	121.39	471.16	13.68
En Emp6	7.29E-02	2.18E-02	1.44E-01	2.97E-02
Maximum Emp9	1.96	7.00E-01	4.10	1.25

## 5. RESULTS

---

Table 5.5 Confusion matrix of the validation set when including melanomas, basal cell carcinomas and nevi in the analysis.

		True condition	
		Melanomas and basal cell carcinomas	Nevi
Predicted condition	Total lesions: 214		
	Melanomas and basal cell carcinomas	63	66
	Nevi	6	79

Table 5.6 Confusion matrix of the validation set when including melanomas and nevi in the analysis.

		True condition	
		Melanomas	Nevi
Predicted condition	Total lesions: 192		
	Melanomas	41	66
	Nevi	6	79

### 5.4. Discussion

In a study of the first SIAscope scoring system applied to a dataset of 348 pigmented lesions (52 melanomas and remainder non-melanoma lesions, mostly nevi), Moncrieff et al. [107] obtained sensitivity and specificity values of 82.7% and 80.1%, respectively. As commented in chapter 2, the SIAscope is a multispectral system with four narrow-bands (from 400 nm to 1000 nm) that provides information about the amount of collagen, haemoglobin and melanin distribution in the epidermis and dermis of pigmented skin lesions in the form of maps called SIAscans. These maps presented by the MoleMate software have to be interpreted by general practitioners or dermatologists who have previously received training [5].

Similarly, Haniffa et al. [109] conducted a study that included 881 pigmented lesions. The observations, carried out by a 3-year-experienced dermatologist using the latest SIAscope software, obtained 87% and 91% sensitivity and specificity, respectively. In the same study, the observations made by a dermatologist with 20 years of experience resulted in 94% sensitivity and 91% specificity. The authors concluded that the use of SIAscope by an experienced dermatologist made no additional contribution over clinical diagnosis.

In a more recent study that analysed 188 lesions including three types of malignant lesions (21 melanomas, 9 basal cell carcinomas and 5 squamous cell carcinomas) and various benign lesions (122 nevi, 23 seborrheic keratosis, 7 dermatofibromas and 1 cherry angioma), Sgouros et al. [140] concluded that although SIAscope was not superior, it could support the results of dermoscopy. In this study, the sensitivity and specificity for suspected malignant lesions were 85.7% and 65.4%, respectively. The lower specificity compared with previous studies results from the inclusion of more types of malignant lesions. The authors

concluded that SIAScope should not be considered a replacement for the standard diagnostic procedure, but an additional tool for non-dermatologist clinicians.

Taking into account that the classification algorithm proposed in this thesis does not require the skills of a dermatologist to interpret a map, this study provides slightly higher sensitivity (91.3%) and lower specificity (54.5%) values than previous studies. Consequently, the inclusion of texture information can be considered relevant for the detection of melanomas and basal cell carcinomas.

However, one should bear in mind that the sensitivity decreases to 87.2% when basal cell carcinomas are not considered; nevertheless, this value is still similar to that obtained by an experienced dermatologist using the SIAScope.

On the other hand, as already stated in the state of the art section, MelaFind® is a 10-wavelength (430, 470, 500, 550, 600, 650, 700, 770, 880, 950 nm) system that generates 6 scores based on linear classifiers for each measured skin lesion. In this system, a lesion is recommended for biopsy if all 6 scores are above the threshold value [109]. After the measurement, the system provides a disorganization value and a treatment suggestion for dermatologists.

The FDA Summary of Safety and Effectiveness Data of MelaFind® [141] shows a much higher sensitivity (98.3%) to detect in situ and invasive melanomas (172/175 melanomas detected) than the SIAScope; however, the specificity was only of 10.8% (157/1457 of high grade dysplastic nevi, atypical melanocytic proliferation/hyperplasia lesions were classified as melanomas). Therefore, the use of MelaFind® generates a large number of false positives and consequently a large number of unnecessary biopsies. Other investigations were carried out in which different dermatologists were asked to evaluate and diagnose a specific number of lesions with and without information from the MelaFind®. The averaged sensitivities and specificities obtained were very similar to those previously shown, ranging from 96.9% to 98.3%, and from 9.2% to 9.9% [105], [142], respectively. The authors concluded that the information obtained with the MelaFind® should be used to decide the need for a biopsy, since in case of an experienced dermatologist MelaFind® could improve biopsy sensitivity with a modest effect on biopsy specificity.

The lower sensitivity shown in our system could be improved by defining more restricted upper and lower thresholds. However, this would also result in an increase of false positives and thus, a marked reduction of the specificity, which is unacceptable from the dermatologists' point of view. In fact, the detection of malignant lesions at early stages, when they can still be controlled and successfully excised, is crucial when dealing with skin cancer and this is the reason why dermatologists are more concerned with increasing sensitivity than specificity.

On the other hand, we should underscore that in contrast with MelaFind®, our study only compared melanomas and basal cell carcinomas with different kinds of nevi (common, melanocytic, dysplastic, blue, junctional and Spitz nevi) and melanomas with nevi.

Using the formula 2.28 described in section 2.7.1, Diebele et al [103] found values of 94% and 89% for sensitivity and specificity, respectively. In this case, the system developed by the authors consisted of a multispectral imaging camera (Nuance EX) with spectral bands from 450-950 nm in steps of 10 nm. The illumination system was a ring of halogen lamps with a polarizer orthogonal to the camera. However, they only analysed 65 nevi and 17 melanomas and a further verification of the algorithm is still pending. Our system obtained a slightly lower sensitivity when excluding basal cell carcinomas, taking into account that in contrast with the abovementioned study, it also included dysplastic nevi and non-pigmented lesions. These lesions present a further difficulty in the discrimination of melanomas, since they are unusual benign moles that may resemble melanomas. In addition, our study included many more lesions.

On the other hand, artificial intelligence is starting to enter the medicine field [143]. Specifically, Esteva et al. [144] used a deep convolutional neural network (CNN) to classify skin lesions from dermoscopic images. The algorithm was trained from a dataset of more than 100,000 images from 18 different clinician-curated, open-access online repositories, and from the Stanford University Medical Centre. An area under curve (AUC) of 96% for the detection of carcinomas, and 94% for the detection of melanomas was obtained, improving the performance of most of the 21 dermatologist which were asked to classify hundreds of lesions from a dermoscopic image. The conclusion of the study was that CNN could be a powerful tool for huge image datasets, and encouraging results will be probably obtained in the coming years. However, this is not the best tool for pilot studies in which new technologies are tested and the database of lesions is small.

According to all this, the addition of textural information, which has not been yet considered in any study, has been shown to be useful for the diagnostic of malignant lesions (melanomas and basal cell carcinomas) than the sole use of averaged spectral and colour information. The sensitivity (91.3%) and specificity (54.5%) values slightly improved in some cases those previously achieved by means of other multispectral systems without the need of an experienced dermatologist as it was based on a completely automatic algorithm. However, when only the melanomas and nevi were considered the sensitivity decreased to 87.2%, although this value was still similar to that obtained by experienced dermatologists through averaged spectral and colour features. It is also necessary to take into account that due to the system is composed of only eight different spectral bands, an error can be found in the reflectance and pseudo-CIELAB calculations, as far as such a value was spline interpolated. However, from our previous experience, this error should be limited since the reflectance curves of the lesions are rather smooth and without narrow peaks, meaning that bandwidths greater than 6-10 nm can be used to discriminate among them. In fact, similar spectral absorption curves for skin lesions have been previously reported [103].

Moreover, the system proposed has a specificity similar to that of confocal microscopy (55.1%) [138] but much closer to dermoscopy (84.1%) [145] than Melafind® (10.8%). On the other hand, our system has a slightly lower sensitivity than Melafind® (98.3%) and confocal microscopy (96.3%) [144], but closer than dermoscopy (89.2%) [145]. Therefore,

the system can help to improve the diagnosis of skin cancer as a supporting tool to dermoscopy and confocal microscopy.





---

## 6. Combination of the systems

---

This chapter comprises preliminary results obtained with the 3D system, which is also available in the multiphotonic platform developed under the framework of the European Project DIAGNOPTICS, after applying the same statistical calculations as those used in the multispectral imaging device. As the final goal of this project is to improve skin cancer diagnosis with the combination of four non-invasive novel techniques, we explore here the combination of the multispectral and 3D systems as a preliminary attempt of doing so.

### 6.1. 3D system results

From the 3D topography of each lesion measured with the 3D system available in the multiphotonic platform, different processing algorithms were developed to extract parameters which characterize the morphology of each lesion. Using C++, Matlab and Mountains Map software programs, the lesion was segmented and 9 parameters were obtained: mean height, maximum height, width, perimeter, area and volume; and the following ones based on first order statistics: energy, entropy and 3rd central moment of the height distribution. The maximum and mean of the height, the width and the perimeter were calculated from the mean profile of a series of horizontal profiles of the lesion. The area and the volume were calculated using four different methods: vertical lines, horizontal lines, least squares planes and polynomial surface (of degree 2 and 6). Making the median of the five values, a single value of the area and volume were assigned to the lesion. The last three parameters were obtained from the histogram of the height distribution (Figure 6.1).

In Figure 6.2 the topography of a nevus and a melanoma are shown. As it can be seen, the melanoma seems to be less homogenous in height and generally higher (more elevated) than the nevus.

Due to the difficulty of the lesion segmentation and processing to extract 3D information - the whole process lasted about 1 hour - only 57 nevi and 27 melanomas were available at the time of this report. Basal cell carcinomas were excluded because of the low amount of processed lesions. Furthermore, in order to be able to compare the results of the 3D system with those of the multispectral device, the lesions were also splitted into training and validation sets, taking into account the group in which they were previously classified in the multispectral classification algorithm. Regarding the lesions which were not used in the analysis of the multispectral system but were processed with the 3D system, they were included in the 3D training set. Accordingly, 27 nevi and 18 melanomas were finally included in the training set and 31 nevi and 9 melanomas in the validation set.

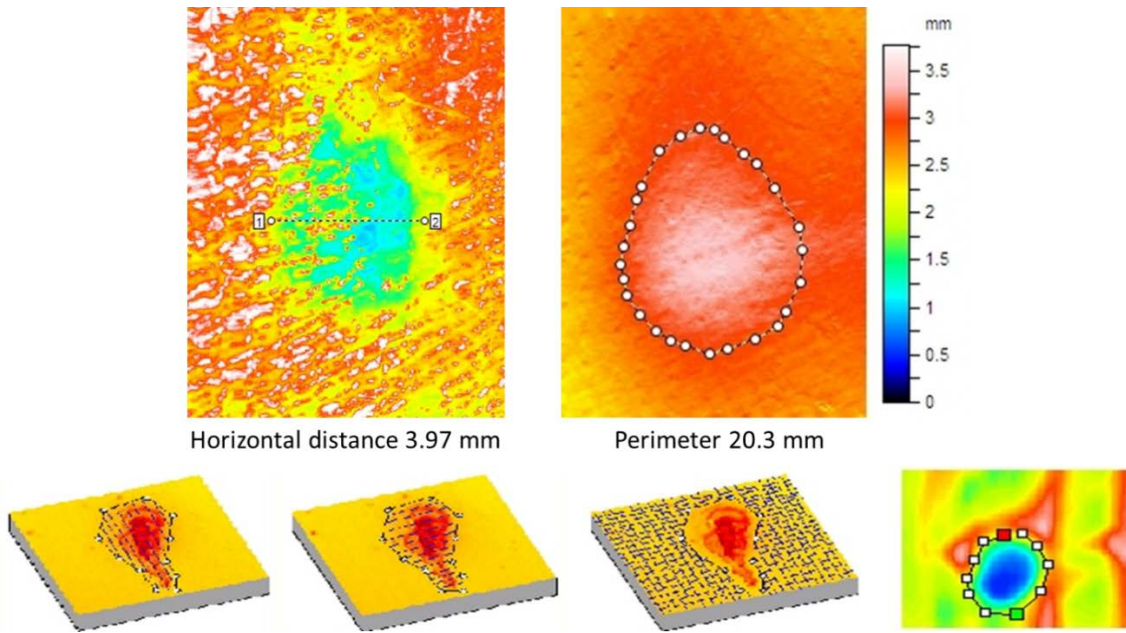


Figure 6.1 Horizontal width and perimeter of a lesion (top), and the 4 methods used to calculate the area and volume of any lesion (bottom).

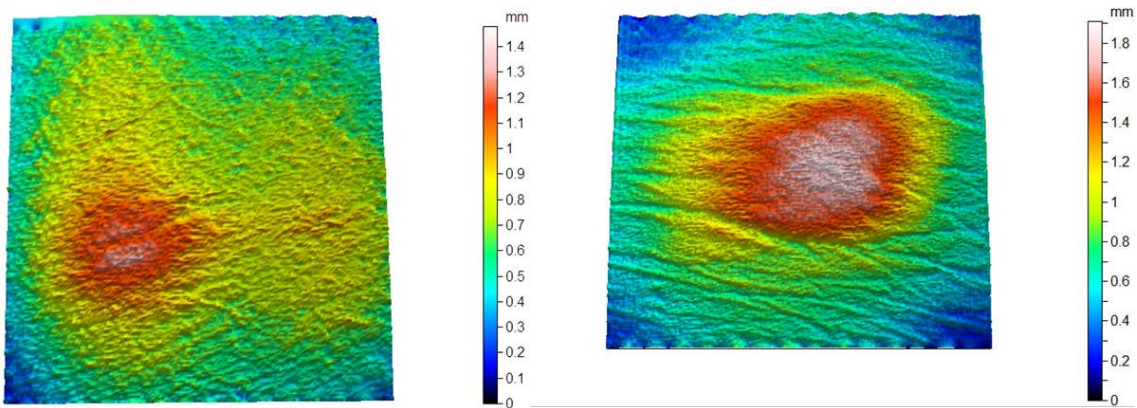


Figure 6.2 3D topography of a nevus (left) and a melanoma (right).

Similarly to the former chapter, thresholds linked to 3D data were chosen according to the following formula:

$$Nevi\ outliers = \tilde{x}_{nevi} \pm 2 \cdot \sigma_{nevi} \quad (6.1)$$

where  $\tilde{x}_{nevi}$  and  $\sigma_{nevi}$  are the average and standard deviation, respectively, in terms of each parameter based on 3D information calculated from all processed nevi lesions in the training set. All lesions above or under the upper and lower thresholds for at least one 3D parameter were classified as malignant.

The same iterative process used to choose non-redundant multispectral parameters was followed to select the most relevant 3D parameters in 3 steps: firstly, in order to detect the highest number of melanomas, the lesions in the validation set which were detected for only one parameter were found and this concrete parameter was selected. Secondly, the lesions which were detected for only two parameters were found and then, the parameter

which had the best rate of differentiation between nevi and melanoma was chosen. Finally, the same process was done successively with those lesions which were detected for 3, 4, 5... parameters, until the maximum number of melanomas were detected. The other parameters were discarded as they did not introduce any significant improvement in the detection of melanomas and basal cell carcinomas

By doing so, 3 of the 9 parameters firstly analysed were found to be not redundant and finally selected to be used in the validation set: perimeter, volume and maximum height (Figure 6.3), obtaining thus, 5 out 9 detected melanomas (55.6% sensitivity) and 5 out 31 nevi classified as malignant (83.7% specificity) (Table 6.1).

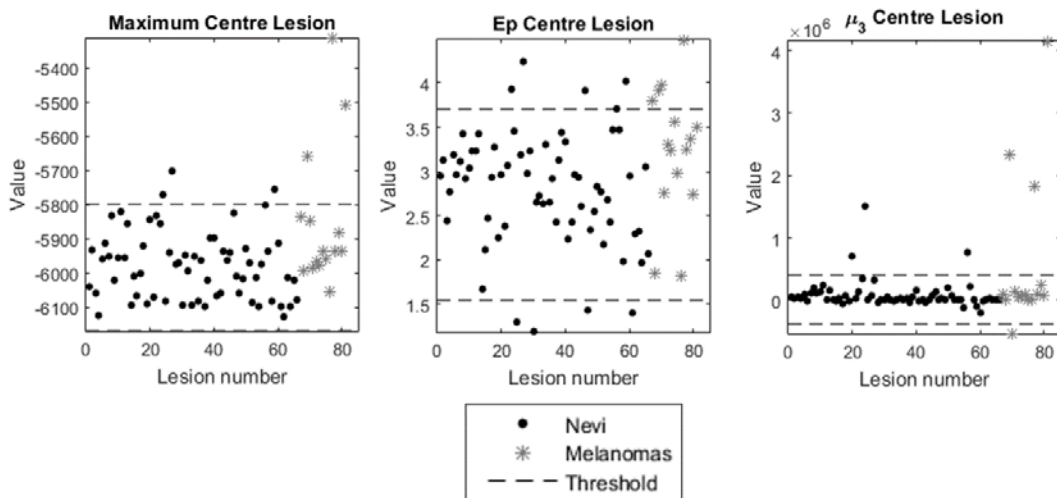


Figure 6.3 Scatterplots of the 3 selected parameters for the 3D system.

Table 6.1 Confusion matrix of the 3D system

Predicted condition	True condition		
	Total lesions: 40	Melanomas	Nevi
Melanomas		5	5
Nevi		4	26

Comparing the results with the multispectral system (87.2% and 54.5% of sensitivity and specificity, respectively) it is clear that the sensitivity based on 3D features is much lower (around 30%) although specificity is much better (about 30%, too). Therefore, even 3D information does not seem to allow detecting more melanomas it could be used to improve specificity of the results.

However, one should bear in mind that the amount of processed lesions with 3D technology is still very limited, and that the training set may not be the most representative one. So that the conclusions reached in this chapter must be taken with caution.

## 6.2. Combined results

The combination of the multispectral and 3D system has also been carried out in this thesis, despite the limited number of lesions analysed with 3D technology, as a preliminary attempt to improve the detection of melanomas, reselecting the best parameters which are not redundant and using the classification algorithm again.

However, in order to lately compare the results, only the common lesions available in both systems has been finally included in the analysis (21 melanomas and 54 nevi). Since the number was very limited, they were used as a whole, i. e., without splitting them into training and test sets.

In consequence, the recalculation of the individual multispectral and 3D sensitivity and specificity considering only these melanomas and nevi (76 lesions) was firstly needed. The process followed was on one hand, to obtain the sensitivity and specificity with the 15 parameters of the multispectral system; and on the other hand, repeating the process with the 3 parameters of the 3D system; and using in both cases the thresholds calculated in the previous sections (5.3 and 6.1). The sensitivity and specificity values were of 95.2% and 50%, respectively, for the multispectral system; and 66.7% and 88.9% for the 3D system.

Finally, all parameters (15 from the multispectral system and 3 from the 3D system) were considered together and, once again, an iterative process was used to choose non-redundant multispectral and 3D parameters as a whole in the 3 steps explained before. By doing so, only 6 parameters from both systems were employed to achieve the best possible classification: difference between the lesion and healthy skin in Ep of Refl<sub>465</sub>, maximum L\*, maximum ITA, maximum of Emp1, perimeter and maximum height.

This combination of parameters allowed a sensitivity of 100% and a specificity of 72.2%, thus improving the detection of melanomas (actually all them were detected) and the specificity (the values was in between those obtained by means of the two systems used individually) (Table 6.2). Nevertheless, it is necessary to take into account once again that the number of lesions included in this analysis is rather low, and that the conclusions reached must then be taken with caution and explored in the future in more detail.

Table 6.2 Sensitivity and specificity of each system individually (Multispectral and 3D) and when they are combined.

	<b>Multispectral</b>	<b>3D</b>	<b>Combined systems</b>
<b>Sensitivity</b>	95.2%	66.7%	100.0%
<b>Specificity</b>	50.0%	88.9%	72.2%

On the other hand, the analysis carried out also demonstrates that some of the melanomas have been classified as malignant using parameters from both systems simultaneously (10). While 10 melanomas were only detected by means of multispectral-based parameters and 1 with 3D ones. 40 nevi were found to be benign with both systems.

Therefore, a new classification could be suggested based on this:

- If both systems classify a lesion as malignant, there is a high probability of the lesion to be malignant.
- If only one of the systems classifies the lesion as malignant, it would have moderate possibilities to be malignant.
- If both systems classify the lesion as benign, this would be highly predictive of benignity.

However, and as formerly stated, more research on this field is still needed.



---

## 7. Conclusions

---

The most relevant conclusions obtained in this thesis are outlined here:

1. **Concerning the developed multispectral system:**

- a. A handheld ergonomic multispectral imaging system was developed as part of the multiphotonic platform in the European Project DIAGNOPTICS “Diagnosis of skin cancer using optics” (seventh call for proposals 2013, CIP-ICT-PSP.2013.3.5; GA621066) with the goal of improving skin cancer diagnosis with the combination of four non-invasive novel techniques: 3D and multispectral imaging, optical feedback interferometry and confocal microscopy.
- b. The system included a 12 bit-depth monochromatic CCD camera attached to an objective lens and a light source containing 32 LEDs (8 clusters) with 8 spectral bands covering the visible and the near-infrared range (400 nm to 1000 nm). The degree of polarization of light could also be changed with the use of two polarizers, enabling information from different skin depths to be obtained.
- c. An acquisition software to control all the components of the multispectral system was programmed. The extended version permitted to test the system in the laboratory, to adjust the exposure times needed to measure skin lesions as well as surrounding healthy skin of individuals within the dynamic range of each spectral band, and to perform the dark calibration to remove dark current noise due to straylight and non-uniformities of the pixels of the camera sensor. On the other hand, the user interface was a simpler version useful for physicians, in which only the measurements and the daily calibration (carried out by means of a uniform calibrated reference and needed to later compute the spectral reflectance of the skin lesion for each wavelength) were available.
- d. The changes over time of the emission of the LEDs was analysed by measuring the radiance corresponding to each wavelength at different forward currents. The analysis showed that LEDs needed at least 2 seconds to stabilize and therefore, a delay of two seconds each time that any LED was switched on was used in the algorithm. Three additional characteristics were also measured to ensure the good performance of the multispectral system as a whole: the linear response of the camera for each wavelength, the uniformity of the LEDs emission (which was below 3.5%) and the short and long-term repeatability of the system acquiring images (with variations reported of 0.5% and 2%, respectively).

## 7. CONCLUSIONS

---

- e. In order to proceed with the Ethical Committee approval and to launch the systems in both hospitals, irradiance and radiance measurements were done according to the standard UNE-EN 62471 “Photobiological safety of lamps and lamp systems”, to ensure that the multispectral system provided light emissions under the limits established by this regulation and to guarantee that patients could not be accidentally damaged under any circumstance.

### 2. Image processing and analysis:

- a. A GUI programmed in Matlab® R2015a was developed for the spectral image processing and corresponding analysis. Firstly, a software devoted to compute spectral and colorimetric features from the spectral images (spectral datacube) acquired with the multispectral system was implemented, including also the segmentation algorithm based on the Otsu method used to extract the isolated information of the lesion. From the spectral images acquired, the algorithm allowed reflectance images to be computed as well as images in terms of absorbance and differences between the average of a ROI of healthy surrounding skin with the lesion itself (spectral parameters). Additionally, images based on a second group of colour based parameters such as pseudoCIELAB colour coordinates, ITA, GFC, etc. were also calculated. Finally, another software used to operate with the spectral images to compute a third group of parameters called empirical to enhance any particular spectral feature potentially different in healthy and malignant tissue was also developed.
- b. For all images in terms of any of the parameters formerly described, statistical descriptors were obtained for each segmented lesion such as the mean, standard deviation, maximum and minimum. Also, as a first approach to the extraction of textural information, we used the analysis of the statistical properties of the histogram for any of the parameters calculated, also known as first order statistics, such as entropy, energy and third central moment.

### 3. Results:

- a. Inclusion criteria and a measurement protocol were established before conducting a clinical study in two hospitals (Barcelona and Modena).
- b. From all the lesions analysed in both hospitals, 620 were measured with the multispectral system. 572 of them had a clinical or histopathological diagnosis at the time of this report and 502 lesions were properly segmented with the algorithm implemented. The diagnosis of them were the following: 290 (57.9%) corresponded to nevi (melanocytic, dysplastic, blue, junctional and Spitz nevi); 95 (18.9%) were melanomas, 44 (8.9%) basal cell carcinomas; 35 (7%) seborrheic keratosis; 34 (6.9%) other benign lesions, such as angiomas, dermatofibromas and actinic keratosis; and 2 (0.4%) corresponded to squamous carcinomas. The last three types of lesions were excluded from the posterior analysis due to the low number



of samples available in each category. Therefore, 429 skin lesions were finally included in the study: nevi, melanomas and basal cell carcinomas.

- c. A classification algorithm was developed to decide whether the lesions were malignant (melanomas and basal cell carcinomas) or not (nevi). Data was splitted into training and validation sets of the same size including half of the nevi, basal cell carcinomas and melanomas. Using the training set, upper and lower thresholds were firstly defined for each parameter of the three groups previously described (spectral, colour and empirical) as the interval limits that included all nevi. All lesions above or under the upper and lower thresholds for at least one parameter were classified as malignant.
- d. Taking into account the difficulty of working with 1309 parameters, an algorithm in order to select only the most useful ones was implemented. This was achieved in 3 steps: firstly, in order to detect the highest number of melanomas and basal cell carcinomas, the lesions in the validation set which were detected for only one parameter were found and this concrete parameter was selected. Secondly, the lesions which were detected for only two parameters were found and then, the parameter which had the best rate of differentiation between nevi and melanoma/basal cell carcinoma were chosen. Finally, the same process was done successively with those lesions which were detected for 3, 4, 5... parameters, until the maximum number of melanomas were detected.
- e. From all parameters calculated, only 15 were not redundant and finally selected for use in the classification algorithm. From the first group (spectral reflectance and absorbance parameters; and corresponding differences between the lesion and the surrounding healthy skin):  $En$  of  $Abs_{875}$ ,  $\mu_3$  of  $Refl_{745}$ ,  $\tilde{\alpha}$  of  $Refl_{645}$  and  $\sigma$  of  $Abs_{935}$ . Also, differences between lesion and surrounding skin in terms  $Ep$  of  $Abs_{465}$ ,  $En$  of  $Abs_{635}$ ,  $\mu_3$  of  $Abs_{985}$ , and  $\mu_3$  of  $Refl_{975}$ . From the second group (colour-based parameters): maximum of  $L^*$ ,  $\sigma$  of  $a^*$  as pseudo-CIELAB colorimetric coordinates, and minimum  $\Delta E$  with the surrounding healthy skin as the reference, and maximum ITA. From the third group (empirical parameters): maximum of  $Emp1$ ,  $En$  of  $Emp6$ , maximum of  $Emp9$ .
- f. With the classification algorithm based on these 15 parameters, 6 out of 47 melanomas and none of the 22 basal cell carcinomas were misclassified (91.3% sensitivity); in contrast, 66 nevi from 145 were classified as malignant (54.5% specificity). The addition of textural information was shown to be useful for the diagnostic of malignant lesions (melanomas and basal cell carcinomas) than the sole use of averaged spectral and colour information. The sensitivity (91.3%) and specificity (54.5%) values slightly improved in some cases those previously achieved by means of other multispectral systems without the need of an experienced dermatologist as it was based on a complete automatic algorithm.

- g. When only the melanomas and nevi were considered the sensitivity decreased down to 87.2%, although this value was still similar to that obtained by experienced dermatologists through averaged spectral and colour features.

#### 4. **Combination of the multispectral system with the 3D system:**

- a. The same steps previously carried out for the multispectral system were done for the 3D system, splitting all lesions into training and validation sets and using a classification algorithm to find the best parameters. 57 nevi and 27 melanomas were included in the analysis. The perimeter, volume and maximum height were the parameters found to be relevant in this case, obtaining values of 55.6% and 83.7% for sensitivity and specificity, respectively.
- b. The combination of the multispectral and 3D system was also carried out as a first attempt to improve the detection of melanomas through the combination of different optical technologies available in the multiphotonic platform. In this case, only the lesions simultaneously analysed with both technologies (multispectral and 3D) were used (54 nevi and 21 melanomas), and lesions were not splitted into training and test sets due to the limited number of samples available. 6 parameters were found to be relevant in this case providing a 100% of sensitivity and 72.2% of specificity: difference between the lesion and healthy skin in Ep of Refl<sub>465</sub>, maximum L\*, maximum ITA, maximum of Emp1, perimeter and maximum height. However, the conclusions reached in this case should be taken with caution due to the limited number of lesions included in the analysis.

---

## 8. Future work

---

In this chapter, some research lines are suggested for future work related to this thesis:

**1. Concerning the developed multispectral system:**

- a. The use of the spectral images at  $45^\circ$  and  $0^\circ$  would be useful for the extraction of more information about the lesion's skin behaviour at different wavelengths.
- b. Daily calibration could be reduced to weekly calibration after checking the repeatability of the system with the daily calibration spectral images, in order to facilitate the use of the system to physicians.

**2. Concerning the spectral and colorimetric analysis:**

- a. The inclusion of more melanomas and basal cell carcinomas in the validation set, could ensure the selected parameters.
- b. The measurement of more seborrheic keratosis, basal cell carcinomas and other kinds of benign and malignant lesions would allow the improvement of the classification algorithm, in order to enhance the detection of malignant lesions.
- c. Second order statistics, i.e. co-occurrence matrices, could improve the textural analysis of the lesion, due to it takes into account the spatial relationship among digital levels.
- d. A deeper analysis using machine learning, i.e. principal components analysis (PCA), could be used to reduce the large list of parameters, and to find more suitable thresholds to classify the lesions.

**3. Concerning the inclusion of the OFI and 3D systems:**

- a. More 3D lesions which have been also analysed with the multispectral system should be included to verify the parameters selected for the 3D. Furthermore, more accurate sensitivity and specificity could be obtained with the combination of the 3D and multispectral system.
- b. Analysis of the OFI information, in order to find parameters which could improve the detection of malignant lesions with the combination of the 3D and multispectral system.



---

## 9. Dissemination

---

### 9.1. Journal publications

1. Delpueyo X., Ares M., Vilaseca M., Royo S., Sanabria F., Herrera J., Hincapié-Zuluaga D., Puig S., Pellacani G., Vázquez J., Solomita G., Bosch T, “Mejora del diagnóstico del cáncer de piel a través de sistemas ópticos”. E-medida, Revista Española de Metrología, 2016. Online Publication.
2. Delpueyo X., Vilaseca M., Royo S., Ares M., Rey-Barroso L., Sanabria F., Puig S., Malveyh J., Pellacani G., Vázquez J., Solomita G., Bosch T (2017): “Multispectral imaging system based on light emitting diodes for the detection of melanomas and basal cell carcinomas: a pilot study”, Journal of Biomedical Optics, 2017, 22(6), 065006. [doi: 10.1117/1.JBO.22.6.065006].

### 9.2. Congress proceedings

1. Ares, M., Royo, S., Vilaseca, M., Herrera, Jorge A., Delpueyo, X., Sanabria, F. (2014): "Handheld 3D Scanning System for In-Vivo Imaging of Skin Cancer". 5th International Conference on 3D Body Scanning Technologies, Lugano, Switzerland, 21-22, 2014. Proceedings 231-236.
2. Delpueyo, X., Vilaseca, M., Royo, S., Ares, M., Sanabria, F., Herrera, J., Burgos, F.J., Pujol, J., Puig, S., Pellacani, G., Vázquez, J., Solomita G. and Bosch, T. (2015): "Handheld Hyperspectral Imaging System for the Detection of Skin Cancer". AIC 2015, Tokyo, Japan. Proceedings. 385-390.
3. Royo, S., Ares, M., Riu, J., Atashkooei, R., Vilaseca, M., Delpueyo, X., Azcona, F., Jha, A., Yáñez, C. (2015): "Metrología óptica en el CD6: aplicaciones en imagen láser". XI Reunión Nacional de Óptica Día de la Luz, 2015, Salamanca, Spain. Proceedings.
4. Delpueyo X., Ares M., Vilaseca M., Royo S., Sanabria F., Herrera J., Burgos F.J., Pujol J., Puig S., Pellacani G., Vázquez J., Solomita G., Bosch T. (2015): "Proyecto DIAGNOPTICS: Diagnóstico del cáncer de piel utilizando óptica". XI Reunión Nacional de Óptica Día de la Luz, 2015, Salamanca, Spain. Proceedings. ISBN 978-84-608-4609-3.
5. Delpueyo, X., Vilaseca, M., Royo, S., Ares, M., Sanabria, F., Herrera, J., Pujol, J., Puig, S., Pellacani, G., Vázquez, J., Solomita G. and Bosch, T. (2016): "Sistema

multispectral para el diagnóstico del cáncer de piel, 2016, Ourense, Spain". XI Congreso Nacional del Color. Proceedings.

6. Delpueyo, X., Vilaseca, M., Royo, S., Ares, M., Sanabria, F., Herrera, J., Pujol, J., Puig, S., Pellacani, G., Vázquez, J., Solomita G. and Bosch, T: "Combination of a multispectral and 3D imaging sensors for the detection of skin cancer". In the 5th International Symposium on Sensor Science 2017. Proceedings. [Submitted].

### 9.3. Patent

Title: Computer implemented method, a system and computer program products to characterize a skin lesion.

Public inventors: Delpueyo, X., Vilaseca M., Ares M., Royo S., Vázquez, J., Pellacani, G., Andre P., Solomita G., Bassoli S., Malvehy, J., Puig, S., Perchoux J., Quotb A.

Application number: EP17152349

Country: European Union

Applicant: Universitat Politècnica de Catalunya (UPC)

---

## 10. Bibliography

---

- [1] I. Kuzmina *et al.*, “Towards noncontact skin melanoma selection by multispectral imaging analysis,” *J. Biomed. Opt.*, vol. 16, no. 6, p. 60502, 2011.
- [2] M. Elbaum *et al.*, “Automatic differentiation of melanoma from melanocytic nevi with multispectral digital dermoscopy: A feasibility study,” *J. Am. Acad. Dermatol.*, vol. 44, no. 2, pp. 207–218, 2001.
- [3] “DermLite DL100,” *DermLite*. [Online]. Available: <https://dermlite.com/>. [Accessed: 19-Jun-2017].
- [4] R. P. Braun, H. S. Rabinovitz, M. Oliviero, A. W. Kopf, and J. H. Saurat, “Dermoscopy of pigmented skin lesions,” *J. Am. Acad. Dermatol.*, vol. 52, no. 1, pp. 109–121, 2005.
- [5] A. Gadeliya Goodson and D. Grossman, “Strategies for early melanoma detection: Approaches to the patient with nevi,” *J. Am. Acad. Dermatol.*, vol. 60, no. 5, pp. 719–735, 2009.
- [6] American Cancer Society, “Cancer Facts & Figures 2017,” 2017.
- [7] G. P. Guy, S. R. Machlin, D. U. Ekwueme, and K. R. Yabroff, “Prevalence and costs of skin cancer treatment in the U.S., 2002-2006 and 2007-2011,” *Am. J. Prev. Med.*, vol. 48, no. 2, pp. 183–187, 2015.
- [8] Y. Garini, I. T. Young, and G. McNamara, “Spectral imaging: principles and applications,” *Cytometry. A*, vol. 69, no. 8, pp. 735–747, Aug. 2006.
- [9] G. Zhou, K. K. L. Cheo, Y. Du, F. S. Chau, H. Feng, and Q. Zhang, “Hyperspectral imaging using a microelectrical-mechanical-systems-based in-plane vibratory grating scanner with a single photodetector,” *Opt. Lett.*, vol. 34, no. 6, pp. 764–766, 2009.
- [10] M. Gianinetto and G. Lechi, “The development of superspectral approaches for the improvement of land cover classification,” *IEEE Trans. Geosci. Remote Sens.*, vol. 42, no. 11, pp. 2670–2679, 2004.
- [11] H. R. Kang, *Computational Color Technology*, 1st ed. SPIE Press Book, 2006.
- [12] C. Chang, *Hyperspectral data exploitation: theory and applications*, 1st ed. USA: Jhon Wiley & Sons, 2001.
- [13] F. Imai and R. Berns, “Spectral estimation using trichromatic digital cameras,” in *Conference on International Symposium on Multispectral Imaging and Color*

- Reproduction for Digital Archives*, 1999, pp. 42–49.
- [14] M. Govender, K. Chetty, and H. Bulcock, “A review of hyperspectral remote sensing and its application in vegetation and water resource studies,” *Water SA*, vol. 33, no. 2, pp. 145–151, 2007.
- [15] L. T. Nieman, M. B. Sinclair, J. A. Timlin, H. D. T. Jones, and D. M. Haaland, “Hyperspectral Imaging System for Quantitative Identification and Discrimination of Fluorescent Labels in the Presence of Autofluorescence,” *3rd IEEE Int. Symp. Biomed. Imaging Macro to Nano, 2006.*, pp. 1288–1291, 2006.
- [16] A. A. Gowen, C. P. O’Donnell, P. J. Cullen, G. Downey, and J. M. Frias, “Hyperspectral imaging - an emerging process analytical tool for food quality and safety control,” *Trends Food Sci. Technol.*, vol. 18, no. 12, pp. 590–598, 2007.
- [17] A. Plaza and J. Plaza, “Impact of Vector Ordering Strategies on Morphological Unmixing of Remotely Sensed Hyperspectral Images,” in *ICPR. 20th International Conference on Pattern Recognition*, 2010, pp. 4412–4415.
- [18] G. J. Edelman, E. Gaston, T. G. van Leeuwen, P. J. Cullen, and M. C. G. Aalders, “Hyperspectral imaging for non-contact analysis of forensic traces,” *Forensic Sci. Int.*, vol. 223, no. 1–3, pp. 28–39, 2012.
- [19] J. Plaza, A. J. Plaza, and C. Barra, “Multi-channel morphological profiles for classification of hyperspectral images using support vector machines,” *Sensors*, vol. 9, no. 1, pp. 196–218, 2009.
- [20] H. F. Grahn and P. Geladi, *Techniques and Applications of Hyperspectral Image Analysis*, vol. 22, no. 7. 2007.
- [21] F. Vasefi, N. MacKinnon, and D. . Farkas, “Hyperspectral and multispectral imaging in dermatology,” in *Imaging in Dermatology*, 1st ed., Elsevier Inc., 2016, pp. 187–201.
- [22] X. Cao *et al.*, “Computational Snapshot Multispectral Cameras,” *IEE Signal Processing Magazine*, no. 1053–588/16, pp. 95–108, 2016.
- [23] C. Fischer and I. Kakoulli, “Multispectral and hyperspectral imaging technologies in conservation: current research and potential applications,” *Rev. Conserv.*, vol. 7, no. 7, pp. 3–16, 2006.
- [24] C. Balas, “Review of biomedical optical imaging—a powerful, non-invasive, non-ionizing technology for improving in vivo diagnosis,” *Meas. Sci. Technol.*, vol. 20, no. 10, p. 104020, 2009.
- [25] “VariSpec™ Liquid Crystal Tunable Filters,” *Perkin Elmer*. [Online]. Available: <https://www.perkinelmer.com>. [Accessed: 19-Jun-2017].
- [26] “AOTF 2837-31,” *Gooch & Housego*. [Online]. Available: <https://goochandhousego.com>.



- [27] “FW1ADF Filter Wheel,” *Thorlabs*. [Online]. Available: <https://www.thorlabs.com>. [Accessed: 19-Jun-2017].
- [28] W. Cho, J. Jang, A. Koschan, M. A. Abidi, and J. Paik, “Hyperspectral face recognition using improved inter-channel alignment based on qualitative prediction models,” *Opt. Express*, vol. 24, no. 24, pp. 27637–27662, 2016.
- [29] R. W. Slawson, Z. Ninkov, and E. P. Horch, “Hyperspectral Imaging : Wide-Area Spectrophotometry Using a Liquid-Crystal Tunable Filter,” *Astron. Soc. Pacific*, vol. 111, pp. 621–626, 1999.
- [30] A. Del Bianco, G. Serafino, and G. Spöck, “An introduction to spectral imaging,” *Useful Adv. Inf. F. Near Infrared Spectrosc.*, pp. 1–36, 2003.
- [31] H. Liang, “Advances in multispectral and hyperspectral imaging for archaeology and art conservation,” *Appl. Phys. A Mater. Sci. Process.*, vol. 106, no. 2, pp. 309–323, 2011.
- [32] “Crystalline Quartz Collinear AOTF Configuration,” *Olympus*. [Online]. Available: <http://www.olympusmicro.com>. [Accessed: 19-Jun-2017].
- [33] M. Ben-Ezra, J. Wang, B. Wilburn, X. Li, and L. Ma, “An LED-only BRDF measurement device,” *26th IEEE Conf. Comput. Vis. Pattern Recognition, CVPR*, no. i, 2008.
- [34] P. Mottier, *LEDs for Lightning Applications*, 1st ed. France: John Wiley & Sons, Inc, 2009.
- [35] Ó. Martínez, M. Vilaseca, M. Arjona, C. Pizarro, and J. Pujol, “Use of light-emitting diodes in multispectral systems design: Variability of spectral power distribution according to angle and time of usage,” in *IX Congreso Nacional del Color*, 2010, vol. 55, no. 5, p. 50501.
- [36] G. Healey and R. Kondepudy, “Radiometric CCD camera calibration and noise estimation,” *Pattern Anal. Mach. Intell.*, vol. 16, no. 3, pp. 267–276, 1994.
- [37] D. Litwiller, “CCD vs. CMOS,” *Photonics Spectra*, vol. 35, no. 1, pp. 154–158, 2001.
- [38] G. C. Holst and T. S. Lomheim, *CMOS/CCD Sensors and Camera System*, 1st ed. USA: JCD Publishing, 2007.
- [39] J. Janesick, *Scientific Charged-Coupled Devices*, 1st ed. SPIE Publications, 2001.
- [40] D. Litwiller, “CMOS vs. CCD: Maturing Technologies, Maturing Markets,” *Photonics Spectra*, vol. 39, no. 8, pp. 54–61, 2005.
- [41] H. Beyer, “Accurate calibration of CCD-cameras,” in *Proceedings CVPR’92. Conference on Computer Vision and Pattern Recognition. IEEE Computer Society.*, 1992, pp. 96–101.
- [42] H. Othman, “Noise reduction of hyperspectral imagery using hybrid spatial-

- spectral derivative-domain wavelet shrinkage,” *IEEE Trans. Geosci. Remote Sens.*, vol. 44, no. 2, pp. 397–408, 2006.
- [43] M. de Lasarte, J. Pujol, M. Arjona, and M. Vilaseca, “Optimized algorithm for the spatial nonuniformity correction of an imaging system based on a charge-coupled device color camera.,” *Appl. Opt.*, vol. 46, no. 2, pp. 167–74, 2007.
- [44] R. C. Hardie, M. M. Hayat, E. Armstrong, and B. Yasuda, “Scene-based nonuniformity correction with video sequences and registration.,” *Appl. Opt.*, vol. 39, no. 8, pp. 1241–50, 2000.
- [45] M. M. Hayat, S. N. Torres, E. Armstrong, S. C. Cain, and B. Yasuda, “Statistical algorithm for nonuniformity correction in focal-plane arrays.,” *Appl. Opt.*, vol. 38, pp. 772–780, 1999.
- [46] B. M. Ratliff, M. M. Hayat, and R. C. Hardie, “correction in focal-plane arrays,” vol. 19, no. 9, pp. 1737–1747, 2002.
- [47] R. S. Aikens, D. a Agard, and J. W. Sedat, “Solid-state imagers for microscopy.,” *Methods in cell biology*, vol. 29. pp. 291–313, 1989.
- [48] L. J. Van Vliet, F. R. Boddeke, D. Sudar, and I. T. Young, “Image Detectors for Digital Image Microscopy,” *Digit. Image Anal. Microbes; Imaging, Morphometry, Fluorometry Motil. Tech. Appl.*, pp. 1–25, 1998.
- [49] C. J. Marshall, P. W. Marshall, A. Waczynski, E. J. Polidan, and S. D. Johnson, “Hot pixel annealing behavior in CCDs irradiated at -84°C,” *Nucl. Sci.*, vol. 52, no. 6, pp. 2672–2677, Dec. 2005.
- [50] J. Dudas, C. Jung, M. L. La Haye, and G. H. Chapman, “A fault-tolerant active pixel sensor for mitigating hot pixel defects,” *Can. Conf. Electr. Comput. Eng.*, pp. 1447–1448, 2007.
- [51] J. Dudas, M. L. La Haye, J. Leung, and G. H. Chapman, “A fault-tolerant active pixel sensor to correct in-field hot-pixel defects,” *Proc. - IEEE Int. Symp. Defect Fault Toler. VLSI Syst.*, pp. 517–525, 2007.
- [52] M. S. Kim, Y. R. Chen, and P. M. Mehl, “Hypersectral Reflectance and Fluorescence Imaging System for Food Quality and Safety,” *Trans. ASAE*, vol. 44, no. 3, pp. 721–729, 2001.
- [53] M. Vilaseca *et al.*, “Repeatability, reproducibility, and accuracy of a novel pushbroom hyperspectral system,” *Color Res. Appl.*, p. Online Publication, Oct. 2013.
- [54] P. Capilla, J. Artigas, and J. Pujol, *Fundamentos de colorimetria*, 1st ed. Saragossa: Universitat de València, 2002.
- [55] P. Ganesan, V. Rajini, and R. I. Rajkumar, “Segmentation and edge detection of color images using CIELAB Color Space and Edge detectors,” *Int. Conf. "Emerging Trends Robot. Commun. Technol. INTERACT-2010*, pp. 393–397,

2010.

- [56] B. Hill, T. Roger, and F. W. Vorhagen, “Comparative analysis of the quantization of color spaces on the basis of the CIELAB color-difference formula,” *ACM Trans. Graph.*, vol. 16, no. 2, pp. 109–154, 1997.
- [57] S. Tominaga, “A color classification method for color images using a uniform color space,” *Pattern Recognition, 1990. Proceedings., 10th ...*, pp. 803–807, 1990.
- [58] J. E. Agudo, P. J. Pardo, H. Sánchez, Á. L. Pérez, and M. I. Suero, “A Low-Cost Real Color Picker Based on Arduino,” *Sensors*, vol. 44, pp. 11943–11956, 2014.
- [59] “CIE L\*C\*h Color Space,” *Konika Minolta*. [Online]. Available: <http://sensing.konicaminolta.us>. [Accessed: 19-Jun-2017].
- [60] F. Imai, “Comparison of Spectrally Narrow Band Capture vs WideBand with A Piror Sample Analysis for Sepctral Reflectance Estimation,” *IS{E}TD Eight Color Imaigng Conferecen*, pp. 231–234, 2000.
- [61] F. Imai, M. Rosen, and R. Berns, “Comparative study of metrics for spectral match quality,” in *CGIV 2002: The First European Conference on Colour Graphics, Imaging and Vision*, 2002, pp. 495–499.
- [62] M. Assefa, “Kubelka-Munk theory for efficient spectral printer modeling,” Gjøvik University College, Norway, 2010.
- [63] J. Hernández-Andrés, J. Romero, and R. L. Lee, “Colorimetric and spectroradiometric characteristics of narrow-field-of-view clear skylight in Granada, Spain.,” *J. Opt. Soc. Am. A. Opt. Image Sci. Vis.*, vol. 18, no. 2, pp. 412–20, 2001.
- [64] M. R. Luo, G. Cui, and B. Rigg, “The development of the CIE 2000 colour-difference formula: CIEDE2000,” *Color Res. Appl.*, vol. 26, no. 5, pp. 340–350, 2001.
- [65] S. Geol Lee, R. Shamey, D. Hinks, and W. Jasper, “Development of a comprehensive visual dataset based on a CIE blue color center: Assessment of color difference formulae using various statistical methods,” *Color Res. Appl.*, vol. 36, no. 1, pp. 27–41, 2011.
- [66] G. Sharma, W. Wu, and E. N. Dalal, “The CIEDE2000 color-difference formula: Implementation notes, supplementary test data, and mathematical observations,” *Color Res. Appl.*, vol. 30, no. 1, pp. 21–30, 2005.
- [67] S. Del Bino and F. Bernerd, “Variations in skin colour and the biological consequences of ultraviolet radiation exposure,” *Br. J. Dermatol.*, vol. 169, no. SUPPL. 3, pp. 33–40, 2013.
- [68] R. Haralick, K. Shanmugan, and I. Dinstein, “Textural features for image classification,” *IEEE Transactions on Systems, Man and Cybernetics*, vol. 3, pp. 610–621, 1973.

- [69] R. C. Gonzalez and R. E. Woods, *Digital image processing*, 2nd ed. New Jersey: Prentice-Hall, 2002.
- [70] J. A. Herrera, M. Vilaseca, J. Düll, M. Arjona, E. Torrecilla, and J. Pujol, "Iris color and texture: A comparative analysis of real irises, ocular prostheses, and colored contact lenses," *Color Res. Appl.*, vol. 36, no. 5, pp. 373–382, 2011.
- [71] G. X. Ritter and J. N. Wilson, *Handbook of computer vision algorithms in image algebra*. 2001.
- [72] S. N. Torres, J. E. Pezoa, and M. M. Hayat, "Scene-based nonuniformity correction for focal plane arrays by the method of the inverse covariance form.," *Appl. Opt.*, vol. 42, no. 29, pp. 5872–81, 2003.
- [73] N. Aggarwal and R. K. Agrawal, "First and Second Order Statistics Features for Classification of Magnetic Resonance Brain Images," *J. Signal Inf. Process.*, vol. 3, no. 2, pp. 146–153, 2012.
- [74] R. N. Clark, G. A. Swayze, E. K. Livo, R. F. Kokaly, and S. J. Sutley, "Imaging spectroscopy: Earth and planetary remote sensing with the USGS Tetracorder and expert systems," *J. Geophys. Res.*, vol. 108, no. E12, p. 5131, 2003.
- [75] F. Montmessin *et al.*, "Hyperspectral imaging of convective CO<sub>2</sub> ice clouds in the equatorial mesosphere of Mars," *Geophys. Res.*, vol. 112, no. E11, pp. 1–14, 2007.
- [76] P. Weibring *et al.*, "Fluorescence lidar imaging of historical monuments.," *Appl. Opt.*, vol. 40, no. 33, pp. 6111–6120, 2001.
- [77] X. Delpueyo, M. Vilaseca, M. Furió, F. J. Burgos-Fernández, and J. Pujol, "Multispectral and colour imaging systems for the detection of small vertebrate fossils : A preliminary study," *Palaeontol. Electron.*, vol. 19.3.5T, pp. 1–9, 2016.
- [78] D. P. Ariana, R. Lu, and D. E. Guyer, "Near-infrared hyperspectral reflectance imaging for detection of bruises on pickling cucumbers," *Comput. Electron. Agric.*, vol. 53, no. 1, pp. 60–70, 2006.
- [79] J. Gómez-Sanchis *et al.*, "Hyperspectral system for early detection of rotteness caused by *Penicillium digitatum* in mandarins," *J. Food Eng.*, vol. 89, no. 1, pp. 80–86, 2008.
- [80] J. Qin and R. Lu, "Measurement of the optical properties of fruits and vegetables using spatially resolved hyperspectral diffuse reflectance imaging technique," *Postharvest Biol. Technol.*, vol. 49, no. 3, pp. 355–365, 2008.
- [81] G. K. Naganathan, L. M. Grimes, J. Subbiah, C. R. Calkins, A. Samal, and G. E. Meyer, "Visible/near-infrared hyperspectral imaging for beef tenderness prediction," *Comput. Electron. Agric.*, vol. 64, no. 2, pp. 225–233, 2008.
- [82] D. Y. Jia and T. H. Ding, "Detection of foreign materials in cotton using a multi-wavelength imaging method," *Meas. Sci. Technol.*, vol. 16, no. 6, p. 1355, 2005.

- [83] C. R. Mora, L. R. Schimleck, S. C. Yoon, and C. N. Thai, "Determination of basic density and moisture content of loblolly pine wood disks using a near infrared hyperspectral imaging system," *J. Near Infrared Spectrosc.*, vol. 19, no. 5, pp. 401–409, 2011.
- [84] S. Serranti and G. Bonifazi, "Hyperspectral imaging based recognition procedures in particulate solid waste recycling," *World Rev. Sci. Technol. Sustain. Dev.*, vol. 7, no. 3, pp. 271–281, 2010.
- [85] M. S. Kim, Y. R. Chen, and P. M. Mehl, "Hyperspectral reflectance and fluorescence imaging system for food quality and safety," vol. 44, no. 3, pp. 721–729, 2001.
- [86] R. A. Schultz, T. Nielsen, J. R. Zavaleta, R. Ruch, R. Wyatt, and H. R. Garner, "Hyperspectral imaging: a novel approach for microscopic analysis," *Cytometry*, vol. 43, no. 4, pp. 239–247, 2001.
- [87] F. Meriaudeau, V. Paquit, N. Walter, J. Price, and K. Tobin, "3D and multispectral imaging for subcutaneous veins detection," *Proc. - Int. Conf. Image Process. ICIP*, vol. 17, no. 14, pp. 2857–2860, 2009.
- [88] A. Basiri *et al.*, "Use of a multi-spectral camera in the characterization of skin wounds," *Opt. Express*, vol. 18, no. 4, p. 3244, 2010.
- [89] M. B. Bouchard, B. R. Chen, S. a Burgess, and E. M. C. Hillman, "Ultra-fast multispectral optical imaging of cortical oxygenation, blood flow, and intracellular calcium dynamics.," *Opt. Express*, vol. 17, no. 18, pp. 15670–15678, 2009.
- [90] N. L. Everdell, I. B. Styles, A. Calcagni, J. Gibson, J. Hebden, and E. Claridge, "Multispectral imaging of the ocular fundus using light emitting diode illumination," *Rev. Sci. Instrum.*, vol. 81, no. 9, pp. 1–9, 2010.
- [91] L. Gao, R. T. Smith, and T. S. Tkaczyk, "Snapshot hyperspectral retinal camera with the Image Mapping Spectrometer (IMS)," *Biomed. Opt. Express*, vol. 3, no. 1, p. 48, 2012.
- [92] B. Khoobehi, J. M. Beach, and H. Kawano, "Hyperspectral Imaging for Measurement of Oxygen Saturation in the Optic Nerve Head," *Invest. Ophthalmol. Vis. Sci.*, vol. 45, no. 5, pp. 1464–72, 2004.
- [93] Z. Liu, Q. Li, J. Yan, and Q. Tang, "A novel hyperspectral medical sensor for tongue diagnosis," *Sens. Rev.*, vol. 27, no. 1, pp. 57–60, 2007.
- [94] N. Guo, L. Zeng, and Q. Wu, "A method based on multispectral imaging technique for White Blood Cell segmentation," *Comput. Biol. Med.*, vol. 37, no. 1, pp. 70–76, 2007.
- [95] H. Akbari *et al.*, "Hyperspectral imaging and quantitative analysis for prostate cancer detection.," *J. Biomed. Opt.*, vol. 17, no. 7, p. 76005, 2012.
- [96] N. Thekkekk and R. Richards-Kortum, "Optical imaging for cervical cancer

- detection: solutions for a continuing global problem,” *Nat. Rev. Cancer*, vol. 8, pp. 725–731, 2008.
- [97] S. Kiyotoki *et al.*, “New method for detection of gastric cancer by hyperspectral imaging: a pilot study.,” *J. Biomed. Opt.*, vol. 18, no. 2, p. 26010, 2013.
- [98] F. M. Walter *et al.*, “Effect of adding a diagnostic aid to best practice to manage suspicious pigmented lesions in primary care: randomised controlled trial,” *BMJ*, vol. 345, p. e4110, 2012.
- [99] T. Ohtsuki and G. Healey, “Using Color and Geometric Models for Extracting Facial Features,” *J. Imaging Sci. Technol.*, vol. 42, no. 6, pp. 554–561, 1998.
- [100] D. Pishva, “Use of Spectral Biometrics for Aliveness Detection,” *Adv. Biometrics Technol.*, 2009.
- [101] G. B. G. Altshuler and I. Yaroslavsky, “Absorption Characteristics of Tissues as a Basis for the Optimal Wavelength Choice in Photodermatology,” *Palomar Med. Technol. Burlingt.*, p. 4, 2004.
- [102] G. N. Stamatias and N. Kollias, “Non - Invasive Measurements of Skin Pigmentation In Situ,” *Pigment cell Res.*, vol. 7, pp. 618–626, 2004.
- [103] I. Diebele *et al.*, “Clinical evaluation of melanomas and common nevi by spectral imaging.,” *Biomed. Opt. Express*, vol. 3, no. 3, pp. 467–472, 2012.
- [104] J. D. Emery, J. Hunter, P. N. Hall, A. J. Watson, M. Moncrieff, and F. M. Walter, “Accuracy of SIAscopy for pigmented skin lesions encountered in primary care: development and validation of a new diagnostic algorithm.,” *BMC Dermatol.*, vol. 10, p. 9, 2010.
- [105] G. Monheit *et al.*, “The performance of MelaFind: a prospective multicenter study.,” *Arch. Dermatol.*, vol. 147, no. 2, pp. 188–94, 2011.
- [106] E. Claridge, S. Cotton, M. Moncrieff, and P. Hall, “Spectrophotometric Intracutaneous Imaging (Siascopy): Method and Clinical Applications E.,” *Handb. Non-Invasive Methods Ski.*, pp. 315–325, 2006.
- [107] M. Moncrieff, S. Otton, E. Claridge, and P. Hall, “Spectrophotometric intracutaneous analysis: A new technique for imaging pigmented skin lesions,” *Br. J. Dermatol.*, vol. 146, no. 3, pp. 448–457, 2002.
- [108] A. Hauschild *et al.*, “To excise or not: impact of MelaFind on German dermatologists’ decisions to biopsy atypical lesions,” *JDDG J. der Dtsch. Dermatologischen Gesellschaft*, vol. 12, no. 7, pp. 606–614, 2014.
- [109] M. A. Haniffa, J. J. Lloyd, and C. M. Lawrence, “The use of a spectrophotometric intracutaneous analysis device in the real-time diagnosis of melanoma in the setting of a melanoma screening clinic,” *Br. J. Dermatol.*, vol. 156, no. 6, pp. 1350–1352, 2007.

- [110] A. Bekina, I. Diebele, U. Rubins, Z. Janis, A. Derjabo, and J. Spigulis, “Multispectral Assessment of Skin Malformations Using a Modified Video-Microscope,” *Latv. J. Phys. Technical Sci.*, vol. 49, pp. 4–8, 2012.
- [111] D. Kapsokalyvas *et al.*, “Spectral morphological analysis of skin lesions with a polarization multispectral dermoscope.,” *Opt. Express*, vol. 21, no. 4, pp. 4826–40, 2013.
- [112] “SIAScope V and MoleMate program,” *MedX*. [Online]. Available: <http://medxhealth.com>.
- [113] “MelaFind,” *MELA Science*. [Online]. Available: <http://skincancerinstitute.net/melafind/>.
- [114] M. A. Calin, S. V. Parasca, R. Savastru, M. R. Calin, and S. Dontu, “Optical techniques for the noninvasive diagnosis of skin cancer,” *J. Cancer Res. Clin. Oncol.*, vol. 139, no. 7, pp. 1083–1104, 2013.
- [115] A. F. Fercher, “Optical coherence tomography,” *J. Biomed. Opt.*, vol. 1, no. 2, pp. 157–173, 1996.
- [116] L. Brancaleon, A. J. Durkin, J. H. Tu, G. Menaker, J. D. Fallon, and N. Kollias, “In vivo fluorescence spectroscopy of nonmelanoma skin cancer.,” *Photochem. Photobiol.*, vol. 73, no. 2, pp. 178–83, 2001.
- [117] S. Sigurdsson, P. A. Philipsen, L. K. Hansen, J. Larsen, M. Gniadecka, and H.-C. Wulf, “Detection of skin cancer by classification of Raman spectra,” *Biomed. Eng. IEEE Trans.*, vol. 51, no. 10, pp. 1784–1793, 2004.
- [118] S. Nori *et al.*, “Sensitivity and specificity of reflectance-mode confocal microscopy for in vivo diagnosis of basal cell carcinoma: A multicenter study,” *J. Am. Acad. Dermatol.*, vol. 51, no. 6, pp. 923–930, 2004.
- [119] M. Rajadhyaksha, M. Grossman, D. Esterowitz, R. H. Webb, and R. R. Anderson, “In Vivo Confocal Scanning Laser Microscopy of Human Skin: Melanin Provides Strong Contrast.,” *J. Invest. Dermatol.*, vol. 104, no. 6, pp. 946–952, 1995.
- [120] M. Rajadhyaksha, R. R. Anderson, and R. H. Webb, “Video-rate confocal scanning laser microscope for imaging human tissues in vivo.,” *Appl. Opt.*, vol. 38, no. 10, pp. 2105–2115, 1999.
- [121] “VivaScope,” *MAVIG*. [Online]. Available: <http://www.vivascope.de>.
- [122] M. Ares, S. Royo, M. Vilaseca, J. A. Herrera-Ramírez, X. Delpueyo, and F. Sanabria, “Handheld 3D Scanning System for In-Vivo Imaging of Skin Cancer,” *Proc. 5th Int. Conf. 3D Body Scanning Technol. Lugano, Switzerland, 21-22 Oct. 2014*, no. October, pp. 231–236, 2014.
- [123] S. Zhang, “Recent progresses on real-time 3D shape measurement using digital fringe projection techniques,” *Opt. Lasers Eng.*, vol. 48, no. 2, pp. 149–158, 2010.

- [124] L. Chen, C. Quan, C. J. Tay, and Y. Huang, "Fringe contrast-based 3D profilometry using fringe projection," *Optik (Stuttg.)*, vol. 116, no. 3, pp. 123–128, 2005.
- [125] S. Laveau and O. D. Faugeras, "3-D scene representation as a collection of images," *Proc. 12th Int. Conf. Pattern Recognit.*, vol. 1, pp. 689–691, 1994.
- [126] T. Bosch, N. Servagent, and S. Donati, "Optical feedback interferometry for sensing application," *Opt. Eng.*, vol. 40, no. 1, p. 20, 2001.
- [127] R. C. Moreira, A. Quotb, C. Tronche, F. Jayat, T. Bosch, and J. Perchoux, "An embedded 2D imager for microscale flowmetry based on Optical Feedback Interferometry," pp. 5–7, 2016.
- [128] G. T. Holman, "The effects of job environment and culture on patient handling: a nurses perspective," in *Patient Handling: Restrictions & Conditions*, ProQuest, Ed. Auburn University, 2007, p. 119.
- [129] D. C. Dugdale, R. Epstein, and S. Z. Pantilat, "Time and the Patient – Physician Relationship," *J Gen Intern Med*, vol. 14, pp. S34–S40, 1999.
- [130] P. Åberg, I. Nicander, J. Hansson, P. Geladi, U. Holmgren, and S. Ollmar, "Skin Cancer Identification Using Multifrequency Electrical Impedance — A Potential Screening Tool," *IEEE Trans. Biomed. Eng.*, vol. 51, no. 12, pp. 2097–2102, 2004.
- [131] "ColorChecker Classic," *XRite*. [Online]. Available: <http://xritephoto.com/>. [Accessed: 19-Jun-2017].
- [132] E. Senel, "Dermoscopy of non-melanocytic skin tumors," *Indian J Dermatol Venereol Leprol*, vol. 77, no. 1, pp. 16–22, 2011.
- [133] G. Argenziano *et al.*, "Dermoscopy Improves Accuracy of Primary Care Physicians to Triage Lesions Suggestive of Skin Cancer," *J. Clin. Oncol.*, vol. 24, no. 12, pp. 1877–1882, 2006.
- [134] ASTM E2214-08, "ASTM - 2011 - ASTM E2214-08. Standard Practice for Specifying and Verifying the Performance of Color-Measuring Instruments." 2008.
- [135] UNE-EN 62471, "UNE-EN 62471 - Photobiological safety of lamps and lamp systems." 2001.
- [136] D. Liu and J. Yu, "Otsu method and K-means," *Proc. - 2009 9th Int. Conf. Hybrid Intell. Syst. HIS 2009*, vol. 1, no. 2, pp. 344–349, 2009.
- [137] I. L. Weatherall and B. D. Coombs, "Skin color measurements in terms of CIELAB color space values," *J. Invest. Dermatol.*, vol. 99, no. 4, pp. 468–473, 1992.
- [138] G. Pellacani, P. Guitera, C. Longo, M. Avramidis, S. Seidenari, and S. Menzies, "The Impact of In Vivo Reflectance Confocal Microscopy for the Diagnostic Accuracy of Melanoma and Equivocal Melanocytic Lesions," *J. Invest. Dermatol.*,



- vol. 127, no. 12, pp. 2759–2765, 2007.
- [139] B. W. Murphy *et al.*, “Toward the discrimination of early melanoma from common and dysplastic nevus using fiber optic diffuse reflectance spectroscopy.,” *J. Biomed. Opt.*, vol. 10, no. 6, p. 64020, 2012.
- [140] D. Sgouros *et al.*, “Assessment of SIAscopy in the triage of suspicious skin tumours,” *Ski. Res. Technol.*, vol. 20, no. 4, pp. 440–444, 2014.
- [141] FDA PMA P090012, “SUMMARY OF SAFETY AND EFFECTIVENESS DATA (SSED), FDA PMA P090012.” 2011.
- [142] M. Burrioni *et al.*, “Dysplastic naevus vs. in situ melanoma: Digital dermoscopy analysis,” *Br. J. Dermatol.*, vol. 152, no. 4, pp. 679–684, 2005.
- [143] Q. Li, W. Cai, X. Wang, Y. Zhou, D. D. Feng, and M. Chen, “Medical Image Classification with Convolutional Neural Network,” *13th Int. Conf. Control. Autom. Robot. Vis.*, vol. 2014, no. December, pp. 844–848, 2014.
- [144] A. Esteva *et al.*, “Dermatologist-level classification of skin cancer with deep neural networks,” *Nature*, vol. 542, no. 7639, pp. 115–118, 2017.
- [145] R. G. B. Langley *et al.*, “The diagnostic accuracy of in vivo confocal scanning laser microscopy compared to dermoscopy of benign and malignant melanocytic lesions: a prospective study.,” *Dermatology*, vol. 215, pp. 365–372, 2007.

# Appendix A. Datasheets of components used in the developed system

## A.1 Big metal ring

ITEM PART #	DESCRIPTION	REVISIONS			
REV	DESCRIPTION	DATE	BY	APPROVED	
A1	PROTOTYPE		JERREKA	CO	
A2	ADDED DIMENT		DONOVAN	CO	
A3	ADDED 3RD VIEW		MAJANCA	CO	

RING MATERIAL : BLACK POLYCARBONATE  
ADHESIVE RING : 3M MEDICAL TAPE #1522  
DR. SIMILAR

**MAVIG**  
Steinstraße 5 · Munich, Germany

**DIAGNOSTICS INTERFACE RING**

SIZE	BEARING #	PART CODE	REV	SCALE
D	N/A	NW	A3	3
				SHEET 1 OF 1

**THIS IS A COMPUTER GENERATED DRAWING OF THE DESIGN MASTER. IT IS NOT TO BE USED FOR THE FABRICATION OF PARTS. ANY CHANGES TO THE DRAWING MUST BE MADE TO THE ORIGINAL DRAWING FILE. THIS DRAWING IS NOT TO BE USED FOR THE FABRICATION OF PARTS.**

**INTENTIONAL COPY**    **PLEASE OBSERVE SPECIFIC DIMENSIONS AND TOLERANCES**    **MANUFACTURE DATE: 2/22/24**

DATE: 2/22/24    DATE: 2/22/24

DATE: 2/22/24    DATE: 2/22/24

DATE: 2/22/24    DATE: 2/22/24

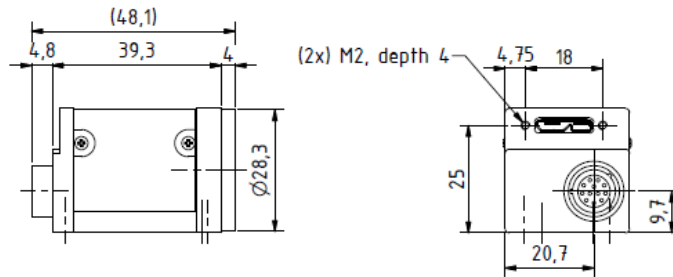
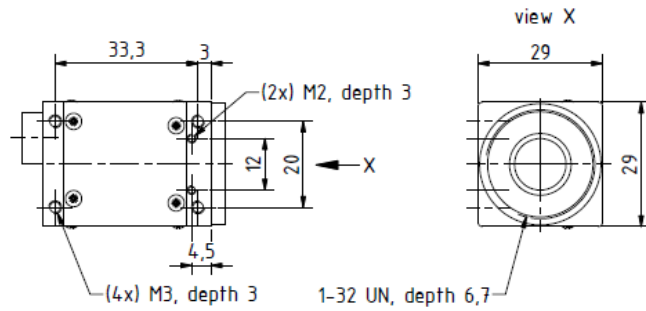
## A.2 DMK 23U455 camera

A. DATASHEETS OF COMPONENTS USED IN THE DEVELOPED SYSTEM



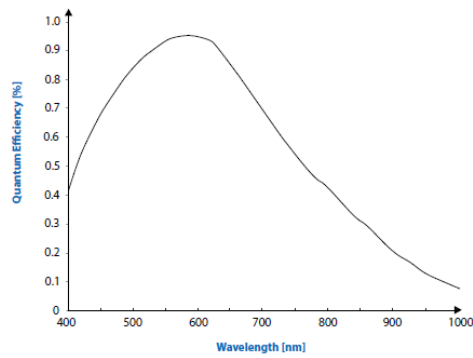
**DxK 23U618**  
**DxK 23U445**  
**DxK 23U274**

(without tripod adapter)



(without tripod adapter)

Dimensions: mm  
 Tolerances: DIN ISO 2768m



### A.3 Sony ICX445ALA sensor

# SONY

Diagonal 6.0mm (Type 1/3) Progressive Scan CCD Image Sensor for B/W Cameras

# ICX445ALA

---

#### Description

The ICX445ALA is a diagonal 6.0mm (Type 1/3) interline CCD solid-state image sensor with a square pixel array and 1.25M effective pixels.  
Progressive scan enables all pixel signals to be output separately and sequentially within 1/22.5 second.  
The sensitivity and smear are improved drastically through the adoption of EXview HAD CCD technology.

---

#### Features

- ◆ Supports following readout modes
  - All-pixel scan mode (15 frame/s, 12.5 frame/s, 22.5 frame/s: Max.)
  - Center cut-out mode (30 frame/s, 25 frame/s)
- ◆ Horizontal drive frequency: 36.0MHz, 29.0MHz
- ◆ High resolution, high sensitivity, low dark current, low smear
- ◆ Excellent anti-blooming characteristics
- ◆ No voltage adjustments (Reset gate and substrate bias need no adjustment.)
- ◆ 24-pin high precision plastic package (Dual-surface reference available)

---

#### Package

24-pin DIP (Plastic)

## **EXview HAD CCD**™

\* EXview HAD CCD is a trademark of Sony Corporation. The EXview HAD CCD is a CCD that drastically improves light efficiency by including near infrared light region as a basic structure of HAD (Hole-Accumulation Diode) sensor.

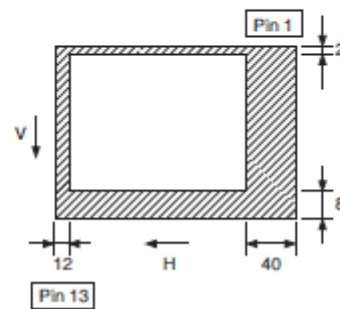
Sony reserves the right to change products and specifications without prior notice. This information does not convey any license by any implication or otherwise under any patents or other right. Application circuits shown, if any, are typical examples illustrating the operation of the devices. Sony cannot assume responsibility for any problems arising out of the use of these circuits.

### Device Structure

- ◆ Interline CCD image sensor
- ◆ Image size  
Diagonal 6.0mm (Type 1/3)
- ◆ Total number of pixels  
1348 (H) × 976 (V) approx. 1.32M pixels
- ◆ Number of effective pixels  
1296 (H) × 966 (V) approx. 1.25M pixels
- ◆ Number of active pixels  
1280 (H) × 960 (V) approx. 1.23M pixels
- ◆ Chip size  
6.26mm (H) × 5.01mm (V)
- ◆ Unit cell size  
3.75 $\mu$ m (H) × 3.75 $\mu$ m (V)
- ◆ Optical black  
Horizontal (H) direction: front 12 pixels, rear 40 pixels  
Vertical (V) direction: front 8 pixels, rear 2 pixels
- ◆ Number of dummy bits  
Horizontal (H) direction: front 4 pixels  
Vertical (V) direction: front 2 pixels
- ◆ Substrate material  
Silicon

### Optical Black Position

(Top View)



## A.4 Schenider-Kreuznack Cinegon 1.8/16



### Mega Pixel lens for image circle 16 mm

---

#### Cinegon 1.8/16

In accordance with the sensitivity of modern 1" CCD and CMOS sensors, the megapixel lenses are corrected and broadband-coated for the spectral range of 400 – 1000 nm ( VIS + NIR ). Even under production and / or extreme conditions, the robust mechanical design with lockable focus and iris setting mechanism guarantees reliable continuous use in which the set optical parameters remain in place.



Cinegon 1.8/16

#### Key Features

- High-resolution optics
- Highest optical imaging performance even with smallest pixel sizes
- Broadband coating (400 - 1000 nm)
- Compact and low weight
- Vibration insensitivity for stable imaging performance
- Focus and iris setting lockable

#### Applications

- Machine Vision and other imaging applications
- 3D measurement
- Traffic
- Medical
- Robot vision
- Food processing

#### Technical Specifications

F-number	1.8
Focal length	16.4 mm
Image circle	16 mm
Transmission	400 - 1000 nm
Interface	C-Mount
Weight	102 gr.
Filter Thread	M30.5 x 0.5
Order No.	1001482

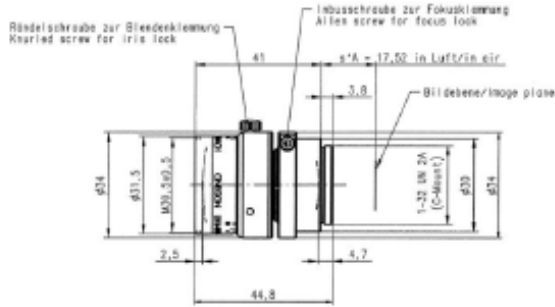
#### Contact

Jos. Schneider Optische Werke GmbH  
 Ringstraße 132  
 55543 Bad Kreuznach  
 Germany  
 Phone +49 671 601-205  
 Fax +49 671 601-286  
[www.schneiderkreuznach.com](http://www.schneiderkreuznach.com)  
[industrie@schneiderkreuznach.com](mailto:industrie@schneiderkreuznach.com)

Schneider Asia Pacific Ltd.  
 20/F Central Tower, 28 Queen's Road  
 Central, Hong Kong  
 China  
 Phone +852 8302 0301  
 Fax +852 8302 4722  
[www.schneider-asiapacific.com](http://www.schneider-asiapacific.com)  
[info@schneider-asiapacific.com](mailto:info@schneider-asiapacific.com)

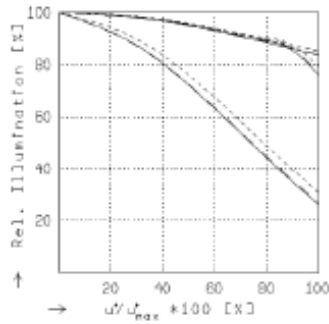
Schneider Optics Inc.  
 285 Oser Ave.  
 Hauppauge, NY 11788  
 USA  
 Phone +1 631 781-5000  
 Fax +1 631 781-5090  
[www.schneideroptics.com/industrial](http://www.schneideroptics.com/industrial)  
[industrial@schneideroptics.com](mailto:industrial@schneideroptics.com)

## Cinegon 1.8/16



### CINEGON 1.8/16

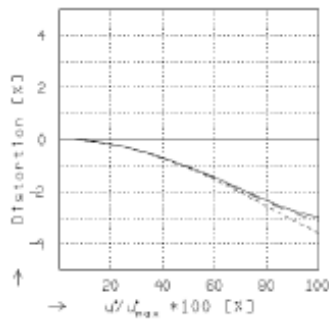
$f^* = 16.4 \text{ mm}$	$\delta_p = 2.591$
$s_f = 11.1 \text{ mm}$	$s_{EP} = 17.4 \text{ mm}$
$s_f^* = 18.5 \text{ mm}$	$s_{EP}^* = -29.1 \text{ mm}$
$HH^* = 12.0 \text{ mm}$	$\Sigma d = 37.5 \text{ mm}$



### RELATIVE ILLUMINATION

The relative illumination is shown for the given focal distances or magnifications.

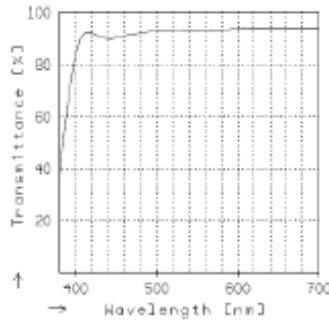
$f / 1.8$	$f / 4.0$	$f / 8.0$
— $\theta^* = 0.0000$	$u_{POK}^* = 8.0$	$CO^* = \infty$
- - $\theta^* = -0.0200$	$u_{POK}^* = 8.0$	$CO^* = 867.$
--- $\theta^* = -0.1000$	$u_{POK}^* = 8.0$	$CO^* = 211.$



### DISTORTION

Distortion is shown for the given focal distances or magnifications. Positive values indicate pincushion distortion and negative values barrel distortion.

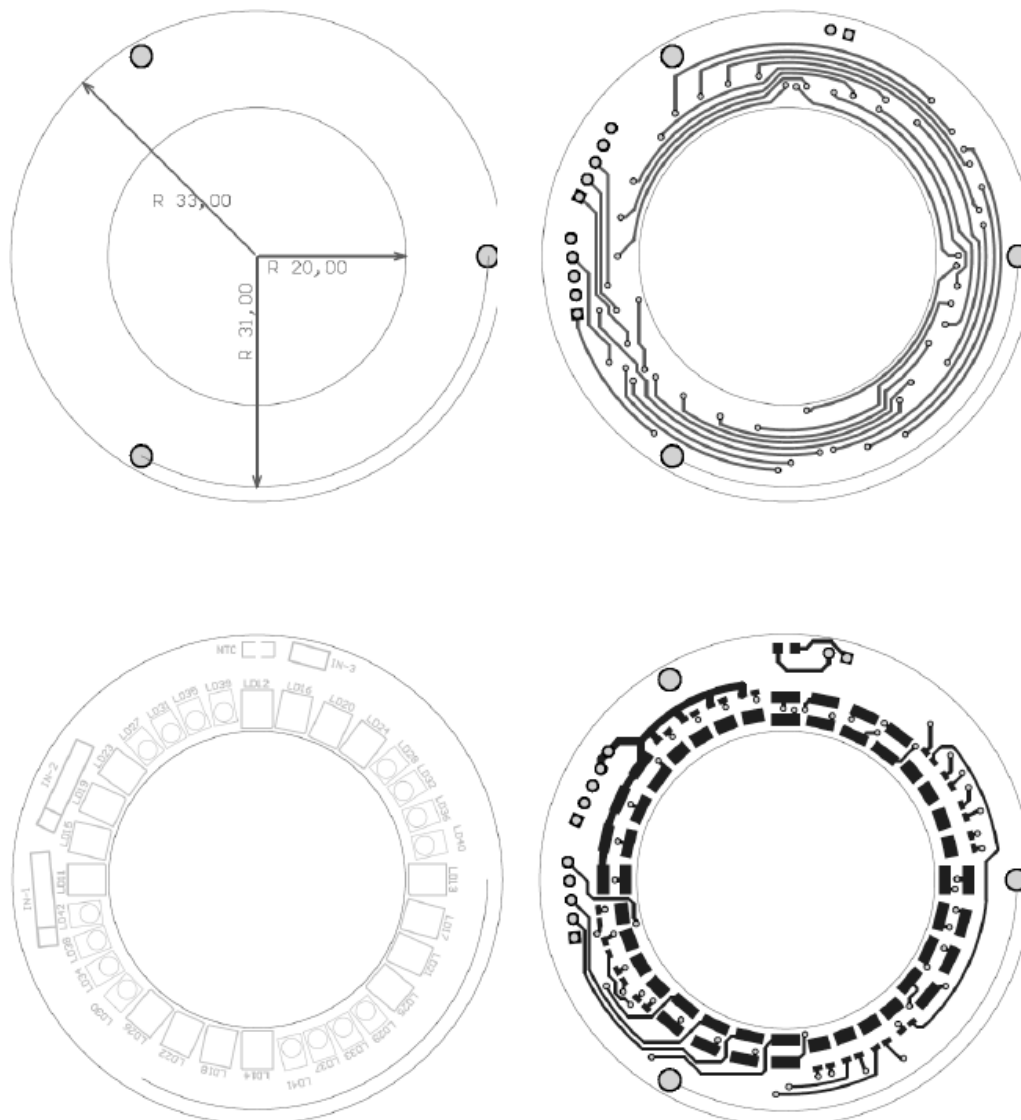
— $\theta^* = 0.0000$	$u_{POK}^* = 8.0$	$CO^* = \infty$
- - $\theta^* = -0.0200$	$u_{POK}^* = 8.0$	$CO^* = 867.$
--- $\theta^* = -0.1000$	$u_{POK}^* = 8.0$	$CO^* = 211.$



### TRANSMITTANCE

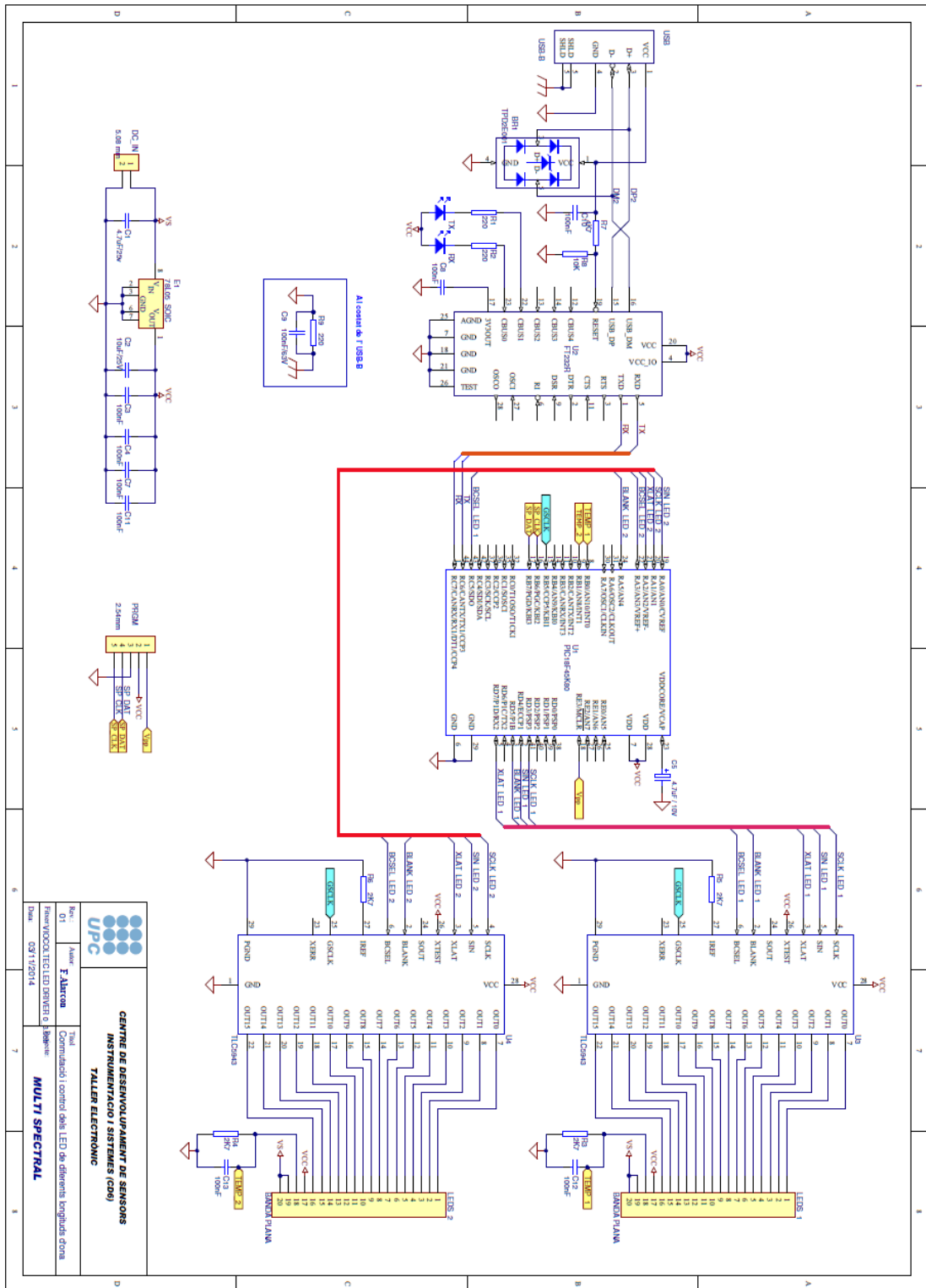
Relative spectral transmittance is shown with reference to wavelength.

### A.5 LEDs board



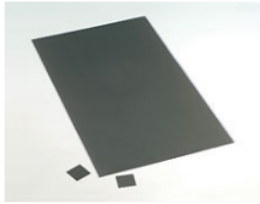


A.6 Electronic board to control the LEDs



## A.7 Visible linear polarizing laminated film from Edmund Optics

### Visible Linear Polarizing Laminated Film



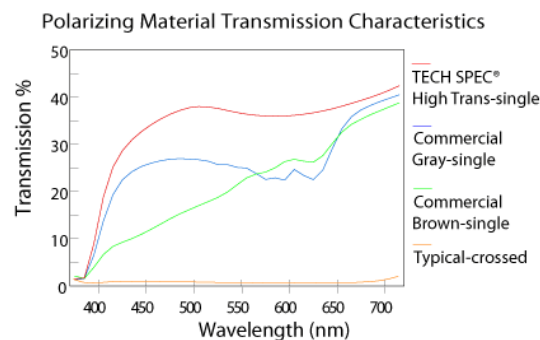
- 38% Transmission of Unpolarized Light
- Laminated for Increased Durability
- Good Color Reproducibility

Visible Linear Polarizing Laminated Film is ideal for a range of [microscopy](#), display, and [imaging](#) applications. A single sheet features 38% transmission of unpolarized light. When two sheets are crossed, transmission reduces to 0.04%. If used at 550nm, the crossed transmission is less than 0.01%. Two sheets can also be used as a variable attenuator.

**Note:** For sheets, the transmission axis is parallel to the first dimension listed.

Visible Linear Polarizing Laminated Film is manufactured using a precision method of aligning long chain polymers in order to produce a highly product, with extremely good color reproducibility. To increase durability and stiffness, the film is laminated in cellulose triacetate (CTA). The sheets are neutral gray in color.

Dimensions (inches)	17 x 30
Thickness (inches)	0.03
Thickness (mm)	0.762
Number of Sheets	1
Color	Gray
Transmission (%)	Single:38 Parallel: 27 Crossed: 0.04
Polarization	>99% Efficiency
Durability	Meets FDA Impact Test, ANSI Z80.3 Standards, Proposed ISO Standards, and Can Be Thermoformed with Standard Equipment
Operating Temperature (°C)	74
UV Absorption (%)	>99
Construction	Polarizing Film
Substrate	Film
Type	Linear Polarizer
RoHS	<a href="#">Compliant</a>



A.8 X Rite ColorChecker® Classic CCCR



The data below is intended to be an average measurement of all ColorChecker Charts. ColorChecker Charts should be replaced every two years as fading of the colors will alter the values of the chart.

No.	Number	sRGB			CIE L*a*b*			Munsell Notation	
		R	G	B	L*	a*	b*	Hue Value / Chroma	
1.	dark skin	115	82	68	37.986	13.555	14.059	3 YR	3.7 / 3.2
2.	light skin	194	150	130	65.711	18.13	17.81	2.2 YR	6.47 / 4.1
3.	blue sky	98	122	157	49.927	-4.88	-21.925	4.3 PB	4.95 / 5.5
4.	foliage	87	108	67	43.139	-13.095	21.905	6.7 GY	4.2 / 4.1
5.	blue flower	133	128	177	55.112	8.844	-25.399	9.7 PB	5.47 / 6.7
6.	bluish green	103	189	170	70.719	-33.397	-0.199	2.5 BG	7 / 6
7.	orange	214	126	44	62.661	36.067	57.096	5 YR	6 / 11
8.	purplish blue	80	91	166	40.02	10.41	-45.964	7.5 PB	4 / 10.7
9.	moderate red	193	90	99	51.124	48.239	16.248	2.5 R	5 / 10
10.	purple	94	60	108	30.325	22.976	-21.587	5 P	3 / 7
11.	yellow green	157	188	64	72.532	-23.709	57.255	5 GY	7.1 / 9.1
12.	orange yellow	224	163	46	71.941	19.363	67.857	10 YR	7 / 10.5
13.	blue	56	61	150	28.778	14.179	-50.297	7.5 PB	2.9 / 12.7
14.	green	70	148	73	55.261	-38.342	31.37	0.25 G	5.4 / 8.65
15.	red	175	54	60	42.101	53.378	28.19	5 R	4 / 12
16.	yellow	231	199	31	81.733	4.039	79.819	5 Y	8 / 11.1
17.	magenta	187	86	149	51.935	49.986	-14.574	2.5 RP	5 / 12
18.	cyan	8	133	161	51.038	-28.631	-28.638	5 B	5 / 8
19.	white (.05*)	243	243	242	96.539	-0.425	1.186	N	9.5 /
20.	neutral 8 (.23*)	200	200	200	81.257	-0.638	-0.335	N	8 /
21.	neutral 6.5 (.44*)	160	160	160	66.766	-0.734	-0.504	N	6.5 /
22.	neutral 5 (.70*)	122	122	121	50.867	-0.153	-0.27	N	5 /
23.	neutral 3.5 (1.05*)	85	85	85	35.656	-0.421	-1.231	N	3.5 /
24.	black (1.50*)	52	52	52	20.461	-0.079	-0.973	N	2 /

Cie L\*a\*b\* values use Illuminant D50 2 degree observer sRGB values for Illuminate D65.

# Appendix B. Instrumentation used in the thesis

## B.1 Spectrometer Instrument Systems Spectro 320



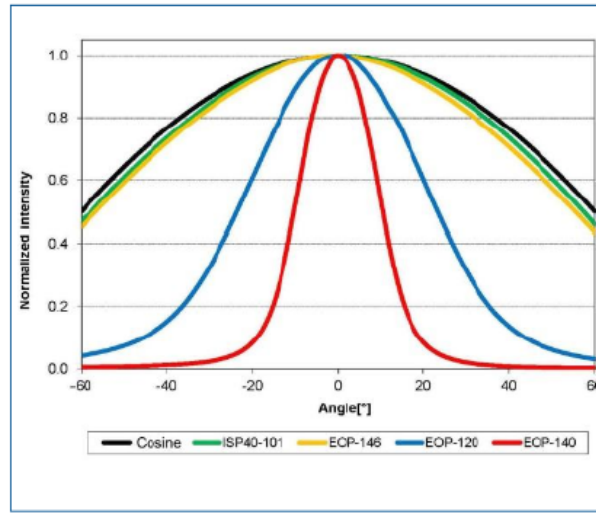
### Key features at a glance

- Fast-Scan Technology offers short measurement times with very high accuracy and large signal dynamic range
- Broad spectral range, up to 190 – 5000 nm
- Single and double monochromator versions
- Integrated density filter wheel facilitates an extremely wide intensity measurement range
- Programmable spectral resolution from 0.1 to 20 nm

## Technical specifications

Model **	UV		VIS		IR1	IR2	IR3	
Spectral range [nm]	100–1050	190–930	350–1100	350–930	800–1700	850–2150	800–3200	1000–5000
Detector **	Si	PMT	Si	PMT	InGaAs	ext. InGaAs	PbS	PbSe
Grating lines ** [l/mm] / Blaze [nm]	1200 / 300		1200 / 500		600 / 1000	300 / 1300	300 / 1300	325 / 2000
Scan time [ms/nm]	12–500		12–500		12–500	20–500	20–500	20–500
Spectral resolution ** [nm]	0.3–5 / 0.1–5		0.3–5 / 0.1–5		0.6–10 / 0.15–10	1.2–20 / 0.3–20	1.2–20 / 0.3–20	1.2–20 / 0.3–20
Wavelength accuracy ** [nm]	±0.1 / ±0.03		±0.1 / ±0.03		±0.2 / ±0.05	±0.5 / ±0.1	±0.5 / ±0.1	±0.5 / ±0.1
Wavelength reproducibility ** [nm]	±0.05 / ±0.01		±0.05 / ±0.01		±0.1 / ±0.02	±0.2 / ±0.05	±0.2 / ±0.05	±0.2 / ±0.05
Minimum increments for data points ** [nm]	0.05 / 0.01		0.05 / 0.01		0.1 / 0.02	0.2 / 0.05	0.2 / 0.05	0.2 / 0.05
Stray light (broadband) ** %	1·10 <sup>-4</sup> / 1·10 <sup>-5</sup>		1·10 <sup>-4</sup> / 1·10 <sup>-5</sup>		<2·10 <sup>-4</sup> / <5·10 <sup>-5</sup>	<2·10 <sup>-4</sup> / -	<2·10 <sup>-4</sup> / -	<2·10 <sup>-4</sup> / -
Stray light (laser) ** %	1·10 <sup>-2</sup> / 1·10 <sup>-3</sup>		1·10 <sup>-2</sup> / 1·10 <sup>-3</sup>		1·10 <sup>-2</sup> / 1·10 <sup>-3</sup>	1·10 <sup>-2</sup> / -	1·10 <sup>-2</sup> / -	1·10 <sup>-2</sup> / -
<b>Spectroradiometry</b>								
Noise equivalent irradiance ** [W/m <sup>2</sup> nm]	8·10 <sup>-7</sup> / 3·10 <sup>-4</sup>	9·10 <sup>-10</sup> / 3·10 <sup>-3</sup>	1·10 <sup>-7</sup> / 5·10 <sup>-7</sup>	2·10 <sup>-10</sup> / 6·10 <sup>-10</sup>	2·10 <sup>-4</sup> / 6·10 <sup>-5</sup>	5·10 <sup>-4</sup> / 2·10 <sup>-7</sup>	2·10 <sup>-4</sup> / 8·10 <sup>-4</sup>	3·10 <sup>-4</sup> / -
Measuring uncertainty irradiance ** %	±3.5 %	±3.5 %	±3.5 %	±3.5 %	±3.5 %	±4 %	±4 %	±6 %
<b>Spectrophotometry</b>								
Transmission measuring accuracy ** %	±0.1 % T		±0.1 % T		±0.15 % T	±0.25 % T	±0.25 % T	±0.5 % T
Baseline noise ** %	±0.05 %		±0.05 %		±0.05 %	±0.1 %	±0.1 %	±0.3 %
Baseline drift ** /h	0.2 % /h		0.2 % /h		0.2 % /h	0.5 % /h	0.5 % /h	1 % /h
<b>Monochromator</b>								
Monochromator and grating type	Asymmetrical Czerny-Turner configuration, subtractive double monochromator; plane grating (standard ruled, optional holographic)							
Focal length, aperture number	320 mm; f/4.6							
Slit widths of the slit wheels [mm]	2 / 1 / 0.4 / 0.2 / 0.1 (additionally for SP320-200: 0.05 / 0.02 / 0.01)							
Configuration of the filter wheels **	Density filter: OD1, OD2 and OD3; order-sorting filter: different filters for suppression of higher diffraction orders							
<b>Electrical data</b>								
Power consumption	Basic version: 65 W, when the system is fully extended: max. 130 W							
Power supply	Broadband input 100 VAC – 230 VAC 50/60 Hz						115 or 230 VAC 50/60 Hz	
PC-interface	RS-232 standard; IEEE-488 Bus optional							
<b>Miscellaneous</b>								
Dimensions (H, W, D) **	220 x 425 x 560 mm <sup>3</sup> / 200 x 425 x 560 mm <sup>3</sup>							
Weight **	approx. 23 kg / approx. 35 kg							
Ambient conditions	15 – 35 °C; max. relative humidity 70 %, non-condensing							
Sound level	max. 70 dBA							
Applicable standards	EN 61326-1:2006, EN 61326-2-2:2006, EN 61010-1:2002-08							

B.1.1 Optical probe EOP 146



Cosine behavior of different EOPs

Model	Acceptance angle	Cosine correction	Throughput	Spectral range	Application
EOP-120	± 6°	Average	Good	190 – 1700 nm	Universal
EOP-140	± 3°	Low	High	190 – 2500 nm	Low light levels
EOP-146	± 32°	Good	Average	190 – 2500 nm	Extended light sources
EOP-350	± 4°	Low	Good	1000 – 5000 nm	Infrared range
EOP-542	-	-	High	190 – 2500 nm	Direct solar radiation, 5.7° aperture angle
ISP 40	± 55°	Very good	Low	220 – 2500 nm	Solar radiation

Selection of available optical probes with qualitative assessment of cosine correction and light throughput. The specified acceptance angle (measured using the photometric integral and the radiometric integral between 1000 nm and 1500 nm for EOP-350, respectively) applies for deviations from the cosine behavior of < 5 %.

## B. INSTRUMENTATION USED IN THE THESIS

---

### B.1.2 Telescopic optical probe TOP 100



The compact integrating spheres of the ISP 80 and ISP 150 series were specially developed for diffuse reflection and transmission measurements. The two spheres are coated with BaSO<sub>4</sub> and can be used for the spectral range from 300 to 2200 nm. The measuring setup is easy to reconfigure between reflection and transmission measurements.

B.1.3 Telescopic optical probe TOP 100



Spectral measurement application range: 370...1600 nm  
 Largest measurement spot: 22 mm at 500 mm  
 Smallest measurement spot: 2 mm at 500 mm  
 Measurement repeatability: better than  $\pm 1\%$  at maximum scan amplitude.

**Operating Conditions**

Ambient temperature:	+10°C to +30°C
Relative air humidity:	< 70 % for acclimatized instrument

**Storage Conditions**


Ambient temperature:	-10°C to +40°C
Relative air humidity:	< 70 % for acclimatized instrument
Packaging:	In plastic foil with desiccant

## B.2 International Light Radiometer (IL 1700)

data sheet IL 1700

IL 1700 RESEARCH RADIOMETER

State of the Art in Light Measurement



The image shows the IL 1700 Research Radiometer, a white rectangular device with a black carrying handle. The front panel features a digital display showing '11.669 x10', several control buttons, and a 'FUNCTION' selector. The text 'IL1700' and 'RESEARCH RADIOMETER' is printed on the device.

INCLUDING SYSTEMS


- IL1705 Research Radiometer
- IL1710 Research Photometer
- IL1730 UV Actinic Radiometer
- IL1740 Photoresist Radiometer
- IL1745 UV Curing Radiometer
- IL1770 Germicidal/Erythematol Radiometer

FEATURES

The all new IL1700 Research Radiometer is the most powerful available today. When combined with ILL's standard detectors, filters and input optics, this new system provides a choice of over 200 different spectral and spatial measurement capabilities, most available from stock. **The microprocessor controlled** circuitry has enhanced capabilities in many new areas. The **continuous memory** stores ten (10) sensitivity factors for different detector, filter, diffuser combinations. **Ranging is automatic** or fixed and provides direct reading on a 3½ digit (plus exponent) display, in any optical units appropriate for the sensor combination. In addition, **"Auto 100%"** offers direct transmission measurements using any stable light source as the reference. The **"auto zero"** function will zero the digital display within 2 seconds in the fixed range or auto range mode.

A unique feature is Auto Ranging in the Integrate Mode. You do not have to experiment to determine the correct range for flash measurements. Just touch "Auto Zero" to subtract ambient conditions, and then touch integrate to capture the flash. "Hold" keeps a solid reading even after the room lights are turned on. Another unusual capability is the long term integration accuracy. Accumulations over periods of weeks or months are possible without any degradation of accuracy. External signals can be used to either trigger the flash or completely control the instrument from a remote source such as a computer. The data can also be sent out through an industry standard interface (**RS232C**) for data processing in automated systems. A user convenience switch configures the instrument to match up with either DTE or DCE equipment, to get you on line fast.

Continued on pg. 5



international light

INC.

DEXTER INDUSTRIAL GREEN, NEWBURYPORT, MA 01950 U.S.A.  
■ TEL. 617-465-5923 ■ TELEX 94-7135



## IL 1700 SERIES SYSTEMS

### IL 1705 Research Radiometer System

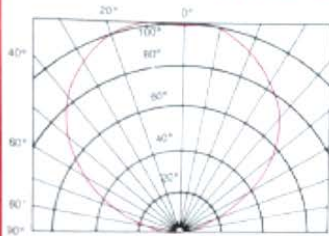


Fig. 1 Relative Sensitivity vs Angle

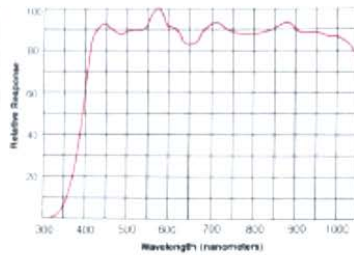


Fig. 2 Relative Spectral Sensitivity

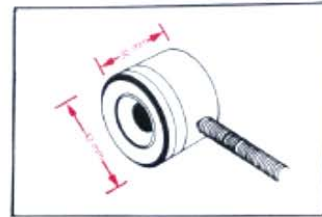


Fig. 3 Detector dimensions

**Detector Model No.:** SED038/F/W

**Units of Calibration:** Watts per square centimeter

**Dynamic Range:**  $1 \times 10^{-9}$  to  $1 \times 10^{-1}$  W/cm<sup>2</sup>

**Spectral Range:** 410nm to 1060 nm (see fig. 2)

The IL1705 Research Radiometer System is designed for making irradiance measurements through the visible and near IR. The input optics can be changed to make laser power measurements (direct reading in watts with Model HNK15 Narrow Beam Adapter), or to make radiance measurements (direct reading in watts per square centimeter per steradian with Model R Radiance Barrel). Removing the filter, Model F, will produce a spectral range of 350nm to 1100nm. Other stock filters can provide narrower spectral ranges. (eg Model NS546 filter has a 10nm bandpass).

### IL 1710 Research Photometer System

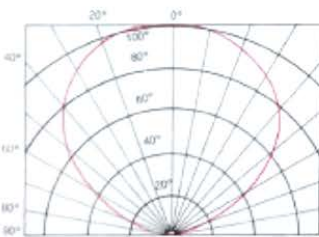


Fig. 4 Relative Sensitivity vs Angle

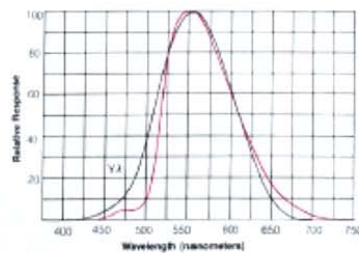


Fig. 5 Relative Spectral Sensitivity

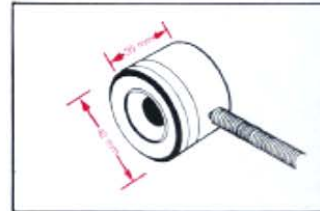


Fig. 6 Detector Dimensions

**Detector Model No.:** SED038/Y/W

**Units of Calibration:** Lumens per square foot (foot-candles)

**Dynamic Range:**  $1 \times 10^{-3}$  foot candles to  $5 \times 10^4$  foot-candles

**Spectral Range:** Visible (see fig. 5)

The IL1710 Research Photometer System has been designed to make illuminance measurements with a high degree of fidelity to the CIE visual spectral response function. The system is calibrated in foot candles but it can be programmed by the user to read in lux, candela and effective candela for a flashing source. An optional filter (Model ZCIE) will provide scotopic spectral response for low light level visual applications. A high gain lens (Model L30) is available for beam candle power measurement at long distance.

---

# Appendix C. User manual of the multispectral system

---

## 1. Getting started

Steps to follow:

- a) Once positioned the medical cart to examine the patients at the hospital, switch the medical cart by pushing the central button of power supply.
- b) Turn on the computer in the medical cart, and wait until the monitor the Windows 7 desktop appears.
- c) Before starting the control program of the multispectral dermoscope (DM) ensure that it is properly located on the base.
- d) Initialize the MS PR1 program by clicking its icon.

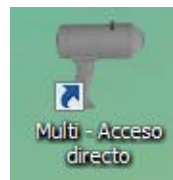


Figure 1

The program will display an image when starting to check operation of its lighting system – LED ring light source (Figure 2). If there is an error message, follow the instruction presented in section "4.5. Troubleshooting".

MS PR1 - LEDS TEST			
416 nm	OK	660 nm	OK
450 nm	?	728 nm	?
476 nm	?	880 nm	?
524 nm	?	985 nm	?

Figure 2

e) If it is the first time that the program is used during this day, the system performs an assisted calibration procedure. Follow the prompts to this process as shown in section "4.3. Calibration". Otherwise go to the next step.

f) After calibration, the patient selection screen is shown, with his/her identification (ID PATIENT, which is a numerical code), the lesion to be measured (LESION), and the test date (DATE) of the last analyzed patient (Figure 3). In case you want to make a new measurement, press the "NEW" button to enter the data. Once this is done, press the "OK" button. In case you want to access the home screen, press the "CANCEL" button.

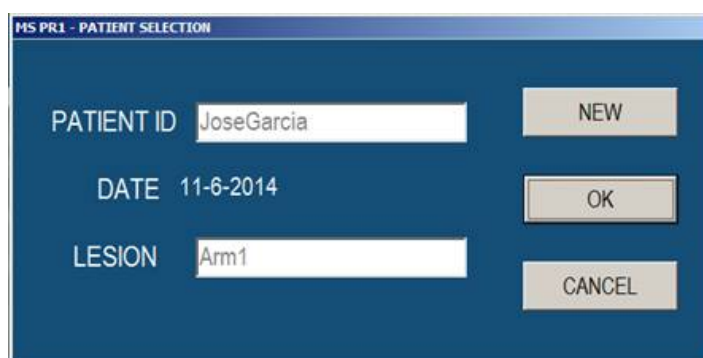


Figure 3

g) If the name of the patient and the lesion already exist, a new window will appear with the warning message "LESION IS ALREADY SAVED, DO YOU WANT TO OVERWRITE THE DATA?" (Figure 4). In case you agree to overwrite the information press the "Aceptar" button; in case you want to keep the information press the "Cancelar" button to return to the patient selection window. In case this window is not shown to go to the next step.

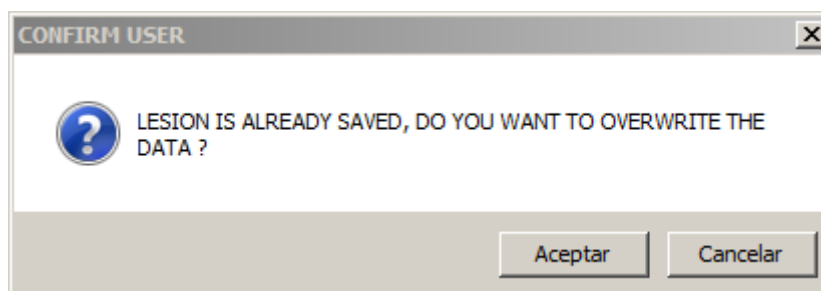


Figure 4

h) A new window to confirm patient data will appear on the screen (Figure 5). Press the "Aceptar" button if the information is correct before continuing with the measure of the lesion. If not, press the "Cancel" button and return to the initial screen. The steps to be followed for the measurement of the lesion are shown in Section 2 "Multispectral dermoscope measurement".



Figure 5

In any case the software will enable measuring without a patient name and the name of the lesion.

## 2. Multispectral dermoscope measurement

The main window of the program interface control of the MD appears after switching on the equipment as shown in Figure 6. This interface contains different areas, buttons and displays live images that are being captured with the MD.

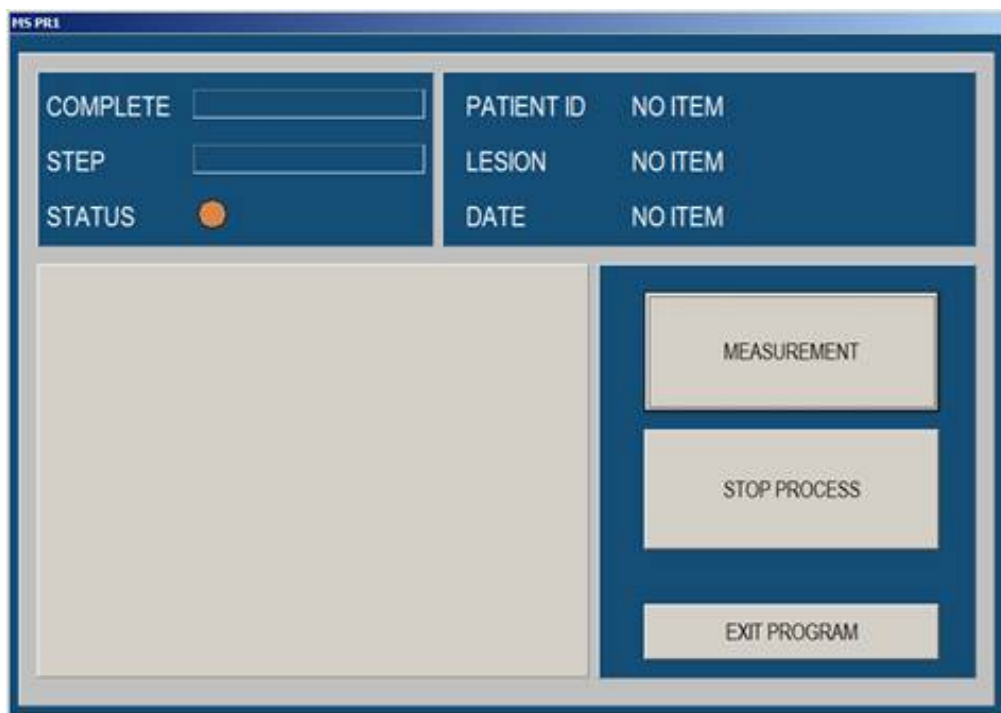


Figure 6

To perform a measurement is necessary to follow the following steps:

- a) First, place an adhesive film onto the metal ring, which has an outer diameter of 41.9 mm and an internal diameter of 31.75 mm. Then, put the metal ring in contact with the skin and centered with respect to the lesion to be measured

b) Place the MD on the lesion with the help of the ring and put the screw in position 1, as indicated by the pop-up screen (Figure 7). Click on "Aceptar".

c) Place the screw in position 2 when prompted by the pop-up screen and press the "Aceptar" (Figure 8) button. Do the same with the position 3 (Figure 9).



Figure 7

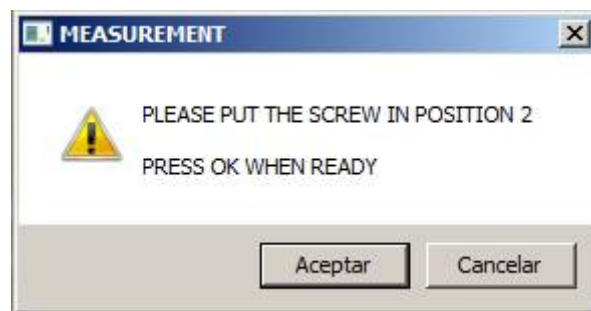


Figure 8

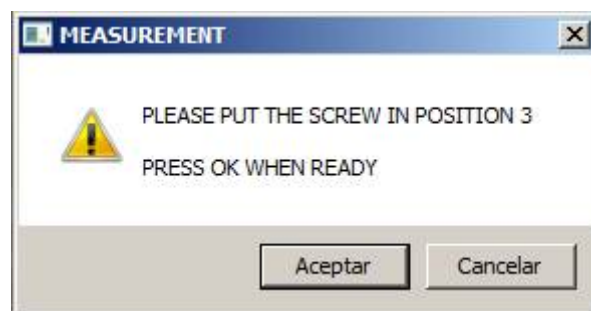


Figure 9

- Initially, the device performs an auto-exposure according to the characteristics of skin pigmentation patient and subsequently, it captures the images. These images are captured for different polarization states, making it necessary to replace the polarizing screw in the positions indicated on-screen messages.

- At the end of the process the images will be saved automatically.

- At any time, the process can be canceled by pressing the "STOP PROCESS" button or the "Cancel" button in the pop-up screens.

d) If you need a new measurement, press the "MEASUREMENT" button to move to patient selection.

### 3. Calibration

The MD will perform a daily assisted calibration to ensure proper image acquisition. This process takes about 5 minutes and follows the same scheme of the measurement procedure explained in the previous section. The calibration process appears as a mandatory step each day, only the first time that the MD is used. You cannot do any action without prior calibration. The steps are:

a) If the device has not been calibrated, a pop-up screen with the message "DEVICE MUST BE CALIBRATED" (Figure 10) appears. Place the MD on the base and press the "Aceptar" button.



Figure 10

b) Put the calibration sample in position "IN" and press the "Aceptar" button in the pop-up screen (Figure 11).



Figure 11

c) Put the screw in position 1 and press the "Aceptar" button in the pop-up screen (Figure 12).

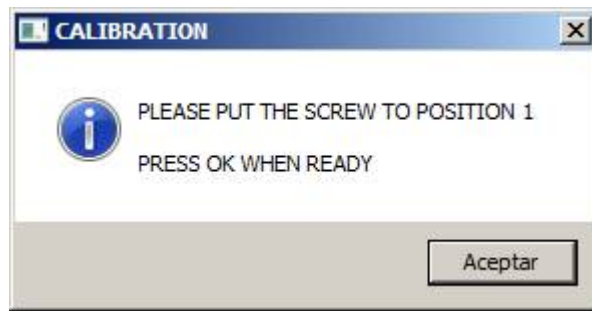


Figure 12

d) Place the screw in position 2 when prompted by the pop-up screen and press the "Aceptar" button (Figure 13). Do the same with the position 3 (Figure 14).

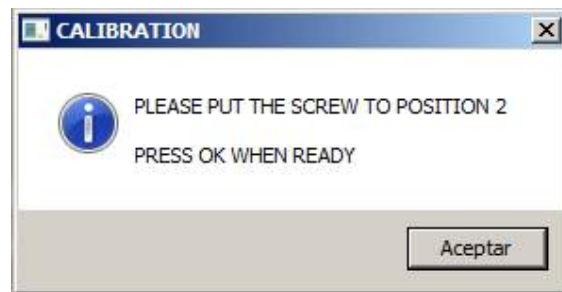


Figure 13

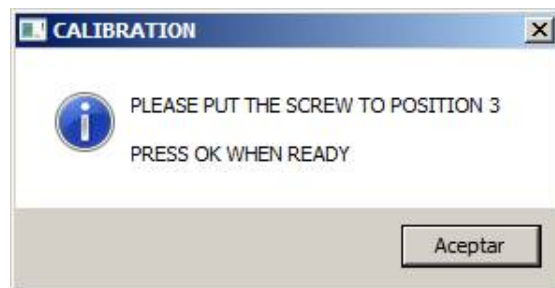


Figure 14

f) Put the calibration sample in the "OUT" position and click "Aceptar" the pop-up screen (Figure 15).

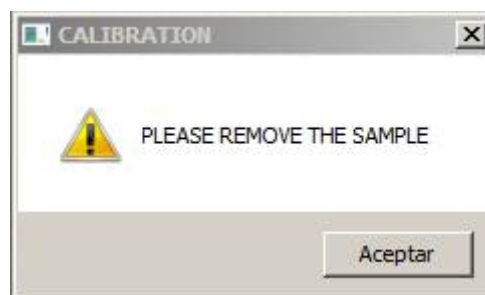


Figure 15

- At the end of the process the images will be saved automatically.

- At any time, the process can be canceled by pressing the "STOP PROCESS" button, but any action will be carried out until calibration has been completely done.

### 4. Switching the device off

a) After measurements are performed, close the program by clicking the Close button on the screen and press the "Aceptar" button (Figure 16).

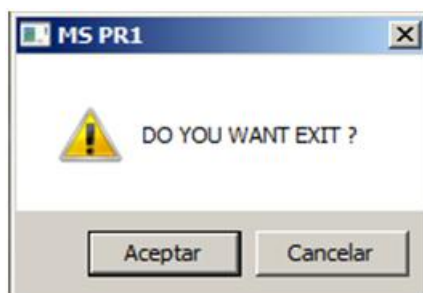


Figure 16

b) In case you are not going to use the computer, also switch it off.

c) In case you are not going to use the medical cart, also switch it off (Figure 17).



Figure 17

### 5. Troubleshooting

Although it is not usual, sometimes specific problems may occur while using the program. Those most likely to occur are described here:

a) In case there is a failure in the communication with the camera or LED ring light source a pop-up window is shown (Figures 18 and 19, respectively). Disconnect the USB cable from the camera and the LED ring light source of the computer, wait 10 seconds and reconnect. If the error persists, contact the Technical Support (contact details in section 6).



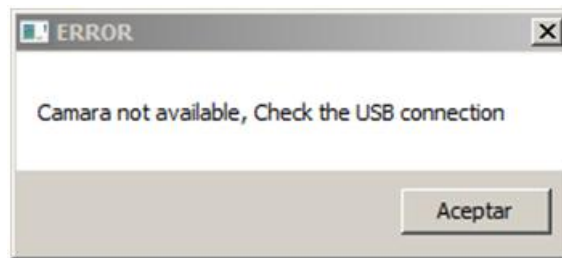


Figure 18



Figure 19

b) In case there is a failure when checking the LEDs operation, the pop-up message of Figure 20 is displayed. In this case, contact the Technical Support (Contact in section 6).

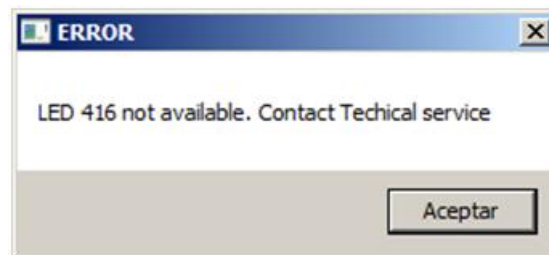


Figure 20

- Other troubles (problems in the measures, failure of any component, etc.), contact the Technical Support (Contact in section 6).

## 6. Contact

Dr. Santiago Royo Royo

[santiago.royo@upc.edu](mailto:santiago.royo@upc.edu)

Tel. +34 937 398 904

Dra. Meritxell Vilaseca

[meritxell.vilaseca@upc.edu](mailto:meritxell.vilaseca@upc.edu)

Tel. +34 937 398 767

CD6 - Centre de Desenvolupament de Sensors, Instrumentació i Sistemes

Rambla Sant Nebridi, 10

08222 · Terrassa

Spain

### Getting here

